Computational modelling of embryogenesis driven by empirical evidence from 4D microscopy images

Joel Dokmegang

PhD 2020

Manchester Metropolitan
University

Computational modelling of embryogenesis driven by empirical evidence from 4D microscopy images

Joel Dokmegang

A thesis submitted in partial fulfilment of the requirements of Manchester Metropolitan University for the degree of Doctor of Philosophy

Centre for Advanced Computational Science (CfACS)
Department of Computing and Mathematics
Faculty of Science and Engineering
Manchester Metropolitan University

2020

Abstract

The development of multicellular organisms remains one of the most enduring puzzles of science. While wet lab methods have proven effective in unravelling multiple mechanisms, much is yet to be discovered. Computer simulations are increasingly used in this context and present over wet lab experiments the advantages of simplicity, reduced risk and total control over experimental conditions and parameters. Hence the need for more computational models and studies establishing their usefulness for biologists. In this work, we present a novel agent-based computational model of cell and tissue mechanics (MG#) of the family of Deformable Cell Models, able to simulate various phenomena in morphogenesis. Furthermore, we show that MG# can be extended to couple mechanical and chemical variables describing the dynamics of a cell within a unified framework. Using MG#, we reproduce key morphological events of mouse implantation and, for the first time, provide theoretical evidence that trophectoderm morphogenesis can regulate epiblast shape upon implantation. Moreover, enriching centre-based models with a polarity term, we show that directed cell behaviours are a sufficient drive for zebrafish fin development. Together, the results presented in this thesis offer key insights into morphogenesis, highlight the usefulness of agent-based modelling methods in the study of embryogenesis, and propose new mathematical models, and computational tools purposed for the investigation of early development.

Contents

Acknowledgements

I would like to express my sincere gratitude to my former Director of Studies and supervisor Dr Rene Doursat. He saw potential in me right from the application stage, and offered me the amazing opportunity to pursue these doctoral studies. Indeed during this journey, his continuous support, enthusiasm, patience, motivation, and wisdom have guided my endeavours and nurtured my embryonic research skills. I could not have imagined having a better advisor and mentor for my PhD studies.

I would also like to express my sincere gratitude to my current Director of Studies Dr. Matteo Cavaliere. Even before joining my supervisory team, we had a good working relationship. After joining my supervision as Director of Studies, he quickly stepped up to the role of a mentor. His practical wisdom, administrative skills, and research experience significantly helped me get through the demanding last months of my studies.

I would like also to thank the rest of my supervisory team in the persons of Prof. Liangxiu Han, Dr. Moi Hoon Yap, and Dr. Sylvester Czanner. They have often provided timely encouragements, fresh eyes, out-of-the-box critical thinking, but also for challenging questions that have incited me to widen my research from various perspectives.

This thesis project is one of fourteen within the EU Horizon 2020 Innovative Training Network ImageInLife. I would like to thank Prof. Georges Lutfalla of the University of Montpellier, our Project Leader, along with all Principal Investigators for initiating the ImageInLife framework, thus contributing in my thesis in multiple ways. My gratitude goes particularly to Prof. Magdalena Zernicka-Goetz and Prof. Nadine Peyrieras, who respectively provided me with an opportunity to visit their laboraties at the

Mammalian and Stem Cell Group of the University of Cambridge, and the BioEmergences Lab of the French National Centre for Scientific Research. Without their precious support and the insightful discussions I had with them and their lab members, it would not have been possible to conduct this research. To conclude this series, my gratitude go to Mrs. Veronika Peciarova, our project manager, for always being there for us and organising everything so well.

I would then like to thank all my fellow Early Stage Researchers within ImageInLife. I have often quoted to you this thought by Eric Schmidt, former CEO and Executive Chairman of Google: "The easiest way to have a good idea is to have a lot of ideas". A lot of ideas that have shaped this thesis sprout from the many meetings and conversations we have had together. I would particularly like to thank Hanh Nguyen, our collaboration has birthed a manuscript that we co-authoured, and which constitutes a chapter of this thesis; and Antonia Weberling, with whom I had stimulating discussions that have led to interesting results.

I thank fellow PhD students at Manchester Metropolitan University. Our multiple discussions on various topics, frequent lunches, and once-in-a-while parties have kept this studies a fun adventure.

Last but not the least, I would like to thank my family: my parents, brother and sisters; and my friends, for supporting me spiritually and emotionally throughout this thesis and my life in general.

Statement of originality

I, Joel Dokmegang, hereby declare that this dissertation and the work described in it are my own work, unaided except as may be specified below. The work presented in chapter 6 is the result of a joint collaboration with colleagues at the French CNRS BioEmergences laboratory, our fellow partners within the EU Horizon 2020 Innovative Training Network Imageinlife. In this collaboration, BioEmergences provided imaging datasets consisting of tracked cell trajectories in a developing zebrafish pectoral fin (as shown in figure 6.1a). Every other analysis in this chapter and in other chapters were performed by me. The findings presented in chapter 6 were also jointly published in the form of an article in the scientific review *bioinformatics*.

Chapter 1

Introduction

Embryogenesis, which designates the formation and development of an embryo, is home to spectacular and species-consistent morphological events that gradually transform an organism from a single egg to a fully functional living being [81]. Morphological changes in embryonic tissues are driven by the coordinated dynamics of myriads of cells, the basic unit of biological life. At the subcellular stage, an impressive machinery deploys intense activity dominated by biomechanics, gene expression and molecular signalling that regulates cell states. On the one hand, cell shapes change and their movements generate the physical forces that shape the embryo. On the other hand, differences in genetic activity lead to the synthesis of various proteins that explain differentiation into distinct cell types [152]. Development is therefore the result of the interplay between two mutually influencing processes: "mechanical morphogenesis" and "chemical morphogenesis" [145]. To adopt an artistic metaphor, these tightly coupled processes can also be described as *shaping*, by which the embryo "sculpts" itself, and *atlassing*, by which it "paints" itself [35].

Following this description, modelling biological development becomes a question of how much each of these processes can be integrated into a unified mathematical and computational formulation to account for what is being observed experimentally. The many different modelling techniques currently in existence can be construed as different compromises to this problem. While approaches based solely on either mechanism have been proposed [61, 116, 146], models that couple both mechanical and chemical variables have been on the rise in recent years [15, 35, 64, 85, 90, 115, 125], and their promising results justify further investigation. Grounded on the latter, we aim in this project to build computational models that can account for both mechanical and chemical aspects of tissues dynamics, and are able to reproduce key morphological events in the early development of living organisms.

Computer simulations present numerous advantages over traditional experimental techniques, one of which is their extreme modulability, both in input and output [18]. "In silico", the experimentalist has more control over environmental conditions, and can measure any metrics of interest. Although this desirable feature eliminates risks, ethical concerns and ideally allows a more thorough investigation of the studied system, one however runs the danger of falling out of the biological domain. As a matter of fact, bio-inspired models can be pushed beyond classical biology to explore alternative forms of life [40]. This is the programme of Artificial Life, a discipline extending theoretical biology by exploring "life-as-we-know-it" within the broader context of "life-as-it-could-be", and deriving from there innovative technologies, e.g. robotic or biomedical. In real-world biological modelling however, it is crucial to keep the model outcomes in accordance with experimental observations. In this context, microscopy imaging plays a central role: observations and simulations interact in a feedback loop, whereby imaging data informs

and refines the model, which in turn raises new questions and suggests new data acquisitions [18].

In this thesis, we aim to apply this workflow to the study of key episodes of vertebrate development: mouse embryo implantation, and zebrafish pectoral fin development. For each of these studies, and taking into account their peculiarities, we propose novel approaches for modelling the biomechanics involved. For the former, we develop a novel model of cell and tissue mechanics based on established approaches in which cells can exhibit various shapes. This enables us to schematically reproduce the observed biological phenomena and quest for new insights. For the latter, we extend an existing modelling paradigm of cell mechanics to accommodate the specific requirements of the study. In order to showcase the work carried out, we propose the following outline for the rest of the thesis.

Chapter 2: Computational models of biological development A great diversity of models exist to simulate biological cells and tissues. Depending on the biological realism they include, the spatio-temporal scale they capture, or the nature of variables they manipulate (physical, chemical), models exhibit different properties and suit different purposes. Here we review computational models of biological development in the literature.

Chapter 3: MG#: A modelling framework and simulation platform for cell and tissue mechanics Building on the fundamental principles of Sub-cellular Element Models, we introduce a novel model (MG#) of cells and tissues biomechanics. In this model, a cohort of particles on the membrane and a single intracellular particle represent the biological cell. Non-linear elastic potentials between particles mimic the plasticity of cell membranes and the activity of the cytoskeleton within the cell. With

this model, cells are able to exhibit bio-realistic cell shapes and cell populations can reproduce biological tissue behaviours such as invagination of an epithelial layer or the formation of multicellular rosettes.

Chapter 4: Modelling of epithelial morphogenesis Not many biological entities are as much regulators of biological development in organisms as are epithelial tissues and their characteristic behaviours. In this chapter, we explore different mechanisms of epithelial morphogenesis. In particular, we use MG# to model and simulate epithelial processes at the scale of individual cells and tissues, including planar polarised constriction, apical constriction and its variants, epithelial folding and rosette formation. This chapter also aims at showcasing what is possible with MG# and lays foundations for the study in the next chapter.

Chapter 5: Computational modelling unveils how epiblast remodelling and positioning rely on trophectoderm morphogenesis during mouse implantation Implantation is a critical milestone in mouse embryogenesis. Upon implantation, the blastocyst undergoes significant remodelling from an oval ball to an egg-cylinder. A key feature of this transition is the symmetry breaking in the epiblast and its shaping into a "cup". We hypothesise that this event is the result of mechanical constraints originating from the trophectoderm, also going through significant transformations in this time. Using MG#, we investigate this hypothesis. Our results suggest that trophectoderm morphogenesis indeed dictates the cup shaping of the epiblast, and fosters its movement towards maternal tissue.

Chapter 6: Quantification of cell behaviors and computational modelling show that cell directional behaviors drive zebrafish pectoral fin morphogenesis How the zebrafish grows its pectoral fin from a 2D layer to a 3D structure remains a challenge in embryology. By analysing

single cell dynamics from live imaging of zebrafish embryos, we find out that during this development cells gradually align their long axis to the proximal-distal axis (PD) of the zebrafish fin. Building on this observation, we enhance the basic centre-based cell model with a polarity term and simulate fin growth, allowing proliferation. Our simulations results in 3D fins similar with shape to real ones, suggesting that directed cell behaviours, are essential to drive fin morphogenesis in zebrafish.

Chapter 7: Conclusion Here we review the landscape of the work carried out, identify its strengths and weaknesses, and present future perspectives.

Chapter 2

Computational models of biological development

2.1 A brief history of mathematical and computational models of development

Only a handful, if any, of natural mechanisms could be considered as fascinating and inspiring as morphogenesis. The formidable challenge presented by biological development, as described by Enrico Coen, is to "understand how the complex pattern and arrangement of different cell types that make up a mature organism can arise from a single cell in a consistent way each generation" [30]. In their efforts solving this self-organising puzzle, embryologists have formulated theories spanning a vast range of the natural sciences. Early attempts described it in terms of intuitive principles such as heat, wetness, and "solidification". After several centuries of enlightenment and progress, D'Arcy Thompson formally postulated that anatomical complexity emerges from the principles of physics and chemistry [143]. A major breakthrough

occurred when in 1938, Nicolas Rashevsky pioneered the field of mathematical biophysics, emphasising quantitative, metric aspects of the physical manifestations of life. In particular, he proposed a framework to describe organisms as networks in which vertices represented biological functions and oriented edges the interactions between them [123], and showed that cell polarity was possible even for spherical cells [122]. Another landmark of mathematical modelling in biology was reached in 1952 when Alan Turing showed that pattern formation in natural systems could be simulated using reaction-diffusion equations [145]. Expanding on Turing's hypothesis, Lewis Wolpert introduced the concept of *positional information*, which postulates a hidden geographical organisation of the embryo into regions of cells following different fates [152]. Over the years, more theoretical hypotheses, for example Holtfreter's "selective affinity" further refined by Steinberg's *differential adhesion hypothesis* (DAH), appeared and inspired further translation into mathematical biophysics [79, 138].

Parallel to the birth of mathematical formulations of developmental theories, computers also appeared and their use for all sorts of scientific purposes grew rapidly. Whilst handwritten equations could help solve the dynamics of a small number of cells, or evaluate a few state variables characteristic of a tissue, this new huge computational power allowed for the simulation of more complex phenomena. One of the earliest computerised simulations of vertebrate development can be attributed to Jacobson and Gordon, who designed and simulated a mathematical model of neural plate formation [77]. Their virtual experiment, backed by mathematical analysis, validated the hypothesis postulated upon experimental observation which stipulated that *shrinkage* of the surface of the neural plate and *displacement* of the entire sheet are necessary and sufficient to produce the transformation of the neural

plate from a hemispheric sheet of cells to a keyhole shape. Since then, computational modelling has gained considerable ground and positioned itself as an instrument of choice in the biologist's toolbox.

2.2 Models of biological development

Anatomical complexity in embryonic tissues emerges from the multiple interactions in which cells are involved. The dynamics of a cell originate from within itself, from the influence of surrounding cells, and from the extracellular matrix (ECM). Cells have the intrinsic ability to initiate complex movements and deformations, which they achieve through constant redeployments of their internal structures [152], first and foremost their cytoskeleton. As cell populations usually reside in densely packed arrangements, any changes in shape and position has a direct influence on neighbouring cells, which themselves undergo (passively) or trigger (actively) morphological changes in response. Several studies have established that genes are ultimately responsible for orchestrating the internal machinery of the cell by defining the properties that drive its activity [84]. Through multiple molecular pathways featuring complex networks of inhibitor/activator agents, genetic regulation establishes an anisotropic functional atlas of cells and tissues, e.g. inducing asymmetries in the distribution of force-related molecules within a single cell, thus driving deformations and migrations. In the same way that genetic activity produces forces, mechanical signals received by the cell can also be translated back into chemical signal via a mechanism called mechanotransduction.

The above description highlights the double dynamics of cellular activity, biomechanics and genetic regulation, and their tight links. Computational modelling of development is deeply grounded in this framework. On the one hand, models of cell mechanics investigate how physical forces shape the embryo. On the other hand, models of gene expression and molecular signalling examine how cells determine their states and behaviours. In the next paragraphs, we review these different paradigms, including some of their fundamental principles and results achieved.

2.2.1 Models of cell mechanics

Generally, there are two approaches when it comes to modelling cell mechanics: global or "continuum" approaches, and agent-based approaches. Continuum models are well suited for capturing large-scale dynamics in developing organisms. These models have proven useful in studying development mechanisms of various interest. Recent studies include investigating the role of topology and mechanics in uniaxial growing cell networks [59], unravelling how lumenal pressure and tissue mechanics control the embryo size [22], showing that human organoids development rely upon the contraction of the inner core of the organoid and the microstructural remodeling of its outer cortex[6], and combining muscular differentiation and differential growth to reproduce morphological patterns observed in the vilification of several species [137]. In continuum systems, however, single cells are overlooked, and focus is put on larger regions of tissues. Hence, the emergence of phenomena initiated by single cells acting in a cohort (the very essence of morphogenesis) can therefore not be fully appreciated. Agent-based models of tissue mechanics, on the other hand, allow the representation of single

cells and their heterogeneities. They can be classified into three categories: lattice-based models, centre-based models and deformable cell models.

Lattice-based models

In lattice-based models, cells reside on a fixed lattice and their dynamics consists of swapping lattice sites under certain conditions with the goal of minimising some defined global energy specific to the simulated phenomena. Simple rules prescribed at lattice level guarantee that large populations of cells can be simulated at a computationally low cost. Surprisingly, lattice-based models have been able to successfully simulate complex tissue-level behaviours including cell sorting, proliferation, cell death, differentiation and polarisation [146]. Further distinctions can be made within this category: models featuring one cell per lattice site in *Cellular Automata* (CA); multiple cells per lattice site; or one cell occupying several lattice sites in the *Cellular Potts Models* (CPM). CPM arguably constitutes the most widely used class of lattice-based models today. Inspired by the success of the large-q Ising model in reproducing the topological changes of metals and soap foams, Graner et al. [60] adapted this approach to biological cells and simulated cell sorting driven by differential adhesion, giving birth to CPM. Niculescu et al. [104] showed that CPM could realistically reproduce shape-driven migration of biological cells, in particular the crawling motion and deformation of amoeboid cells, and gliding of half-moon shaped keratocyte-like cells. Lattice-based models can also be extended to 3D, as exemplified by Belmonte et al. [10] who used CPM in 3D to simulate the in-plane elongation (in one direction) and simultaneous shortening (in the perpendicular direction) of a planar-polarised epithelial tissue, an event also known as *convergent extension*. Nevertheless, this class of models exhibit

a few drawbacks. Due to their stochastic nature, time scales are not well defined. Moreover, the simple rules that govern cell movements in these models generally do not represent biomechanics in a physically meaningful way and are hard to interpret.

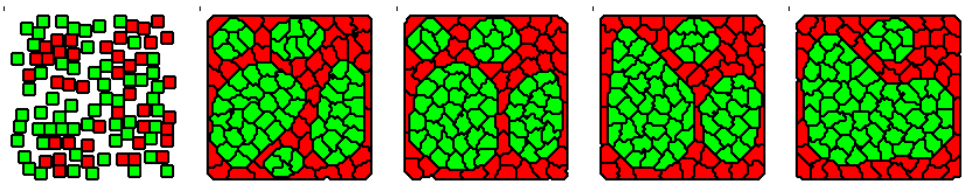

FIGURE 2.1: A population of cells, initially randomly scattered, gradually sorts itself into two regions due to differences in adhesion strength between cell types.

Centre-based models

Another class of models, *centre-based models* (CBMs), represent cells or simply their centres as single particles embedded in a highly viscous 3D environment. These models assume that, in analogy to physical particles, cell trajectories in space can be described by an equation of motion [118, 146]. Similar to lattice-based models, CBMs enable physical properties such as volume, surface area, internal pressure and mechanical stress to be defined for simulated cells. Moreover, the gained physical realism allows the explicit introduction of forces, well-defined time scales, and intuitive ways of modelling cell-cell interactions. With these models, however, the evaluation of mesoscale properties such as cell shapes remains a problem. Cells generally have a constant geometric shape, in most cases spheres. Although cell bodies usually display perfect symmetry, it is possible to simulate asymmetric cell behaviours. In order to achieve this, Delile et al. [35] define 'active'

behavioural forces underlying at once polarisation, mesenchymal cell protrusion, and epithelial cell-junction remodelling. In CBMs, cells generally interact with one another through a spring-damper system applied in their centre. This constitutes of course a crude simplification of biology, where in reality adhesion molecules act at the surface of the cell membrane, but is nonetheless sufficient in most simulations. In an attempt to improve precise cell-cell adhesion and collisions, Disset et al. [39] proposed a force applied at the centre of the *contact* surface of cell bodies and proportional to the area of this surface. Further enhancements employ established methods of contact mechanics, namely Hertzian or Johnson-Kendall-Roberts theories [118, 146]. Interesting experimentally observed phenomena have been simulated using CBMs, ranging from proliferation within monolayers [41, 88] to complex cellular rearrangements induced by intercalation observed in the enveloping layer of the zebrafish during gastrulation [34, 35].

The advantages of force-based models are a well-defined time scale, and a more intuitive way of taking into account complex interactions of cells with other cells or their environment which is why they became the standard approach.

Deformable cell models

At the higher end of biological realism integrated within a single cell are *deformable cell models* (DCMs). In DCMs the cell body is discretised into a number of vertices or 'nodes' connected by viscoelastic edges and interacting via opposite conservative forces, creating a flexible scaffolding structure with multiple degrees of freedom per cell [146].

In some DCMs, it is common to make a distinction between internal nodes, which mimic the activity of intracellular organelles, and external nodes, corresponding to the cell membrane. Newmann et al. put forward this modelling approach by introducing the *subcellular element model* (SEM) where subcellular elements (SCEs) are subjected to forces derived from a Morse potential [102]. Multiple extensions to the SEM have been proposed. Of notable interest is the work of Milde et al. [98] which introduces several new features: a modification of the potential function to increase adhesion between SCEs; cell polarity; the smooth insertion and removal of SCEs to simulate polymerisation and depolymerisation of the actin complex (leading to shape change, migration and growth); novel methods for detection of the cell membrane elements; and a special SCE representing the cell nucleus.

Although pairwise interactions between particles can accommodate cell-cell adhesion and collisions, other ways of modelling these behaviours have also been used. In addition to potentials, and to avoid overlapping between cell membranes, some authors employ specular reflections of cell particles on the membranes of other cells [50]. More accuracy may be attained through the use of established theories of contact mechanics. This is the case of Odenthal et al. [107] who rely on the Maugis-Dugdale theory of contacts between elastic bodies to investigate cell-cell and cell-substrate adhesion. However, SEM descriptions of the cell are generally too broad to take into account the specificities of epithelial cells and tissues in terms of shape and polarisation. Marin-Riera et al. [90] tackled this challenge by proposing a unified model of development enabling the simulation of both mesenchymal and epithelial cells. In their model, epithelial subelements, in contrast to mesenchymal subelements represented by spheres, are assumed to be cylindrical entities, each consisting of an apical and a basal part that can move

independently. More recently, Revell et al. [127] developed a SEM implementation able to predict the mechanical drivers of cell sorting in multicellular aggregates. Combining this model with experimental observations, the group was able to show that dynamic cell surface fluctuations, in addition to static mechanical properties, played a crucial role in the spatial segregation of the founding lineages in mammalian embryo [153]. Other SEM applications span a wide range of biological processes including the dynamics of red blood cells [50, 107], cell sorting driven by differential adhesion [150], and sea urchin gastrulation [90].

A particular class of DCMs that capture epithelial dynamics remarkably well consists of *vertex models* (VMs). VMs were created in response to the poor performance of CBMs regarding the flexibility of cell shapes in dense packings [101]. In VMs, a tissue is represented by a tiling made of non-overlapping connected polygons (each polygon corresponding to a cell), whose vertices are free to move. Vertex motion is driven by the minimisation of a potential energy of the tissue. Depending on the phenomenon to simulate and the dimensionality of the system, this potential energy may contain a certain number of terms such as: total edge length, area or volume conservation, cavity volume in blastocyst formation, or directed elongation in convergent extension [70]. VMs probably constitute the most popular class of agent-based models currently in use. Extending the work of Honda and coworkers, Okuda et al. thoroughly investigated morphogenesis using VMs [110–114].

In general, the accuracy of the mechanics in DCMs is closely correlated with the number of nodes in each cell. Depending on the application, a low number of nodes can create unrealistic dynamics, whereas a high number of nodes considerably increases the computational complexity of the model.

2.2.2 Coupling mechanical and chemical variables

Many authors have identified the need for models accounting for both mechanical and genetic/molecular aspects of cellular life, as these are tightly correlated in a feedback loop. In the context of VMs, Yu et al. [154] explain that forces might be proportional to the concentration of molecules whose activity create them, as is the case with actin-myosin driven migration forces and E-cadherin driven adhesion forces. Additionally, they advocate the necessity of using reaction-diffusion systems to model the dynamics and transport of substances through the tissue. Okuda et al. [114, 115] applied Turing's activator/inhibitor system to 3D vertex models, correlating the concentration of activator with the growth rate of individual cells. They showed that such coupling could reproduce spontaneous multicellular morphogenetic patterns including undulation, tubulation, branching, arrest, expansion, invagination and evagination.

Investigating how sharp boundaries between regions of different gene expression appear in tissues, Wang et al. [150] simulate the dynamics of an epithelium with a unified model coupling cell biomechanics through the SEM approach (model S) and gene regulation via reaction-diffusion equations (model P). The tissue is composed of two cell archetypes characterised by the preponderance of two genes (A and B), and a morphogen (M) diffusing through the tissue. Gene expression levels influence the mechanical properties of cells, and cells can ultimately differentiate into the other type. Using a new "sharpness index" metric, they show that coupling models S and P produces a better characterisation of boundaries than models S and P applied separately. Another notable work combining SEMs to GRNs was carried out by Marin-Riera et al. [90]. In their model, both mechanical and chemical variables act directly at the subcellular element level. The model

further distinguishes between enzymes, adhesion molecules and transcription factors, the latter being restricted to the nuclear SCE of each cell.

Delile et al. [34, 35] implemented mechanogenetic behaviours by integrating mechanics, gene regulation and molecular signalling in a CBM. Their model called MecaGen defines a *cell behaviour ontology* that relates cell behaviours to specific levels of concentration of proteins within cells. In this context, attraction forces are controlled by surface densities of adhesion molecules; differentiation and specialised behaviours are influenced by gene regulation; polarisation is determined by ligands and neighbouring cells; and mechanotransduction affects gene regulation.

2.3 The validation feedback loop between observations and models

As mentioned in the introduction, the crucial difference between biological modelling and bioinspired or artificial life approaches is the ultimate comparison of the model's predictions with actual biological observations. During most of the history of biological modelling, models of development have been validated or falsified based on a mere qualitative evaluation of their predictions. For a model to be judged satisfactory, it had to visually reproduce well-known morphological phenomena such as the neural plate formation [77], cavity formation or convergent extension [70], DAH driven cell sorting [58], or the sea urchin gastrulation [90]. While qualitative assessment remains an important criterion, a major paradigm shift is now underway. With the recent explosion of microscopy imaging data, models are increasingly rated on their ability to infer results that quantitatively match

experimental data. Generally, achieving acceptable levels of accuracy is a matter of optimisation of model parameters with the goal of minimising a given "fitness" energy. Different authors deal with this challenge in different ways.

Farhadifar et al. [47] use metrics based on the topology of the tissue to validate their simulations. Based on a vertex model, they investigate the influence of cell mechanics, cell-cell interactions and proliferation on the epithelial packing of the *Drosophila* wing disc. Simulating the dynamics of a proliferating epithelial layer undergoing eight cycles of division, they analyse the proportions of polygonal cell shapes and their average surface areas in the resulting tissue, and compare them with experimental data. This data consists of a network of apical junctions of 1,738 cells segmented from microscopy images of wing discs using an automated image-processing algorithm. By searching the parameter space, they discover regions where calculated network morphologies match the experimentally observed ones.

Delile et al. [35] employ topological distances measured on the tissue to validate their model and hypothesis. In examining the impact of protrusive forces and cell polarisation on the dynamics of zebrafish enveloping layer during epiboly, a parameter space search is conducted. At the end of each iteration, they make use of a fitness function to compare key properties of the simulated embryo (embryo height, yolk height, margin height, and margin diameter) to those measured on a real embryo. Parameters for which calculated data fit experimental data are found, thus corroborate their hypothesis that oriented protrusion of deep cells in the enveloping layer drives zebrafish epiboly.

Kursawe et al. [83] propose a more informed approach for parameter

space search. With the goal of determining whether vertex model parameters can be calculated from imaging data, they use summary statistics from cell packing and laser ablation experiments. With their method, the authors show that data gathered across multiple experiments generate valid parameter estimates. This data driven approach has the benefit that it further allows an estimate of the uncertainties related to these parameters, thus providing a means of evaluating confidence intervals associated with model predictions.

In summary, and despite these advances, the validation of developmental models is still a grey area of research: understanding how to best integrate and interpret experimental data with cell-based models remains a major challenge for the modelling community. In order to make the most of the available data, Fletcher et al. [53] propose an end-to-end workflow including data acquisition, analysis and fusion; model development, reduction and parametrisation; model validation/selection and guidance for future experiments.

In the area of model development, although many computational studies still rely on tailored implementations of models, there have been advances in the uniformisation in the field with the emergence in recent years of multipurpose modelling and simulation software tools. These software usually offer implementations of either single or multiple model families within open-source frameworks which modellers are able to use and extend for the benefit of their studies. The most notable packages include Chaste[99], CompuCell3D[142], VirtualLeaf[96], LAMMPS[36], Yalla [57], MecaGen[35]. With the exception of a few, most notably CompuCell3D [142], these platforms are often aimed at audiences with strong mathematical and programming skills, hence limiting the participation of stakeholders across the board

in model development. Subsequent advances will require standardisation and simplification of communication practices between scientists of various domains contributing to the field, including biologists, physicists, mathematicians and computer scientists.

Chapter 3

MG#: A modelling framework and simulation platform for cell and tissue mechanics

In this chapter, we present our model of cell and tissue mechanics, the open source simulation framework developed, and preliminary experiments of simulated morphological events. The necessity of a model featuring deformable cells arose from the need to simulate drastic cell shape changes involved morphological events such as mouse embryonic implantation (Chapter 5). As discussed in the previous chapter, two family of models are suitable for these specific modelling requirements: Subcellular Elements Models (SEM) and Vertex Models (VM). These classes of models however presented obvious limitations for our targeted use cases. On the one hand, SEM approaches often use a large number of particles, to discretise the cell, increasing the computational time and power requisite for simulations. On the other hand, Vertex Models, by using fewer particles representing in most cases only apical and basal faces of cell, are unable to account for a vast breadth of biological

cell shapes. We therefore aimed at developing a model which metaphorically bridges the gap between the two frameworks.

MG#: A Computational Model

Based on the fundamental principles of DCM, our abstraction of the biological cell features particles in interaction under the influence of conservative forces. Emphasis is put on particles at the surface of the cell membrane, bringing our model close to VM [71], while at the same time we also include a single intracellular particle reminiscent of the cell's microtubule organising centre (Fig. 3.1A,B).

On the cell membrane, we define a topological neighbourhood based on a triangulation of vertices. Two same cell particles are deemed internal neighbours if they both belong to one of the mesh triangles (Fig. 3.1C,F). We also define an external neighbourhood based on distances between particles of different cells (Fig. 3.1C,F). To minimise the computation time required, we introduce cell-cell neighbourhood relationships where particles of different cells are tested for external neighbour links only when the cells to which they belong were already approved as neighbours. The implementation of cell-cell neighbourhoods depends on the geometry of the problem at hand. In dense tissues with little variation of cell positions, depending on the geometry of cells, we opt for either a Moore neighbourhood, where a cell is surrounded by eight neighbours in its plane, or a hexagonal neighbourhood, a configuration in which most cells have six neighbours. In other cases, a metric-based cell-cell neighbourhood may be favoured.

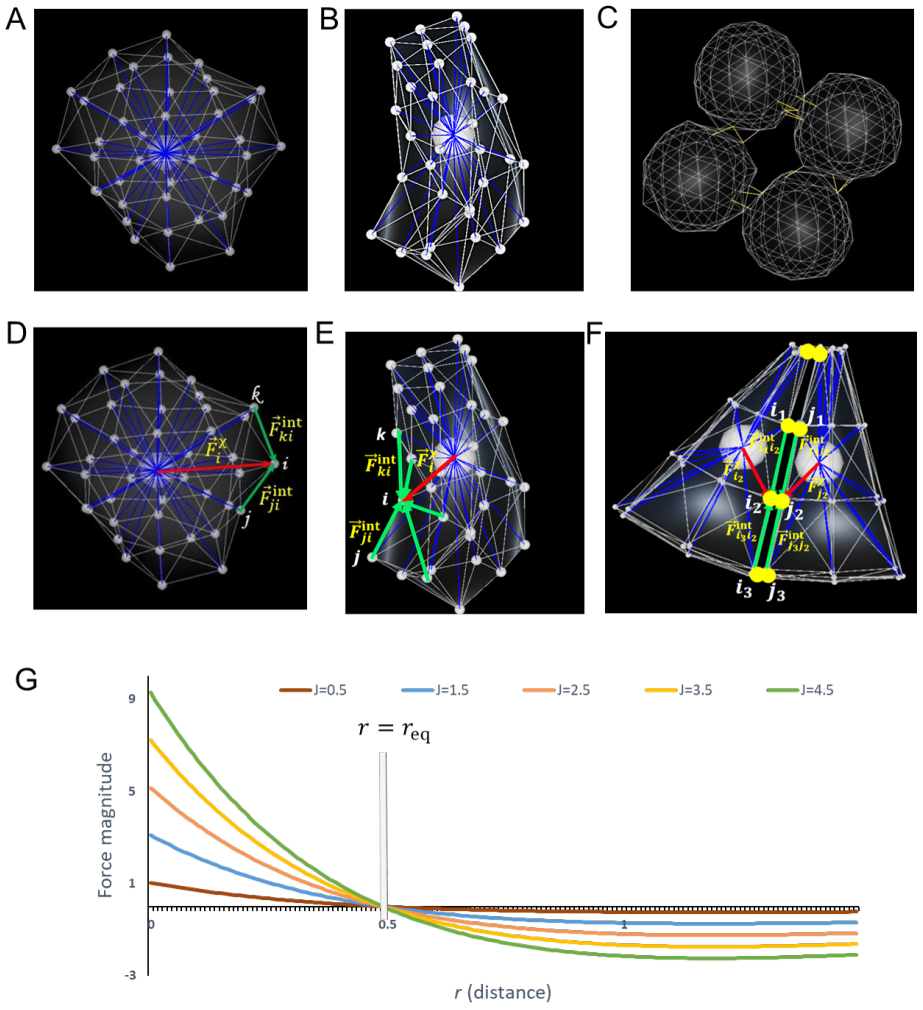

FIGURE 3.1: **Computational model (MG#). A,B.** 3D representation of cells: The cell is abstracted by an agglomeration of particles (small white spheres), whose triangulation (white edges) forms the membrane, and by an intracellular particle (big white sphere). Interactions between the intracellular and membrane particles (blue lines) mimic the cytoskeleton. Membrane particle i is under forces from neighbouring particles (j, k, ...), and from the intracellular particle χ. **A.** Cell with 42 vertices. **B.** Columnar cell with 34 vertices. **C.** A view of particle neighbourhoods in a square arrangement of four cells (nuclei not displayed). white: internal neighbourhood links. Yellow: external neighbourhood links. In this case, diagonal cells are not touching. **D,E.** Forces acting on a cell. Membrane particle i is under forces from neighbouring particles (j, k, ...), and from the intracellular particle χ. **F.** External forces acting on a cell via its particles. Here, $\overrightarrow{F}^{\text{ext}}_{i_2} = \overrightarrow{F}^{\text{ext}}_{j_2 i_2} = (\overrightarrow{F}^{\text{int}}_{j_1 j_2} + \overrightarrow{F}^{\text{int}}_{j_3 j_2}) + \overrightarrow{F}^{\chi}_{j_2}$. **G.** Plots of the magnitude of Morse forces under different values of J, with $\rho = 1$ and $r_{\text{eq}} = 0.5$.

In order to induce intrinsic mechanical behaviours within cells, we assimilate internal particle neighbourhood links to non-linear springs, which have been shown to faithfully emulate living matter [108]. These springs mimic the activity of actomyosin and microtubule networks in the cytoskeleton, and forces are derived from their elastic potential (Fig. 3.1D,E). In the cell's resting state, the equilibrium distance of each spring coincides with the length of the segment formed by its nodes. Cell dynamics arise from alterations to these equilibrium distances.

Equation of motion

Acting on a given membrane particle i, we distinguish four main types of forces: internal forces $\overrightarrow{F}_{ji}^{\text{int}}$, cytoskeleton forces $\overrightarrow{F}_{i}^{\chi}$, external forces $\overrightarrow{F}_{ji}^{\text{ext}}$, and specific forces $\overrightarrow{F}_{i}^{\text{spe}}$. Biological media are often characterised by a low Reynolds number, due to their high viscosity, which minimises the effects of inertia [146]. We therefore subject particles to an over-damped, first-order equation of motion:

$$\left(\sum_{j\in\mathcal{N}_{\text{int}}(i)} \overrightarrow{F}_{ji}^{\text{int}}\right) + \overrightarrow{F}_{i}^{\chi} + \left(\sum_{j\in\mathcal{N}_{\text{ext}}(i)} \overrightarrow{F}_{ji}^{\text{ext}}\right) + \overrightarrow{F}_{i}^{\text{spe}} = \lambda_{\text{med}}\,\overrightarrow{v}_{i} \qquad (3.1)$$

Here, $\mathcal{N}_{\text{int}}(i)$ and $\mathcal{N}_{\text{ext}}(i)$ represent the sets of internal and external neighbours of particle i, and λ_{med} is the coefficient of friction exerted on all particles.

In line with Newton's third law of motion, membrane particles entertain reciprocal forces equal in magnitude and opposite in direction with the intracellular particle. Therefore, the dynamics of the intracellular particle

are dictated by:

$$\sum_i -\overrightarrow{F}_i^{\chi} = \lambda_{\chi} \overrightarrow{v}_{\chi} \tag{3.2}$$

Here, λ_{χ} is the coefficient of friction exerted on the intracellular particle.

Internal and cytoskeleton forces

The internal force created by a particle j on a neighbouring particle i derives from a Morse potential (Fig. 3.1G). Previous studies have used Morse potentials to represent forces in a biological context [98, 102]. The expression of this force is given by:

$$\overrightarrow{F}_{ji}^{\text{int}} = 2J_{\omega}\rho\left(e^{2\rho(r-r_{\text{eq}})} - e^{\rho(r-r_{\text{eq}})}\right)\overrightarrow{u}_{ij} \tag{3.3}$$

Here, J_{ω} represents the interaction strength between particles i and j, both of cell type ω, r_{eq} is the equilibrium of the spring force between i and j, and $\overrightarrow{u}_{ij}$ is the unit vector along the direction formed by i and j. Similar forces dictate interactions between the intracellular particle and the membrane particles.

External forces

As discussed in the previous chapter, there are several approaches to implementing cell-cell interactions in the wider family of sub-cellular elements models [108]. In the scope of this work, inspired by vertex models [47], we developed a simple method to account for cell-cell interactions in epithelial tissues.

Given the tight packing in epithelial tissues, a cell membrane is always in contact with neighbouring cell membranes. Thus local action on a membrane

produces an equivalent deformation on the surrounding cells. In other words, a particle always transmits the force received to its external neighbours. To account for this behaviour, we submit particles and their external neighbours to equal forces. This is done by setting the external force acting on a particle to be equal to the sum over all its external neighbours of their internal and nucleus forces:

$$\overrightarrow{F}_i^{\text{ext}} = \sum_{j \in \mathcal{N}_{\text{ext}}(i)} \overrightarrow{F}_{ji}^{\text{ext}} \tag{3.4}$$

$$\overrightarrow{F}_{ji}^{\text{ext}} = \left(\sum_{k \in \mathcal{N}_{\text{int}}(j)} \overrightarrow{F}_{kj}^{\text{int}} \right) + \overrightarrow{F}_j^{\chi} \tag{3.5}$$

Specific forces

Generally speaking, it is possible to include specific forces in DCM to account for desired behaviours. A few studies have taken advantage of this possibility to enable for example cell surface bending resistance [108] or cell surface area and volume conservation [49]. Specific forces can be defined to complement the other three main forces when a particular behaviour is expected. Their implementation depends on the modelled event.

3.1 Computational implementation and Preliminary results

In summary, cells are represented by an intracellular particle and membrane particles. The cell shape emerges from a triangulation of membrane particle positions. Nonlinear springs between particles obey a Morse potential between nodes (membrane particles and the intracellular particle) and drive

shape changes. These springs mimic the activity of actomyosin networks in the cytoskeleton. In the cell's resting state, the equilibrium distance of each spring coincides with the length of the segment formed by its nodes. Cell dynamics arises from alterations to these equilibrium distances. Based on this principle, a number of cellular and tissue behaviours were simulated and are described here.

The computational implementation of the described model requires a time discretisation of the equation of motion. Given $\overrightarrow{X}_i^t$, λ and $\overrightarrow{F}_i^t = \left(\overrightarrow{F}_i^{\text{int}}\right)^t + \left(\overrightarrow{F}_i^{\chi}\right)^t + \left(\overrightarrow{F}_i^{\text{ext}}\right)^t + \left(\overrightarrow{F}_i^{\text{spe}}\right)^t$, respectively the position, friction coefficient and total force applied on a particle i at time point t, an explicit Euler scheme is used to calculate the position $\overrightarrow{X}_i^{t+1}$ of the particle at the next time point. If dt is the time lapse between instants t and $(t+1)$, particles update their configuration based on the following rule (Eq. 6.2).

$$\overrightarrow{X}_i^{t+1} = \overrightarrow{X}_i^t + \overrightarrow{V}_i^t \times dt \tag{3.6}$$

$\overrightarrow{V}_i^t$ is neither given, nor determined in (Eq. 6.2). An expression of $\overrightarrow{V}_i^t$ can however be drawn from the equation of motion (Eq. 6.3).

$$\lambda \overrightarrow{V}_i^t = \overrightarrow{F}_i^t \tag{3.7}$$

Hence we update particle positions in simulations according to the formula in equation (Eq. 6.4).

$$\overrightarrow{X}_i^{t+1} = \overrightarrow{X}_i^t + \frac{\overrightarrow{F}_i^t}{\lambda} \times dt \tag{3.8}$$

In the next section, we provide preliminary results of simple biology

phenomena that can be simulated with our model. We also use one of the examples (red blood cells) to show that the adopted Euler scheme is stable and converges when the time laps dt is refined.

3.1.1 Cell shapes

As the embryo develops, cells gradually lose the perfect symmetry of the initial zygote. Active phenomena such as protrusion, Epithelial-Mesenchymal Transition (EMT), or Mesenchymal-Epithelial transition (MET) [128] among others, and passive behaviours such as mechanical response to physical stress in multicellular settings foster single shape changes. For example, during gastrulation, several mechanisms of large-scale morphological change are due to cell intercalation driven by the elongation of individual cells along a particular axis [35, 102].

Accounting for various cell shapes constitutes an important requirement for our model. Globally, specific cell shapes can be obtained in two ways: either by setting particles' positions to preferential coordinates and triangulating the cell membrane accordingly, or by transitioning from an initial cell shape to a target shape. For the latter, we distinguish between two cases. Regular shapes like spherical cells, cylindrical cells or red blood cells can be modelled with analytical equations that set new equilibrium lengths for cell springs. In the next sections, we show how new equilibrium lengths for desired regular shapes can be computed. For less target regular shapes, stochastic methods such the Ising model [76] in combination with Monte Carlo methods such as the Metropolis-Hastings algorithm [11], and body similarity metrics like the Hausdorff distance [74] can be used .

3.1.1.1 Red blood cell shapes

Here, we model the relaxation of a red blood cell from a spherical shape to the biconcave shape characteristic of red blood cells. Evans et al. [46] put forward an equation to describe this shape (eq. 3.9). This equation expresses the new y coordinate changes as a function of coordinates x, y and z, with parameters a_0, a_1, a_2.

$$y'(x,y,z) = \begin{cases} D\sqrt{1-\frac{4(x^2+z^2)}{D^2}}\left(a_0 + a_1\frac{x^2+z^2}{D^2} + a_2\frac{(x^2+z^2)^2}{D^4}\right) if\ \ y \geq 0 \\ -D\sqrt{1-\frac{4(x^2+z^2)}{D^2}}\left(a_0 + a_1\frac{x^2+z^2}{D^2} + a_2\frac{(x^2+z^2)^2}{D^4}\right) if\ \ y < 0 \end{cases} \tag{3.9}$$

Hence, we deduce the following equations for new equilibrium lengths

$$\begin{cases} r_{\text{eq}}^{\chi i} &= \sqrt{x_i^2 + \left(y'(x_i,y_i,z_i)\right)^2 + z_i^2} \\ r_{\text{eq}}^{ij} &= \sqrt{(x_i-x_j)^2 + \left(y'(x_i,y_i,z_i) - y'(x_j,y_j,z_j)\right)^2 + (z_i-z_j)^2} \end{cases} \tag{3.10}$$

Figure 3.2B demonstrates this shape change.

With this example, we have an opportunity to highlight how MG# differs from other vertex-based approaches. Generally, vertex models do not feature intracellular particles. Hence, the forces that shape the cell emanate exclusively from membrane particles interactions. In order to emulate this behaviour in this context, we ran new simulations of cell shape transformation from spherical to RBC shape, this time suppressing the action of cytoskeleton forces and allowing the cell to remodel under the sole influence of membrane forces. We observed that particles did not rearrange in the previous configuration that outlined the biconcave shape. Rather, though the cell relaxes to a steady state, it maintains a convex shape (Fig. 3.2C).

We also take advantage of this example to examine the numerical stability and convergence of our model. To test these properties, we conducted further simulations in which we varied the time step (dt) over multiple level of magnitude. Additionally, we introduce the notion of the elastic energy of a cell (E) to measure how well the cell has reached the equilibrium state of the target shape. This energy is defined as the sum over all cell springs of the squared difference between equilibrium and actual lengths (Fig. 3.11). In their resting states, cells springs have the same elongation as their equilibrium lengths. Hence, cells exhibit the property that their elastic energy equals zero at rest.

$$E = \sum_{s \leq N_k} (r_{\text{eq}}^{ks} - r^{ks})^2 \tag{3.11}$$

Here N_k is the number of springs in the cell (k).

For each simulation, we plotted the evolution of the elastic energy per time. Figure 3.3 shows the outcomes of these simulations. Whereas higher time steps ($dt = 0.35, dt = 0.3$, Fig. 3.3B, *blue, yellow*) yielded unstable simulations where the elastic energy indefinitely oscillated around non zero values, lower time steps ($dt = 0.25, dt = 0.1, dt = 0.01, dt = 0.005$, Fig. 3.3B, *green, red, purple, brown*) not only produced simulations where the elastic energy converged towards zero, but the curve also exhibited stability. In the latter category, smaller time steps ($dt = 0.01, dt = 0.005$) however needed more simulation time to fully converge.

3.1.1.2 Cell elongation

Here, we model the elongation of a cell from a spherical shape to that of a cylinder. Because of the spherical symmetry of the initial cell, we can

use the parametric representation of a sphere (eq. 3.12), with coordinates (x, y, z) relative to the cell centre.

$$\begin{cases} x &= R\sin\theta\cos\varphi \\ y &= R\cos\theta \\ z &= R\sin\theta\sin\varphi \end{cases} \tag{3.12}$$

If we assume that the new ellipsoidal cell will be characterised by radius and height (h, r), the shape change from spherical to cylindrical will require that new positions of particles in the elongated cell satisfy equation 3.13.

$$\begin{cases} x' &= \frac{a}{R}x \\ y' &= \frac{b}{R}y \\ z' &= \frac{c}{R}z \end{cases} \tag{3.13}$$

Combining (eq. 3.12) and (eq. 3.13), we then have the following relationships between initial and target coordinates.

$$\begin{cases} x' &= \frac{a}{R}x \\ y' &= \frac{b}{R}y \\ z' &= \frac{c}{R}z \end{cases} \tag{3.14}$$

We can therefore compute required equilibrium lengths for springs ij and χi by computing particle distances from their new positions.

$$\begin{cases} r_{\text{eq}}^{\chi^i} & = \sqrt{\left(\frac{ax_i}{R}\right)^2 + \left(\frac{by_i}{R}\right)^2 + \left(\frac{cz_i}{R}\right)^2} \\ r_{\text{eq}}^{ij} & = \sqrt{\left(\frac{ax_i - ax_j}{R}\right)^2 + \left(\frac{by_i - by_j}{R}\right)^2 + \left(\frac{cz_i - cz_j}{R}\right)^2} \end{cases} \tag{3.15}$$

Figure 3.2A demonstrates this shape change.

3.1.1.3 Epithelial cell shapes

Here, we model the transformation of a cell from a spherical shape to that of a cylinder. Because of the spherical symmetry of the initial cell, we can use the parametric representation of a sphere (Eq.3.16), with coordinates (x, y, z) relative to the cell centre.

$$\begin{cases} x & = R\sin\theta\cos\varphi \\ y & = R\cos\theta \\ z & = R\sin\theta\sin\varphi \end{cases} \tag{3.16}$$

If we assume that the new cylindrical cell will be characterised by radius and height (h, r), the shape change from spherical to cylindrical will require that new positions of particles in the elongated cell satisfy equation (3.17).

$$\begin{cases} x' & = r\cos\varphi \\ y' & = hy \\ z' & = r\sin\varphi \end{cases} \tag{3.17}$$

From equations (eq. 3.16) and (eq. 3.17), we deduce that:

$$\begin{cases} x' &= \frac{r}{\sqrt{x^2+z^2}}x \\ y' &= hy \\ z' &= \frac{r}{\sqrt{x^2+z^2}}z \end{cases} \tag{3.18}$$

We can therefore compute required equilibrium lengths for springs ij and χi by calculating particle distances from their new positions.

$$\begin{cases} r_{\text{eq}}^{\chi i} &= \sqrt{\left(\frac{r}{\sqrt{x_i^2+z_i^2}}x_i\right)^2 + h^2 y_i^2 + \left(\frac{r}{\sqrt{x_i^2+z_i^2}}z_i\right)^2} \\ r_{\text{eq}}^{ij} &= \sqrt{\left(\frac{r}{\sqrt{x_i^2+z_i^2}}x_i - \frac{r}{\sqrt{x_j^2+z_j^2}}x_j\right)^2 + h^2\left(y_i - y_j\right)^2 + \left(\frac{r}{\sqrt{x_i^2+z_i^2}}z_i - \frac{r}{\sqrt{x_j^2+z_j^2}}z_j\right)^2} \end{cases} \tag{3.19}$$

Figure 3.2D demonstrates this shape change.

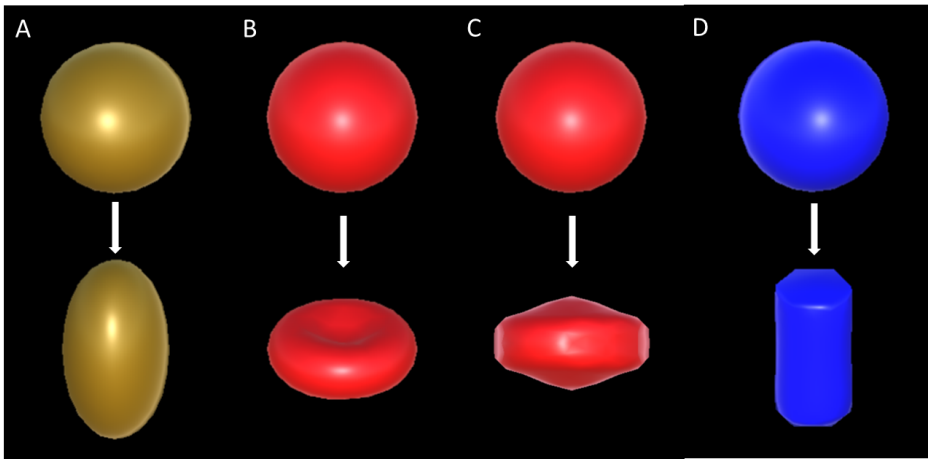

FIGURE 3.2: **Regular cell shapes obtained by shape metamorphosis**. **A**. Top: initial spherical cell. Bottom: Ellipsoid cell shape representing an elongated cell. Parameter values: $a = 0.707, b = 1.25, c = 1$ **B**. Top: initial spherical cell. Bottom: Biconcave cell shape characteristic of Red Blood Cells. Parameter values: $a_0 = 0.0518, a_1 = 0.0518, a_2 = -4.491$. **C**. Top: initial spherical cell. Bottom: Red Blood cells biconcave shape is not attained when radial forces are suppressed, though simulation time is 10 times longer than in **C**. Parameter values: $a = 0.707, b = 1.25, c = 1$. **D**. Top: initial spherical cell. Bottom: Cylindrical cell shape characteristic of epithelial cells. Parameter values: $h = 1, r = 0.5$.

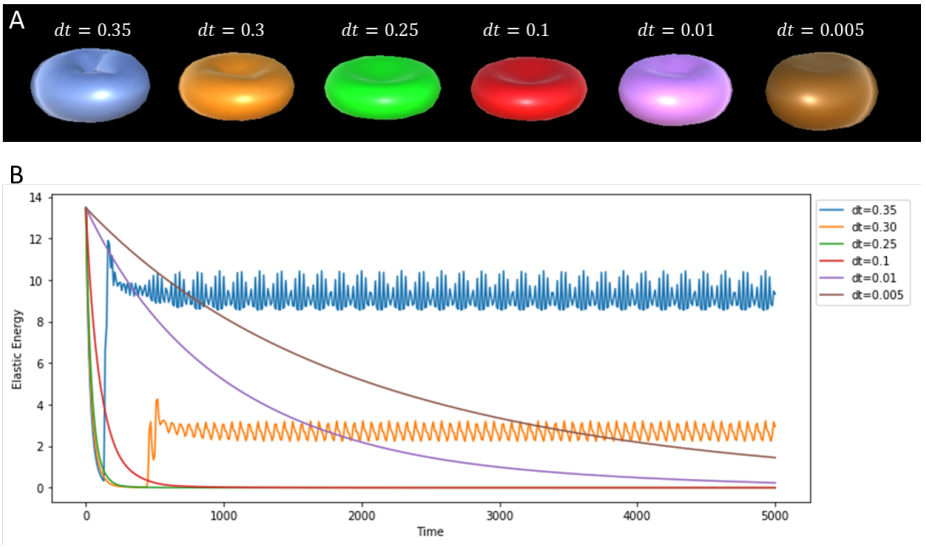

FIGURE 3.3: **Convergence of Red Blood cell Shapes**. **A**. Cell shapes obtained for different values of the simulation time step. **B**. Elastic energy charts for different simulation scenarios. Higher time steps converge towards non-zero values, but yield unstable simulations (*blue, yellow*). Lower time steps converge towards zero and yield stable simulations (*green, red, purple, brown*). In each of these simulations, we use parameter values $a_0 = 0.0518, a_1 = 0.0518, a_2 = -4.491$.

3.1.2 Apoptosis

Biological life is an equilibrium between life and death. In order for organisms to live and develop, new cells need to be born, while old cells need to die. Apoptosis, which designates the programmed death of biological cells, is one the mechanisms that mediate the right balance between life and death in living beings. Dysfunctional control of cell birth and death mechanisms lead to several physiological diseases including cancers [33, 89]. Apoptosis is also very instrumental in other development processes such as the separation of digits [140].

Here, we propose to simulate apoptosis by gradually reducing the volume of the cell. For this, we shrink all cell spring equilibrium lengths to

zero. As a response, the cell spring lengths decrease until the cell reaches a negligible volume (Fig.3.4).

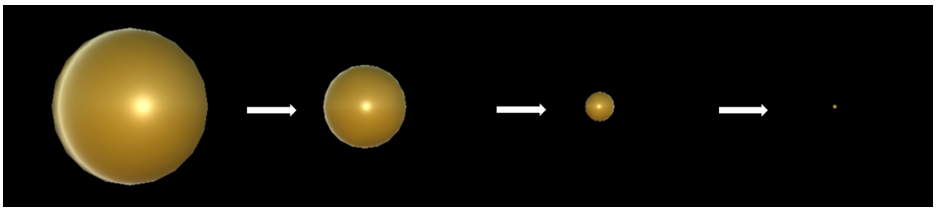

FIGURE 3.4: **A cell undergoing apoptosis**. A cell decreases in volume until it vanishes

3.1.3 Cell polarity

Polarity is an important property of biological cells. In epithelial tissues, cells exhibit an apico-basal polarity with a strict distinction between their basal and apical faces. This type of polarisation enables absorptive epithelia to extract materials from a particular side of the sheet [55], or form multicellular structures such as tubes [28], or rosettes [65]. Mesenchymal cells, on the other hand, feature polarity through mechanisms such as protrusion, which induce directed shape changes and cell movement [57]. Polarisation, along with apoptosis, appears to play a critical in lumenogenesis [33, 155].

In MG#, we propose to model polarity by assigning to a membrane particle the lead role in the cell. In this way, the said particle defines the orientation and polarity of the cell. Figure 3.5 shows different scenarios of orientation for apico-basal polarity of an epithelial cell. The different cells have been obtained by shape transformation of the same initial spherical cell.

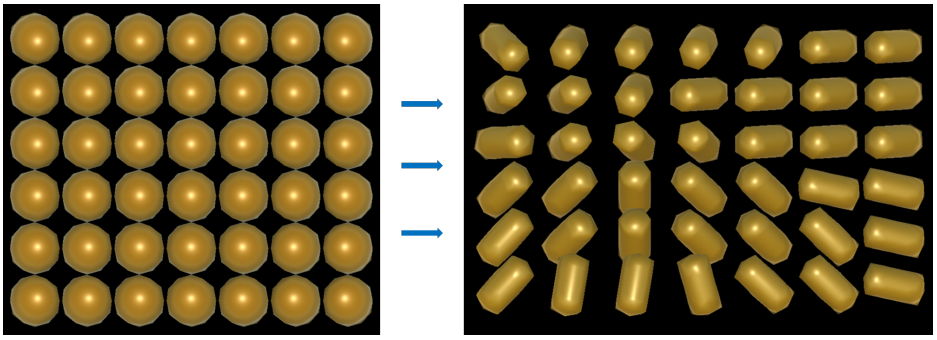

FIGURE 3.5: **Cell Polarity**. Different spatial orientations for the apicobasal polarity of an epithelial cell. In each case, the epithelial cell has been obtained by shape metamorphosis of an initial spherical cell. A different polarity orientation has been specified for each cell.

3.1.4 Cell cycle and division

Cell cycle is a mechanism at the heart of morphogenesis. From the zygote stage to the adult vertebrate, cell growth and division ensure that the organism develops and renews its organs. We implement a simple cell cycle with a cycle period for each cell. While going through their cycle, each cell increments its internal clock, then divides into two cells when their counter reaches the cycle period.

The process of division takes as input the cell's mesh and outputs two meshes corresponding to the daughter cells (Fig. 3.6). It starts with computing the division plane, which is fully determined by a normal vector ($\overrightarrow{n}$) and a characteristic point (O). The normal vector is either explicitly given as a parameter, or numerically determined by computing the elongation axis of the cell. For symmetric division, we use the centre of the cell as characteristic point. Our model may also account for asymmetric division by choosing a point different from the centre of the cell to compute the division plane. Having set the division plane, each particle's position relative to this plane (P_i)

is determined by evaluating the sign of the dot product $\overrightarrow{OP_i} \cdot \overrightarrow{n}$, and using the terminology 'above' if it is positive and 'below' otherwise. This operation partitions the cell mesh into two distinct sets: the 'upper mesh', made of all particles whose relative position to the plane is above, and the 'lower mesh', consisting of particles which are below the plane. However, these meshes are not equivalent in terms of number of particles and topology. In order to preserve these characteristic features of our model, we extend each mesh with new particles obtained by an orthogonal projection on the division plane of the other mesh's vertices.

In the cleavage simulation below (Fig. 3.6), a single cell (zygote) goes through a series of successive divisions. At each division, the division plane is chosen such that its normal vector maximises the dispersion of the cloud point (formed by the cell particles) around their centre of mass. The vector is determined by calculating the co-variance matrix of the cloud point and then computing the eigen vector corresponding to the minimal eigen value.

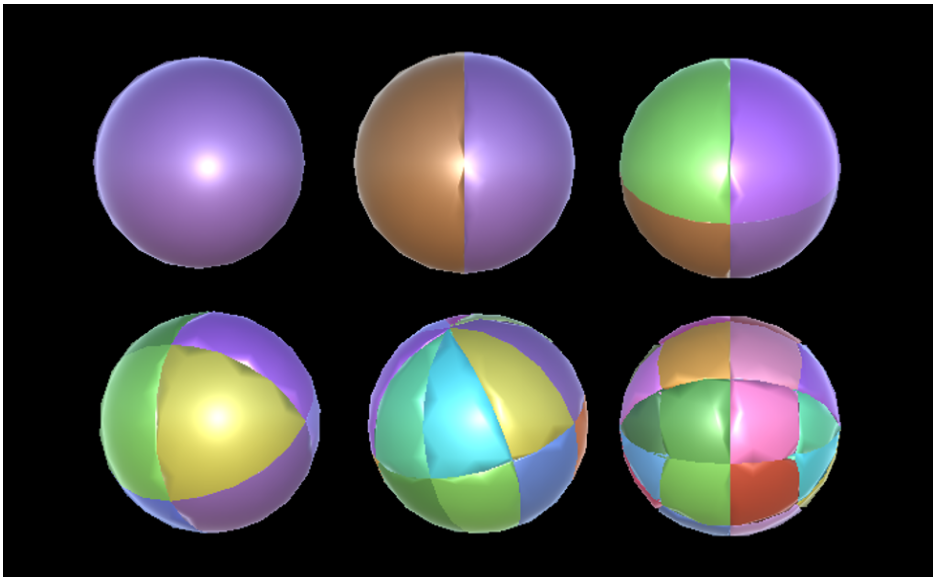

FIGURE 3.6: A simulated cell going through a series of successive divisions

3.2 MG#: The open simulation framework

To produce simulations based on our model, we initially built a modelling platform within the game engine Unity[1]. It had the advantage of offering a unique environment for programming, running and viewing simulations. However, combining at every time step the computation of particle configurations together with their rendering significantly slowed down the whole process. In addition, once a simulation was done, all results were lost and should the same experiment be run again, it was not possible to reuse or play back the previous calculations. Furthermore, a unity-based simulation platform could not allow us to run simultaneously multiple variants of a simulation.

To overcome these limitations, and following the lead of Chaste, an open source library for computational biology and physiology [99], we adopted a design principle driven by Dijkstra's separation of concerns [37]. We opted for a separation of computing and visualisation into two distinct programs. On the one hand, we developed in C# a custom back-end physics engine specific to our model, and independent from any graphical interface, based on implementations of algebraic and geometric primitives described by Hardy and Steeb in their book [66]. Figure 3.7 gives a brief overview in UML representation of the class diagram of MG#. This new physics engine updates at every time frame cell particles' positions and thus the spatial configuration of simulated cell populations. At the end of simulations, the physics engine logs these configurations to log files using either the well established VTK format, or our custom format (*.MG files*), which has the advantage of producing overall more compact logs. On the other hand, we developed a Unity-based viewer to render simulations logged in our custom (Fig. 3.8).

[1] https://unity3d.com

VTK log files can be rendered with open source visualisation tools such as paraview [1].

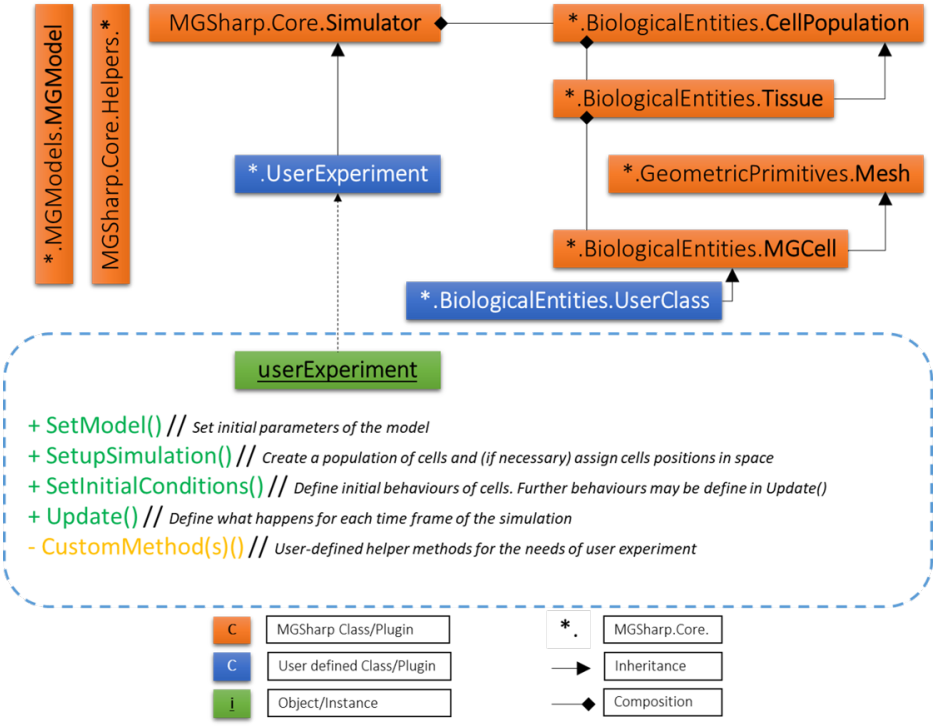

FIGURE 3.7: **MG# Class Architecture**. An MG# user experiment **.UserExperiment* (blue) is implemented in the form of a simulation class which inherits from the base simulator class (*MGSharp.Core.Simulator*). A simulation is performed on a population of cells (**.BiologicalEntities.CellPopulation*), which may be partitioned into tissues (**.BiologicalEntities.Tissue*), which themselves are specific cell populations. Each cell population or tissue is made of cells (**.BiologicalEntities.MGCell*), whose representation in the 3D space are geometric meshes (**.GeometricPrimitives.Mesh*). The generic mesh class is built upon more elementary geometric classes not shown here (vector, face, etc.) and extended from Hardy and Steeb implementations [66]. The generic *MGCell* can be specialised further into child classes with specific behaviours (**.BiologicalEntities.UserClass*). Helper classes and methods (*MGSharp.Core.Helpers.**), and the generic model class (**.MGModels.MGModel*) that contains the definition of most generic model parameters, are transversal to this architecture, and can be used at any level. An instance of a user experiment class (green, underlined) implements inherited methods from the Simulator class, and may define custom methods.

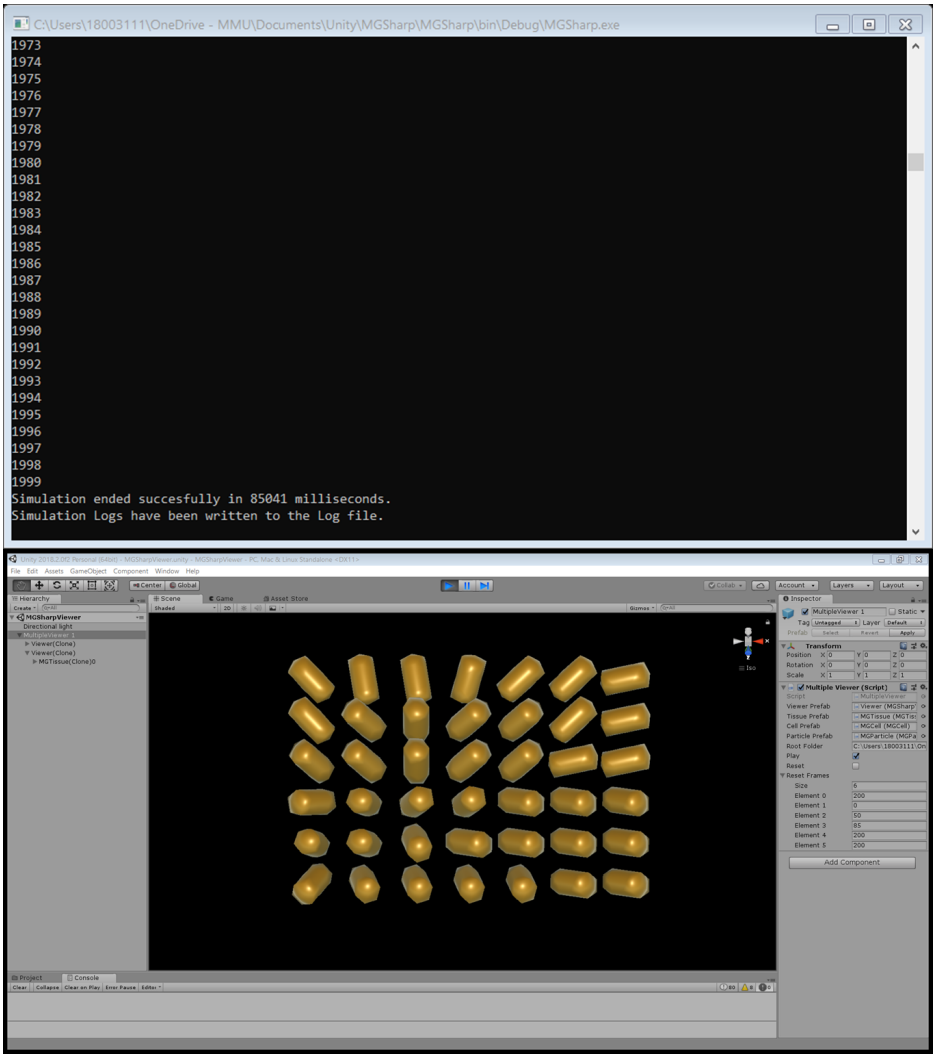

FIGURE 3.8: Simulation framework: GUI-less physics engine and viewer

Chapter 4

Modelling of epithelial morphogenesis

Epithelial sheets can be defined as densely packed arrays of cells tightly connected at their junctions to form layers of cells. Their inherent rigid topology confers them natural functions of acting as barriers and selective filters [55]. Epithelial sheets are intensely present in adult organisms. They form the tissues that absorb nutrients and metabolites from the environment, and make up the tubes, canals and cavities of glandular organs. They are responsible for transport, filtration, the synthetic functions of endocrine and exocrine, and for maintaining different electric potentials between parts of the body [82]. However, of much more interest to us, epithelia play a central role in morphogenesis: the complex geometry of embryos and organs can often be traced back to biomechanical processes occurring within epithelial sheets [32, 69]. Spectacular cellular arrangements during key morphogenesis events such as Neural Tube Closure in *Xenopus* [25], the formation of the ventral furrow during *Drosophila* gastrulation [19], or the remodelling of mouse embryonic and extraembryonic tissues during implantation [8, 9, 26],

are all driven by epithelia. In general, epithelial tissues present a set of canonical behaviours from which proceed the basic structure of most organs. These include tissue elongation or shortening, folding, spreading, budding, cavitation, and delamination of epithelial sheets [69, 82]. Here, we would like to show how we can use the model presented in the previous chapter to simulate a subset of these canonical behaviours.

In biological development, higher scale processes often emerge as a result of lower scale dynamics. This key feature of morphogenesis is present in epithelial sheets, where tissue morphogenesis is inextricably linked with questions of cell behaviour[55]. However, cell shape changes may proceed from either active or passive response to the mechanical stress or chemical signals they receive [32]. For instance, Apical Constriction (AC), which is known to be one of the mechanisms driving bending in epithelial sheets, has been shown to be a result of lower scale cellular biochemical processes [131]. On the other hand, cells transition from squamous to columnar shape might be tributary to stresses imposed by tissues' boundaries [26, 32]. However, in both scenarios, understanding the processes by which shape changes in epithelial tissues are brought about require the study of how their elementary units, epithelial cells, behave. Furthermore, even when the action of individual cells trigger epithelial morphogenesis, the coordination of such action remains essential to the formation of coherent tissues[55]. In the first part of this chapter we will focus on modelling the behaviours of single epithelial cells. From there, we will move on to address the coordinated implementation of these behaviours in epithelial sheets to simulate emergent phenomena.

4.1 Morphological changes in single epithelial cells

In this section we show how we can use MG# to model single epithelial cell shape changes. Here, we consider modelling the mechanics of Planar Polarised Constriction (PPC), Apical Constriction (AC) and Expansion, Apical Constriction with volume conservation. Finally, we examine how we can integrate chemical variables to simulate Apical Constriction.

To describe single cell shape changes in epithelial tissues, we use the MG# mechanical framework presented in the previous chapter. Epithelial cell shapes can be abstracted as cells with a cylindrical geometry and apical-basal polarity. In MG#, cell shape changes emanate from alterations to equilibrium lengths of cell springs. Hence, triggering these behaviours requires setting new equilibrium lengths for each cell. Because, in addition to their simple geometry, elementary shape changes in epithelial cells may also exhibit straightforward geometry, we will establish analytical equations to describe these changes. In the following equations, cell dimensions are assumed to be normalised by a standard distance, making them dimensionless, and the equations non-dimensionalised.

4.1.1 Planar Polarised Constriction

4.1.1.1 Biological motivation

Planar Polarised Constriction (PPC) is the process by which epithelial cells constrict their lateral domain. PPC exists as a consequence of Planar Polarity, which, unlike the characteristic apicobasal polarity of epithelial sheets,

is generated within the plane of the sheet[12]. This type of polarity coordinates the asymmetric distribution of molecules within individual cells, creating forces that break the symmetry of the cell and causes it to constrict laterally. Planar Polarised Constriction is known to play a role in multicellular rosette formation, convergent extension and the elongation of epithelial sheets [12, 65, 87].

4.1.1.2 Computational modelling

In this section, for purposes of simplification, we consider an epithelial cell with a square base. In analogy to biology, we simulate planar polarised constriction by shrinking the equilibrium lengths of cell springs. The closer the springs are to the constricting side, the greater we reduce their resting lengths. Here, we show how we obtain new equilibrium lengths when we target to reduce the width of the constricting face by a total length of $2d$.

We consider a 2D cut of the constricted cell as in figure 4.1B. In addition, let us consider sub-cellular vertices $M_i(R, y_i, z_i)$ and $M_j(R, y_j, z_j)$ located on the lateral side of the cell. Once the cell constricts by reducing one of its lateral sides by d, vertices M_i and M_j will have moved respectively to positions $M_i'(x_i', y_i, z_i)$ and $M_j'(x_j', y_j, z_j)$.

Equilibrium lengths of membrane spring ij and χi in the constricted cell are given by equation (4.1).

$$\begin{cases} r_{\text{eq}}^{\chi i}(d) = ||\overrightarrow{OM_i'}|| \\ r_{\text{eq}}^{ij}(d) = ||\overrightarrow{M_i'M_j'}|| \end{cases} \tag{4.1}$$

Finding equilibrium lengths necessary to constraint the cell to undergo planar polarised constriction is therefore equivalent to computing the coordinates of vertices M_i' and M_j'. Given that the same process can be used to calculate the coordinates of M_i' and M_j', we will show the steps for M_i', and use equivalent results for M_j'.

We define point $O_i(0, y_i, z_i)$ as the centre of the disc formed by the intersection of the cell and the plane containing M_i and parallel to the base of cell (see figure 4.1). Using the Chasles theorem for vectors $\overrightarrow{O_iM_i'}$, $\overrightarrow{O_iM_i}$ and $\overrightarrow{M_i'M_i}$, we can write:

$$\overrightarrow{O_iM_i'} = \overrightarrow{O_iM_i} - \overrightarrow{M_i'M_i} \tag{4.2}$$

The Thales theorem applied to the triangle $(A'BA)$ yields

$$\frac{||\overrightarrow{M_i'M_i}||}{||\overrightarrow{A'A}||} = \frac{||\overrightarrow{M_iB}||}{||\overrightarrow{AB}||} \tag{4.3}$$

Hence

$$||\overrightarrow{M_i'M_i}|| = \frac{||\overrightarrow{M_iB}||}{||\overrightarrow{AB}||}||\overrightarrow{A'A}|| \tag{4.4}$$

Meanwhile, $\overrightarrow{O_iM_i}$ and $\overrightarrow{A'A}$ are co-linear, and

$$\overrightarrow{A'A} = \frac{d}{R} \times \overrightarrow{O_iM_i} \tag{4.5}$$

Combining equations (4.2), (4.3), (4.4) and (4.5), we can deduce

$$\overrightarrow{O_iM_i'} = \overrightarrow{O_iM_i} - \frac{d}{R} \times \frac{||\overrightarrow{M_iB}||}{||\overrightarrow{AB}||}\overrightarrow{O_iM_i} \tag{4.6}$$

Hence,

$$\overrightarrow{O_iM_i'} = \left(1 - \frac{d}{R} \times \frac{||\overrightarrow{M_iB}||}{||\overrightarrow{AB}||}\right) \overrightarrow{O_iM_i} \tag{4.7}$$

One can easily verify that

$$\frac{||\overrightarrow{M_iB}||}{||\overrightarrow{AB}||} = \frac{z_i + R}{2R} \tag{4.8}$$

Hence

$$\overrightarrow{O_iM_i'} = \left(1 - \frac{d\,(z_i + R)}{2R^2}\right) \overrightarrow{O_iM_i} \tag{4.9}$$

Hence, in the coordinates system, we get

$$\overrightarrow{O_iM_i'} = \begin{pmatrix} \left(1 - \frac{d(z_i+R)}{2R^2}\right) x_i \\ 0 \\ 0 \end{pmatrix} \tag{4.10}$$

Hence the coordinates of M_i', the new position of particle i in the constricted cell is given by equation (4.11).

$$M_i' \left(\left(1 - \frac{d\,(z_i + R)}{2R^2}\right) x_i, y_i, z_i\right) \tag{4.11}$$

Similarly, for a particle j with position M_j on the cylindrical cell, its position on the constricted cell will be given by equation (4.12).

$$M_j' \left(\left(1 - \frac{d\,(z_j + R)}{2R^2}\right) x_j, y_j, z_j\right) \tag{4.12}$$

From this and equations (4.1) and (4.2), we deduce new equilibrium lengths for all springs M_iM_j and OM_i required to constrict apically our

epithelial cell.

$$\begin{cases} r_{\text{eq}}^{\chi^i}(d) = \sqrt{\left(1 - \frac{d(z_i+R)}{2R^2}\right)^2 x_i^2 + y_i^2 + z_i^2} \\ r_{\text{eq}}^{ij}(d) = \sqrt{\left(\left(1 - \frac{d(z_i+R)}{2R^2}\right) x_i - \left(1 - \frac{d(z_j+R)}{2R^2}\right) x_j\right)^2 + (y_i - y_j)^2 + (z_i - z_j)^2} \end{cases} \tag{4.13}$$

Figure 4.1C showcases a simulation of planar polarised constriction.

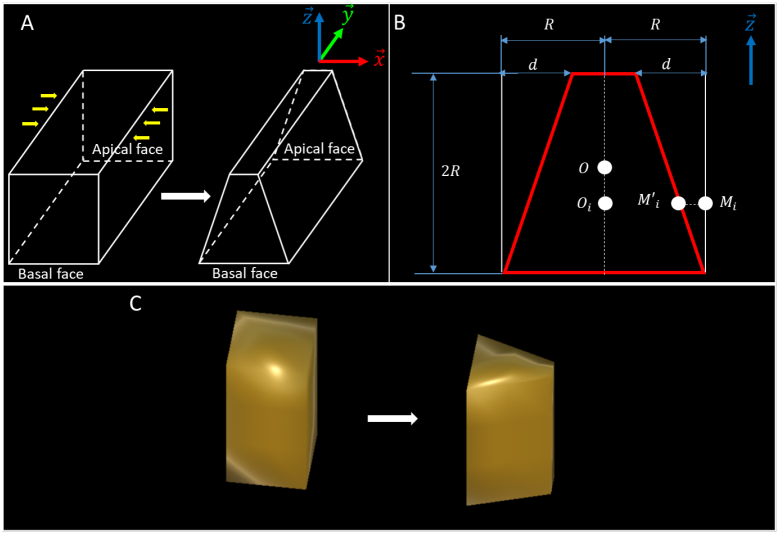

FIGURE 4.1: **Planar Polarised Constriction**. **A**. Apicobasal polarisation of a planar polarised constricted cell **B**. A 2D cut of a constricted cell. The cell underwent planar polarised constriction by reducing its lateral width by a length of $2d$. **C**. Simulation of planar polarised constriction using an epithelial cell with square base. Parameter values: $R = 0.5, d = 0.35$

4.1.2 Apical Constriction & Apical Expansion

4.1.2.1 Biological motivation

Apical constriction can be defined as the shrinkage of the apical surface of an epithelial cell. AC is the result of the contraction of actomyosin networks

near the apical face of the cell[93]. This seemingly simple behaviour of individual cell may induce dramatic changes in a sheet's morphology [92, 131]. Apical Constriction is involved in many processes driving morphogenesis in development, including the formation of tubes [3, 28], neurulation [25, 75], or during gastrulation in several species [129]. The roles and regulation of AC in development has been extensively reviewed in [91–94, 131].

Apical Expansion is the increase of the apical surface area in an epithelial cell. By definition, it appears to be the reverse process of Apical Constriction. However, several morphogenesis events involve Apical Expansion. It has been shown that Apical Expansion, under the influence of Cadherin 99C, fosters epithelial tube elongation [29]. Apical Expasion has also been found to be a driver of ascidian gastrulation [32]. Hence, we propose to simulate apical expansion, in addition to apical constriction.

4.1.2.2 Computational modelling

We simulate apical constriction (resp. expansion) by shrinking the equilibrium lengths of membrane springs. To obtain conic shapes, the new resting lengths among nodes at a given height are set to decrease (resp. increase) with the distance from the basal face. Here we will establish the expressions for new equilibrium lengths when we target to reduce (resp. increase) the apical radius (R) by a total amount of d. In order to account for both Constriction and Expansion, we allow d to be negative, however, with the constraint that $-R < d$.

We will consider a 2D projection of an epithelial cell as described in figure 4.2B. In addition, we consider sub-cellular vertices $M_i(x_i, y_i, z_i)$ and $M_j(x_j, y_j, z_j)$ located on the lateral side of the cell. Once the cell constricts

by reducing its apical radius by d, vertices M_i and M_j would have moved respectively to positions $M_i'(x_i', y_i', z_i')$ and $M_j'(x_j', y_j', z_j')$.

Equilibrium lengths of membrane spring ij for the constricted cell is given by equation (4.14).

$$\begin{cases} r_{\text{eq}}^{\chi i}(d) = ||\overrightarrow{OM_i'}|| \\ r_{\text{eq}}^{ij}(d) = ||\overrightarrow{M_i'M_j'}|| \end{cases} \tag{4.14}$$

Hence, finding equilibrium lengths necessary to constraint the cell to undergo apical constriction is equivalent to computing the coordinates of vertices M_i' and M_j'. The same process can be used to calculate the coordinates of M_i' and M_j'. Therefore, we will show the steps for M_i', and use the similar result for M_j'.

We define point $O_i(0, y_i, 0)$ as the centre of the disc formed by the intersection of the cell and the plane containing M_i and parallel to the base of cell (see figure 4.2B). Using the Chasles theorem for vectors $\overrightarrow{O_iM_i'}$, $\overrightarrow{O_iM_i}$ and $\overrightarrow{M_i'M_i}$, we can write:

$$\overrightarrow{O_iM_i'} = \overrightarrow{O_iM_i} - \overrightarrow{M_i'M_i} \tag{4.15}$$

Using the property of Thales applied to the triangle $(A'BA)$

$$\frac{||\overrightarrow{M_i'M_i}||}{||\overrightarrow{A'A}||} = \frac{||\overrightarrow{M_iB}||}{||\overrightarrow{AB}||} \tag{4.16}$$

Hence

$$||\overrightarrow{M_i'M_i}|| = \frac{||\overrightarrow{M_iB}||}{||\overrightarrow{AB}||}||\overrightarrow{A'A}|| \tag{4.17}$$

Meanwhile, $\overrightarrow{O_iM_i}$ and $\overrightarrow{A'A}$ are colinear, and

$$\overrightarrow{A'A} = \frac{d}{R} \times \overrightarrow{O_iM_i} \tag{4.18}$$

Therefore,

$$\overrightarrow{O_iM_i'} = \overrightarrow{O_iM_i} - \frac{d}{R} \times \frac{||\overrightarrow{M_iB}||}{||\overrightarrow{AB}||}\overrightarrow{O_iM_i} \tag{4.19}$$

Hence,

$$\overrightarrow{O_iM_i'} = \left(1 - \frac{d}{R} \times \frac{||\overrightarrow{M_iB}||}{||\overrightarrow{AB}||}\right)\overrightarrow{O_iM_i} \tag{4.20}$$

One can easily verify that

$$\frac{||\overrightarrow{M_iB}||}{||\overrightarrow{AB}||} = \frac{y_i + \frac{h}{2}}{h} \tag{4.21}$$

Hence

$$\overrightarrow{O_iM_i'} = \left(1 - \frac{d\left(y_i + \frac{h}{2}\right)}{Rh}\right)\overrightarrow{O_iM_i} \tag{4.22}$$

In the Cartesian coordinates system, we get

$$\overrightarrow{O_iM_i'} = \begin{pmatrix} \left(1 - \frac{d\left(y_i + \frac{h}{2}\right)}{Rh}\right) x_i \\ 0 \\ \left(1 - \frac{d\left(y_i + \frac{h}{2}\right)}{Rh}\right) z_i \end{pmatrix} \tag{4.23}$$

Hence the coordinates of M_i', image of M_i by the transformation that transforms the cylindrical cell to the cone-shaped apical constricted cell is

given by equation (4.24).

$$M_i'\left(\left(1-\frac{d\left(y_i+\frac{h}{2}\right)}{Rh}\right)x_i, y_i, \left(1-\frac{d\left(y_i+\frac{h}{2}\right)}{Rh}\right)z_i)\right) \tag{4.24}$$

Similarly, for a particle M_j on the cylindrical cell, its position on the constricted cell will be given by equation (4.25).

$$M_j'\left(\left(1-\frac{d\left(y_j+\frac{h}{2}\right)}{Rh}\right)x_j, y_j, \left(1-\frac{d\left(y_j+\frac{h}{2}\right)}{Rh}\right)z_j\right) \tag{4.25}$$

From this and equations (4.14) and (4.15) we deduce the new equilibrium lengths for all springs M_iM_j and OM_i required to constrict apically our epithelial cell.

$$r_{\text{eq}}^{\chi^i}(d) = \sqrt{\left(A(x_i)\right)^2 + y_i^2 + \left(A(z_i)\right)^2} \tag{4.26}$$

$$r_{\text{eq}}^{ij}(d) = \sqrt{\left(A(x_i) - A(x_j)\right)^2 + (y_i - y_j)^2 + \left(A(z_i) - A(z_j)\right)^2} \tag{4.27}$$

Here, $A(t_k) = \left(1 - \frac{d(\frac{h}{2}+y_k)}{Rh}\right)t_k$ and $x_{i,j}, y_{i,j}, z_{i,j}$ are relative to the centre of the cell.

An interesting feature of these equations is that they are independent of the topology of the initial mesh, which also needs to be cylindrical in shape. Figures 4.1C and 4.1D show examples of apical constriction with two different types of cylindrical meshes, respectively with square and hexagonal base.

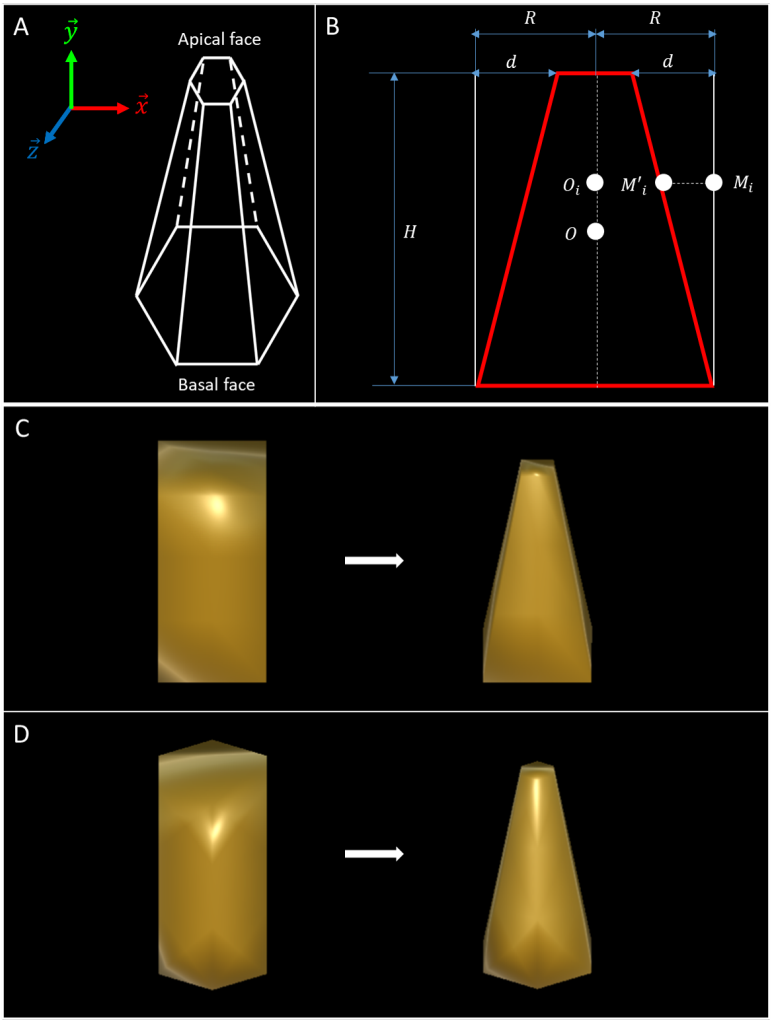

FIGURE 4.2: **Apical Constriction**. **A**. Schema of an apically constricted epithelial cell with hexagonal base. **B**. A 2D section of a constricted cell. The cell underwent apical constriction by reducing its apical radius by a length of d. Initial cylindrical section in white, constricted cell in red. **C**. Simulation of apical constriction with an epithelial cell with square base. Parameter values: $H = 2, R = 0.5, d = 0.35$. **D**. Simulation of apical constriction with an epithelial cell with hexagonal base. Parameter values: $H = 2, R = 0.5, d = 0.35$.

4.1.3 Apical constriction with volume conversation: basal-lateral modulation

4.1.3.1 Biological motivation

In several situations during their shape changes, cells attempt to maintain their volume unchanged. This feature has been observed in certain cases of Apical Constriction, where the cell, while constricting, simultaneously employs volume conservation mechanisms to compensate the loss of volume induced by the constriction of the apical side. These mechanisms involve basal modulation, in which the epithelial cell enlarges it basal face, and lateral lengthening, where the cell increases its lateral height [32, 136, 151]. These variants to AC are present in multiple morphogenesis events in epithelial tissues. For instance, there is evidence that coordination between apical and basolateral contractility is necessary for ascidian endoderm invagination [32, 136]. As in simple Apical Constriction and Planar Polarised Constriction, these shape changes are dependent on the differential localisation of activated actomyosin networks within the cell.

4.1.3.2 Computational modelling

In the scenario presented in figure 4.3B, the cell reduces its apical radius by a given amount d, and, as a consequence of volume conservation, increases its lateral height by H_0, and its basal radius by R_0. In order to enforce volume conservation on the constricting cell, we need to compute appropriate values H_0 and R_0.

Computing R_0 and H_0

We consider an epithelial cell with cylindrical shape. In its initial state, the volume of the cell is given by

$$\mathcal{V}_0 = \mathcal{B} \times H \tag{4.28}$$

Here, $\mathcal{B}$ is the surface area of the cylinder base, the specific formula for $\mathcal{B}$ depending on the actual shape of the base. In regular cylinders (with regular base), the formula for $\mathcal{B}$ will be given by

$$\mathcal{B} = \gamma \times R^2 \tag{4.29}$$

Here, γ is a multiplicative factor. For a square base, $\gamma = 4$, for the inscribed circular base $\gamma = \pi$, for the inscribed hexagonal base (inside the circle) $\gamma = 3$ etc.

Hence, the volume of the cell at its initial resting state is

$$\mathcal{V}_0 = \gamma \times R^2 \times H \tag{4.30}$$

On the other hand, once the cell is fully constricted having reduced its apical radius by d, increased its height by H_0 and its basal radius by R_0, the volume is given by

$$\mathcal{V} = \int_{-\frac{H}{2}-H_0}^{\frac{H}{2}} \gamma r'^2(y')dy' \tag{4.31}$$

Here, $r'(y')$ is the radius of the constricted cell at height y'. If the cell radius decreases in an homogeneous way, $r'(y')$ takes the form of an affine

function such that

$$r'(-\frac{H}{2} - H_0) = R + R_0 \quad \text{and} \quad r'(\frac{H}{2}) = R - d \tag{4.32}$$

Solving $r'(y')$, we get

$$r'(y') = -\frac{R_0 + d}{H + H_0} y' + R - d + \frac{(d + R_0) \times H}{2(H + H_0)} \tag{4.33}$$

Hence

$$dy' = -\frac{H + H_0}{R_0 + d} dr' \tag{4.34}$$

By a change of variable, we get the following equation for the volume

$$\mathcal{V} = \int_{R+R_0}^{R-d} \gamma r'^2 \left(-\frac{H + H_0}{R_0 + d} dr' \right) \tag{4.35}$$

$$= -\gamma \times \frac{H + H_0}{R_0 + d} \int_{R+R_0}^{R-d} r'^2 dr' \tag{4.36}$$

$$= -\frac{\gamma}{3} \times \frac{H + H_0}{R_0 + d} \left[r'^3 \right]_{R+R_0}^{R-d} \tag{4.37}$$

$$= -\frac{\gamma}{3} \times \frac{H + H_0}{R_0 + d} \left((R - d)^3 - (R + R_0)^3 \right) \tag{4.38}$$

$$= -\frac{\gamma}{3} \times \frac{H + H_0}{R_0 + d} (-d - R_0) \left((R - d)^2 + (R - d)(R + R_0) + (R + R_0)^2 \right) \tag{4.39}$$

$$= \frac{\gamma}{3} \times (H + H_0) \left((R - d)^2 + (R - d)(R + R_0) + (R + R_0)^2 \right) \tag{4.40}$$

Hence,

$$\mathcal{V} = \frac{\gamma}{3} \times (H + H_0) \left(R_0^2 + (3R - d)R_0 + 3R^2 - 3Rd + d^2 \right) \tag{4.41}$$

The volume conservation hypothesis dictates that $\mathcal{V}_0 = \mathcal{V}$. Hence, the right hand terms of equations (4.30) and (4.41) are equal. Therefore,

$$\gamma R^2 H = \frac{\gamma}{3} \times (H + H_0) \left(R_0^2 + (3R - d)R_0 + 3R^2 - 3Rd + d^2 \right) \tag{4.42}$$

Hence the following equation describing volume conservation in a constricting epithelial cell. This equation is quadratic in R_0, and linear in H_0.

$$(H + H_0) \left(R_0^2 + (3R - d)R_0 + 3R^2 - 3Rd + d^2 \right) - 3R^2 H = 0 \tag{4.43}$$

Therefore, for given values of d and R_0 such that $d \leq R$, $R_0 >= -R$ and $(d, R_0) \neq (R, -R)$, equation (4.43) gives the resulting lateral modulation.

$$H_0 = \frac{3R^2 H}{(R_0^2 + (3R - d)R_0 + 3R^2 - 3Rd + d^2)} - H \tag{4.44}$$

Conversely, for given values of d and H_0 such that $d \leq R$ and $H_0 > -H$, one can easily show that the expected basal modulation is given as in equation (4.45).

$$R_0 = \frac{\sqrt{(3R - d)^2 - 4\left(3R^2 - 3Rd + d^2 - \frac{3R^2 H}{H + H_0}\right)} - (3R - d)}{2} \tag{4.45}$$

Special case 1: Basal modulation

Here, in order to compensate for volume loss induced by apical constriction, the epithelial cell strictly increases its basal radius, keeping its height

unchanged. In this case, $H_0 = 0$ and R_0 is given by equation (4.46).

$$R_0 = \frac{\sqrt{3(3R-d)(R+d)} - (3R-d)}{2} \tag{4.46}$$

Special case 2: Lateral modulation

Here, in order to compensate for volume loss induced by apical constriction, the epithelial cell strictly increases its height, keeping its basal radius unchanged. In this case, $R_0 = 0$ and H_0 is given by equation (4.47).

$$H_0 = \frac{3R^2H}{(3R^2 - 3Rd + d^2)} - H \tag{4.47}$$

Having computed values for H_0 and R_0, we can now proceed with calculating new equilibrium distances for springs connected to point M_i'.

Computing the coordinates of M_i'

We will consider a 2D section of an epithelial cell going through apical constriction with basal-lateral modulation (Fig.4.3B). In addition, we consider sub-cellular particles i and j with respective positions $M_i(x_i, y_i, z_i)$ and $M_i(x_j, y_j, z_j)$ located on the lateral side of the cell. Once the cell constricts by reducing its apical radius by d, particles i and j will have moved respectively to positions $M_i'(x_i', y_i', z_i')$ and $M_j'(x_j', y_j', z_j')$.

Equilibrium lengths of membrane spring M_iM_j for the constricted cell is given by equation (4.48).

$$\begin{cases} r_{\text{eq}}^{\chi i}(d) = ||\overrightarrow{OM_i'}|| \\ r_{\text{eq}}^{ij}(d) = ||\overrightarrow{M_i'M_j'}|| \end{cases} \tag{4.48}$$

Hence, finding equilibrium lengths necessary to constraint the cell to undergo apical constriction is equivalent to computing the coordinates of vertices M_i' and M_j'. The same process can be used to calculate the coordinates of M_i' and M_j'. Therefore, we will show the steps for M_i', and use the similar result for M_j'.

Here we use a different approach to the previous sections. Because epithelial cells, thanks to their shape, have a cylindrical symmetry, We consider the coordinates of points M_i and M_i' in the cylindrical system of coordinates, respectively $M_i(r_i, \varphi_i, y_i)$ and $M_i'(r_i', \varphi_i', y_i')$.

To switch between cylindrical and Cartesian coordinates systems, we have the following relationships:

$$\begin{cases} x_i = r_i \cos\varphi \quad \text{and} \quad x_i' = r_i' \cos\varphi' \\ z_i = r_i \sin\varphi \quad \text{and} \quad z_i' = r_i' \sin\varphi' \end{cases} \tag{4.49}$$

While constricting, if the cell does not rotate, we can assume that the angle φ is not changed by the process.

$$\varphi_i' = \varphi_i \tag{4.50}$$

Hence, combining equations (4.49) and (4.50), we have the following equations for x'_i and z'_i:

$$\begin{cases} x'_i = r'_i \frac{x_i}{r_i} \\ z'_i = r'_i \frac{z_i}{r_i} \end{cases} \tag{4.51}$$

We have already established that r'_i can be expressed as an affine function of the y coordinate of M'_i as in equation (4.33). We found

$$r'(y') = -\frac{R_0 + d}{H + H_0} y' + R - d + \frac{(d + R_0) \times H}{2(H + H_0)} \tag{4.52}$$

Furthermore, y' can be expressed as an affine function of y, such that

$$y'(-\frac{H}{2} - H_0) = -\frac{H}{2} \quad \text{and} \quad y'(\frac{H}{2}) = \frac{H}{2} \tag{4.53}$$

We therefore get

$$y'(y) = \left(1 + \frac{H_0}{H}\right) y - \frac{H_0}{2} \tag{4.54}$$

Hence, We can write r' as a function of y

$$r'(y) = -\frac{d + R_0}{H} y + R - d + \frac{d + R_0}{2} \tag{4.55}$$

Therefore, we get the following equations for M_i' coordinates:

$$\begin{cases} x_i' = \left(-\frac{d+R_0}{H} y_i + R - d + \frac{d+R_0}{2}\right) \times \frac{x_i}{\sqrt{x_i^2+z_i^2}} \\ y_i' = \left(1 + \frac{H_0}{H}\right) y_i - \frac{H_0}{2} \\ z_i' = \left(-\frac{d+R_0}{H} y_i + R - d + \frac{d+R_0}{2}\right) \times \frac{z_i}{\sqrt{x_i^2+z_i^2}} \end{cases} \tag{4.56}$$

For a particle j on the cylindrical cell, its position M_j' on the constricted cell will be given by a similar equation (Eq.4.57).

$$\begin{cases} x_j' = \left(-\frac{d+R_0}{H} y_j + R - d + \frac{d+R_0}{2}\right) \times \frac{x_j}{\sqrt{x_j^2+z_j^2}} \\ y_j' = \left(1 + \frac{H_0}{H}\right) y_j - \frac{H_0}{2} \\ z_j' = \left(-\frac{d+R_0}{H} y_j + R - d + \frac{d+R_0}{2}\right) \times \frac{z_j}{\sqrt{x_j^2+z_j^2}} \end{cases} \tag{4.57}$$

From these equations (4.28) and (4.29) we deduce the new equilibrium lengths for all springs ij and χi required to enforce volume conservation during the apical constriction of an epithelial cell.

$$\begin{cases} r_{\text{eq}}^{\chi i}(d) = \sqrt{x_i'^2 + y_i'^2 + z_i'^2} \\ r_{\text{eq}}^{ij}(d) = \sqrt{(x_i' - x_j')^2 + (y_i' - y_j')^2 + (z_i' - z_j')^2} \end{cases} \tag{4.58}$$

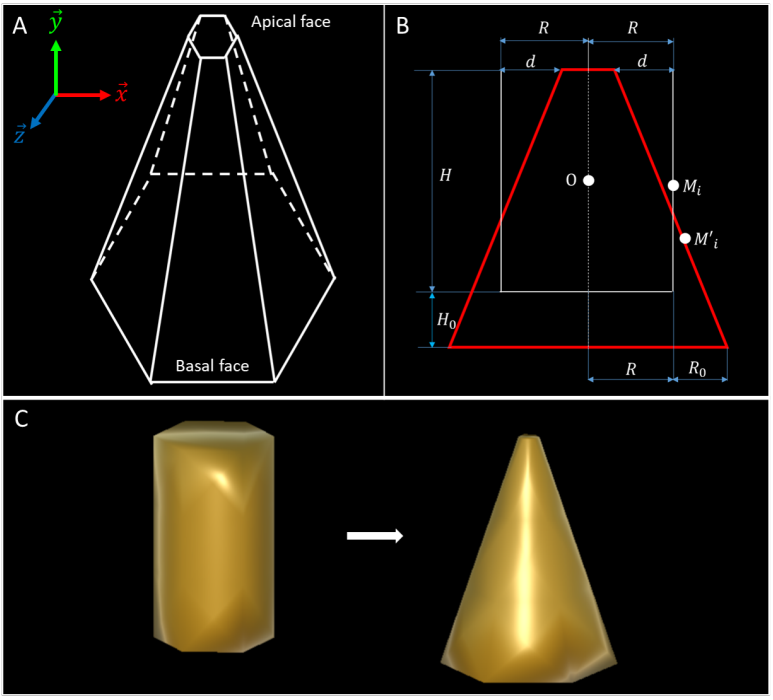

FIGURE 4.3: **Apical Constriction with volume conservation**. **A**. Schema of an apically constricted epithelial cell with hexagonal base. **B**. A 2D section of a constricted cell. The cell underwent apical constriction by reducing its apical radius by a length of d. Initial cylindrical section in white, constricted cell in red. **C**. Simulation of apical constriction with volume conservation using an epithelial cell with hexagonal base. Parameter values: $H = 2, R = 0.5, d = 0.4, H_0 = 0.25$. Using equation (4.45), we find $R_0 = 0.2618908$.

4.1.4 Integrating chemical variables: Ca-controlled Apical Constriction

4.1.4.1 Biological motivation

Several studies have provided evidence for correlation of Apical Constriction events with high concentrations of Ca^{2+} within epithelial cells. In particular, these studies have shown that periodic spikes of calcium levels preceding the enrichment in apical actin, result in pulsed contractions of cells' actomyosin networks which drive apical constriction [25, 93, 141]. In this

dynamic system, cells do not constrict all at once. Rather, AC manifests as a continuous process involving alternative phases of apical surface area shrinkage and expansion [25]. Although these studies evidenced strong correlations between the spikes and apical contractions, and established the precedence of Ca2+ spikes, the detailed chain of causation remains to be elucidated. Christodoulou et al. hypothesised that these could involve the calcium-driven activation of RhoA which in turn activates ROCK, responsible for the contraction of actin filaments [25]. Moreover, it was shown that calcium regulates the cytoskeletal dynamics of AC during mouse neural tube closure through the secretory pathway calcium ATPase-1 [20].

Furthermore, it has been established that calcium levels in Xenopus are regulated by inositol 1,4,5-triphosphate [5]. Building on these studies, Kaouri et al. [78] proposed a simple mechanochemical model capturing the dynamics of Ca^{2+} and $IP3$, as well as the interplay between their levels of concentration and changes in the apical surface area of cells. In order to demonstrate how chemical modelling can be coupled with cell mechanics in MG#, we propose an application to the control system of calcium levels during apical constriction.

4.1.4.2 Computational modelling

Calcium signalling within single cells involves the storage and release of calcium cations in and from cellular stores such the Endoplasmic Reticulum (ER) or the Sarcoplasmic Reticulum. Several conceptual modelling attempts aiming at capturing these dynamics have been put forward over the years [44]. Among those, the Atri model [5] presents the advantage of strong agreement with experimental findings [45].

Kaouri et al. [78] propose an enhancement of the Atri model which accounts for the mechanochemical feedback loop between calcium concentrations and the apical surface constriction. This model takes the form of a system of three ODEs describing the evolution over time of the molecular concentrations of Ca^{2+} (c) and $IP3$ (h), a receptor molecule in the ER, and the dynamics of the apical surface area of the cell (θ).

Here, the variations of calcium concentrations are influenced by the release of calcium from ER stores into the cytoplasm through IP3 receptors (*first term* in (Eq. 4.59)), the flux of calcium out of the cytoplasm (*negative term* in (Eq. 4.59)), and the apical surface area (*third term* in (Eq. 4.59)). Reciprocally, the variations of $IP3$ concentrations and of the apical surface area are influenced by the concentration of calcium cations in the cell. This results in the following non-dimensionalised equations ((Eq. 4.59) - (Eq. 4.61)).

$$\frac{dc}{dt} = \mu h K_1 \frac{b+c}{1+c} - \frac{\Gamma c}{K+c} + \lambda\theta = R_1(c,\theta,h;\mu,\lambda) \tag{4.59}$$

$$\frac{dh}{dt} = \frac{K_2^2}{K_2^2+c^2} - h = R_3(c,h) \tag{4.60}$$

$$\frac{d\theta}{dt} = -K_\theta\theta + \widehat{T}(c) = R_2(c,\theta) \tag{4.61}$$

In (Eq. 4.59)-(Eq. 4.61), $K_1 = k_f\frac{\tau_h}{k_1}, \Gamma = \gamma\tau_h k_1, K = \frac{k_\gamma}{k_1}$ and $\lambda = \tau S/k_1$. $k_\theta = \tau_h E'(1+\nu')\xi_1 + \xi_2$ and $T(c) = \frac{\tau_h}{\xi_1+\xi_2}T_D(c)$ and $K_2 = k_2/k_1$. Using the parameter values of Atri et al. [5], they obtain $K_2 = 1, \Gamma = \frac{40}{7}$, and $K = \frac{1}{7}$. Also, taking values of E, ν and of the viscosity from Zhou et al. [156] ($E = 8.5Pa, \nu = 0.4$ and $\xi_1 + \xi_2 = 100$Pa.s) they find that k_θ is 0.4. Furthermore, $T(c) = \frac{\tau_h}{\xi_1+\xi_2}T_D(c) = \frac{\tau_h}{\xi_1+\xi_2}T_{0D}\widehat{T}(c)$, where $\widehat{T}(c)$ is non-dimensional, and they also fix $\frac{\tau_h}{\xi_1+\xi_2}T_{0D} = 1$.

Integrating the work of Kaouri et al. [78] into our model of cell mechanics, we propose here a mechanochemical model of apical constriction, linking molecular regulation within epithelial cells to contractile forces causing apical constriction, i.e. making the mechanical parameters r_{eq} functions of certain protein concentrations h (molecular concentration of Inositol 1,4,5-triphosphate), and c (molecular concentration of Ca^{2+}).

In the previous section on apical constriction, we established for our model a mathematical link between the apical radius of a constricting cell and the mechanical forces driving the constriction (Eq.4.25). From this, we can deduce a relationship between the surface area of a constricting cell and those mechanical forces.

For an hexagonal epithelial cell with initial apical radius R, the apical surface area is given by $A_0 = (3\sqrt{3}/2)R^2$, and, for a constricted cell, whose apical radius has been reduced by d, the apical surface area is given by $A(d) = (3\sqrt{3}/2)(R-d)^2$. One can easily establish the relationship between θ, the normalised surface area, and d, given by equation (4.62) - (4.63).

$$d = \frac{1}{2}\left(1 - \sqrt{\theta}\right) \tag{4.62}$$

$$\theta = \frac{A(d)}{A_0} \tag{4.63}$$

Hence, we can express the contractile forces required to reduce cells radius by a length d as a function of the apical surface area via the constricted cells springs' equilibrium lengths $r^{ij}_{\text{eq}}(d)$ and $r^{i\chi}_{\text{eq}}(d)$, themselves functions of d (See equation (4.25)).

With these equations, we are able to establish a direct feedback loop between the chemical and mechanical variables that control the cell shape.

For a given initial state (c_0, θ_0, h_0), we can solve this system of ODEs and infer the evolution of the system over the whole simulation length. Having computed the apical surface area for each simulation frame, we can calculate the corresponding quantity d (eq. 4.62) periodically and trigger apical constriction/expansion. Figure 4.4 shows an example simulation of apical constriction regulated by AC levels.

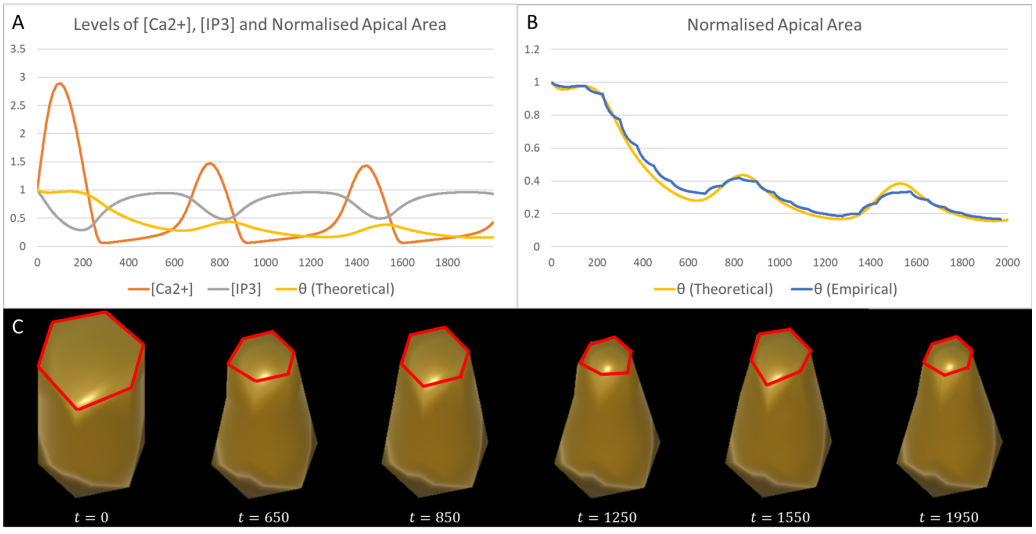

FIGURE 4.4: Ca^{2+} **regulated Apical Constriction**. **A**. Levels of concentrations of Ca^{2+} (orange) and IP3 (grey) within an epithelial undergoing AC. The yellow curve shows the theoretical evolution of the apical cell area through time. The apical faces goes through alternative phases of growth and decrease as reported in [25]. **B**. Plots of theoretical and empirical apical surface area as yielded by our simulation. Observed slight differences are caused by the Euler explicit scheme used **C**. Snapshots of the constricting cell at different time points showing the evolution of the apical surface area. Parameter values: $H = 2, R = 0.5$. From (eq. 4.59 - eq. 4.61), we fix $c_0 = 1, \theta_0 = 1, h_0 = 1, \lambda = 0.5, \mu = 0.289, k1 = 0.7$.

4.2 Morphogenesis in epithelial tissues

The bulk of epithelial morphogenesis can be broken down into interactions of a few canonical epithelial behaviours [69]. In this section, we describe and

simulate using MG# some of these canonical behaviours, notably epithelial folding and the formation of multicellular rosettes. In order to simulate these development episodes, we implement the single cellular behaviours described in previous sections in the context of multicellular epithelial sheets.

4.2.1 Folding of epithelial sheets

4.2.1.1 Biological motivation

Epithelial folding is undoubtedly one of the most common regulators of shape in development across living organisms [119]. It can be defined as the process during which a flat epithelial sheet goes out of plane by acquiring a curved shape. Folding is the main mechanism at the heart of important morphogenesis events such as gastrulation [75], Neural Tube Closure [25, 95, 141] and the formation of epithelial tubes [3, 28]. A plethora of single epithelial cells changes are able to drive the bending of epithelial sheets including different shades of apical constriction, basal expansion, and lateral modulation [119, 139, 151]. More details on epithelial folding can be found in reviews by Wen et al. and Pearl et al [32, 119, 151].

4.2.1.2 Computational modelling

Founded on the biological background of the previous section, we propose to simulate the folding of a single epithelial layer. However, here we limit ourselves to epithelial folding driven by apical constriction, the principle being the same for other drivers of folding.

It has often been suggested in litterature that during epithelial folding, single cell mechanisms at work are activated in discriminatory ways both in

space and time. Suzuki et al. [141] confirmed observations by Christodoulou et al. [25] that Ca^{2+} pulses, the biochemical metabolism fuelling AC in single cells during Xenopus Neural Tube Closure, occurred in neural plate cells rather than in the non-neural epidermis, which surrounds the Neural Plate. Hence, epidermis cells, located at the boundary of the neural plate, did not undergo AC, nor folding morphogenesis. Furthermore, Ogura et al.[109] evidenced the requirement of a timely wave of cellular contractility during epithelial invagination in *Drosophila* tracheal placode.

In order to account for this behaviour in our modelling, we speculate the presence of an *"epicentre"* within the sheet where cells actively undergo apical constriction (Fig. 4.5A). Cells beyond the epicentre (a region of space that we shall name the *"boundary"*) do not constrict apically, and only respond to the mechanical action of cells in the epicentre. In other words, the distance d by which we reduce the apical radius of a cell is a function of the position of the cell within the sheet. In this case of epithelial folding, equation (4.64) describes this function.

$$d(\overrightarrow{X_{cell}}) = \begin{cases} 0 \text{ if cell is on } \textit{boundary} \\ R \text{ if cell is on } \textit{epicentre} \end{cases} \tag{4.64}$$

The coordinated movement of cells induced by these positional laws causes the tissue to bend and fold (Fig. 4.5A,B).

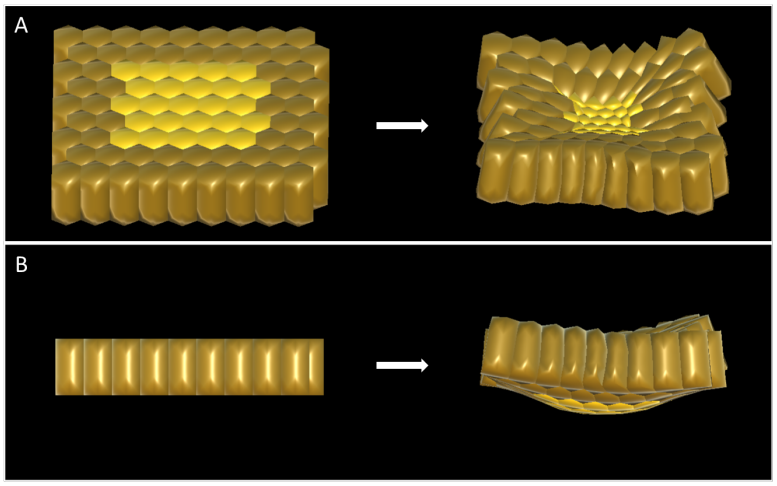

FIGURE 4.5: **Epithelial Folding**. **A**. Top view of a single epithelial layer folding under the influence of single cells at the centre of the sheet (coloured in yellow) constricting apically. The sheet is composed of 81 epithelial cells with hexagonal base. The *epicentre* is represented by the 25 yellow cells at the centre of the sheet. **B**. Lateral view of the folding process in **A**. The sheet goes out of plane. Parameter values: $h = 2, R = 0.5, d = 0.5$

4.2.2 Morphogenesis of multi-cellular rosettes

4.2.2.1 Biological motivation

Multi-cellular rosettes are concentric biological structures formed by agglomerations of polarised cells in epithelial tissues. These epithelial structures have observed across many species during development, including mouse [8, 24], *Drosophila*, chick and zebrafish [65]. Multi-cellular rosettes play an important role in several cellular behaviours: tissue elongation [3], lumen formation and maintenance of cell pluripotency [65]. In mammalian embryos for instance, they mediate the formation of a lumen in the early epiblast [8, 9, 132–134], and later the pro-amniotic cavity, bridging through embryonic and extra-embryonic tissues [24].

Like many processes in epithelial sheets, mechanisms of multicellular rosettes formation find their source in the contraction of actomyosin networks within individual cells. However, depending on the localisation of these contractions within the cell, two fundamental mechanisms have been found to drive multicellular rosette formation. On the one hand, polarised apical constriction, where actin-myosin networks localised near the apical surface of the cell constricts leading to the narrowing of the apical domain of cells. Here, polarity regulators (such as Par-3, Par-6, and atypical protein kinase C) adherens junction proteins (cadherins), and tight junction proteins (ZO-1) are responsible for the actin-myosin network localisation [8, 65]. On the other hand, polarised apical constriction [8, 65], where the network is localised near the apical surface of the cell, and planar polarised constriction, where the network is localised near the constricting lateral face of the cell [12, 65]. In both cases, cell polarity is critical to the formation of the rosette [8, 12].

4.2.2.2 Computational modelling

Founded on the biological background of the previous section, we propose to simulate rosette formation on the basis of the distinct single cell mechanisms that have been put forward as regulators of multicellular rosette formation.

The first scenario we simulate is the formation of planar rosettes (Fig. 4.6A). Here, an epithelial sheet with a relatively small amount of cells (8 cells) metamorphoses into a planar rosette by the action of single cells triggering planar polarised constriction. In the second scenario, cells in a single layered epithelial sheet constrict apically, prompting the sheet to turn into a rosette (Fig. 4.6B). Finally, in a polarised epithelial tissue with two layers, cells undergo apical constriction. This results in the emergence of a

near spherical epithelial rosette, reminiscent of mammalian embryonic tissues [132–134] (Fig. 4.6C).

In a pure mathematical sense, we can extend the idea of the positional shrinking function defined for positional folding by noticing that here also, whether a cell constrict or not depends on the position of the cell. However, in all three cases, this function is homogeneous over the tissue, and the presented simulations is equal to the initial apical radius of the cells. (eq. 4.65).

$$d(\overrightarrow{X_{cell}}) = R \tag{4.65}$$

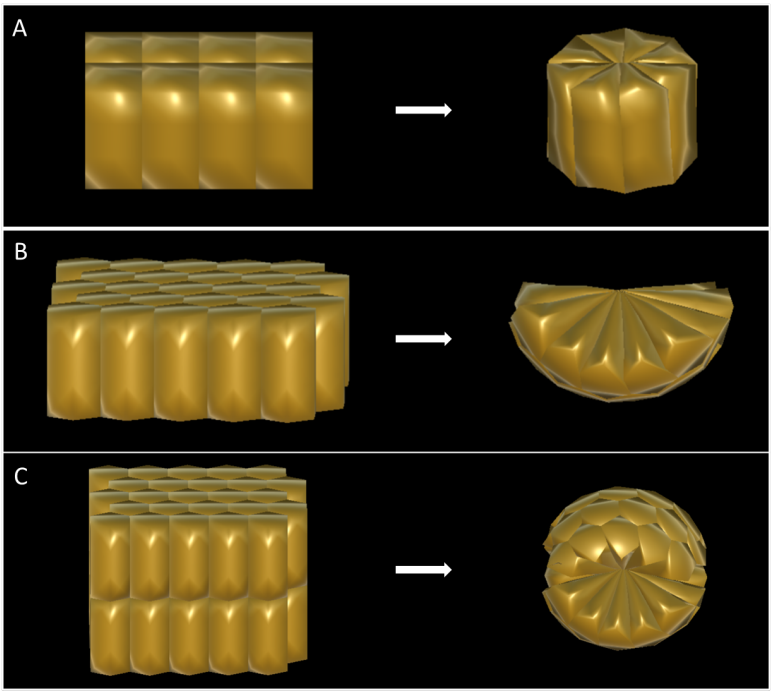

FIGURE 4.6: **Morphogenesis of multi-cellular rosettes**. **A**. Simulation of the morphogenesis of a multicellular rosette through planar polarised constriction of single cells. The cell population is made of 8 epithelial cells with square base. **B**. Simulation of the morphogenesis of a multicellular rosette via apical constriction of cells in a single-layered epithelial sheet. **C**. Simulation of the morphogenesis of a multicellular rosette via apical constriction of polarised cells in a double-layered epithelial sheet. In **B** and **C**, the the sheets are respectively composed of 25 and 50 hexagonal epithelial cells. Parameter values: $h = 2, R = 0.5, d = 0.5$

Chapter 5

Computational modelling unveils how epiblast remodelling and positioning rely on trophectoderm morphogenesis during mouse implantation

Understanding the processes by which the mammalian embryo implants in the maternal uterus is a long-standing challenge in embryology. New insights into this morphogenetic event could be of great importance in helping, for example, to reduce human infertility. During implantation the blastocyst, composed of epiblast (EPI) and trophectoderm (TE) and the primitive endoderm (PE), undergoes significant remodelling from an oval ball to an egg cylinder. A main feature of this transformation is symmetry breaking and

reshaping of the epiblast into a "cup". Based on previous studies, we hypothesise that this event is the result of mechanical constraints originating from the trophectoderm, which is also significantly transformed during this process. In order to investigate this hypothesis we propose MG#, an original computational model of biomechanics able to reproduce key cell shape changes and tissue level behaviours *in silico*. With this model, we simulate epiblast and trophectoderm morphogenesis during implantation. First, our results uphold experimental findings that repulsion at the apical surface of the epiblast is sufficient to drive lumenogenesis. Then, we provide new theoretical evidence that trophectoderm morphogenesis is sufficient to dictate the cup shape acquisition by the epiblast and to foster its movement towards the uterine tissue. We also conduct a sensitivity analysis, where we show how different sets of model parameters influence simulation outcomes. Together, these results offer mechanical insights into mouse implantation and highlight the usefulness of agent-based modelling methods in the study of embryogenesis.

5.1 Introduction

A critical milestone of mouse development is reached when the embryo implants in the maternal uterine tissue [132, 149]. Prior to implantation, a series of cell fate decisions concomitant with multiple rounds of divisions gradually transform the initial zygote into a blastocyst featuring three different cell lineages: a spherical embryonic epiblast (EPI) wrapped into two extraembryonic tissues, the trophectoderm (TE) and primitive or visceral endoderm (PE/VE) [4, 8]. Upon implantation, the embryo moves towards maternal sites, and undergoes significant remodelling, culminating in the case of

the mouse in an egg cylinder, a body structure essential to post-implantation phases such as gastrulation [8, 24**?**]. A key feature of this blastocyst-to-egg-cylinder transition, still poorly understood, is the appearance of symmetry breaking within the epiblast and its reshaping into a cup [8, 9], which occurs roughly between stages E4.5 and E4.75 of embryonic development.

Many of the important structural changes that occur during implantation have been explained in terms of chemical signals within and between embryonic and extraembryonic compartments [117, 149]. For instance, it was shown that at the onset of implantation epiblast cells exit their naive pluripotency state, self-organise into a highly polarised rosette, and initiate lumenogenesis under the influence of β1-integrin signalling [9, 133]. Shortly after implantation, β1-integrin enables pro-amniotic cavity formation along the entire egg cylinder via the resolution of multiple rosettes both in extraembryonic cell populations and at their interface with the embryonic tissue [24]. Moreover, differentiation of the primitive trophectoderm into polar and mural trophectoderm leading to the formation of a boundary between the two tissues was traced back to fibroblast growth factors (FGFs) signalling [26].

As D'Arcy Thompson already noted about genetics, however, development cannot be construed solely in terms of biochemical signals either: the mechanical interactions between cells and tissues equally and reciprocally contribute to embryogenesis [68, 143]. On the subject of the epiblast remodelling into a cup, a series of biological works have paved the way and triggered further investigation into the mechanics involved. Because it was observed that the EPI did not initiate specific tissue-level symmetry-breaking behaviours, one study stated that after the basement membrane disintegrated between the EPI and TE, the membrane between the EPI and the PE acted like a basket that moulded the epiblast into its cup shape [8] (Fig. 5.1A).

Although this hypothesis put the spotlight on the basement membrane, it also suggested that the TE in direct contact with the EPI could play a role in this shape change. Evidence supporting this hypothesis grew when "ETS-embryoids" (ETS: embryonic and trophoblast stem-cell) assembled *in vitro* from EPI and TE stem cells, surrounded by the extracellular matrix (ECM) acting as the basement membrane, replicated embryonic transition from blastocyst to egg cylinder [67] (Fig. 5.1B). Furthermore, a recent study highlighted more clearly the role of the trophectoderm [155]. In this study, ExE-embryoids (ExE: extra-embryonic ectoderm), cultured from EPI and PE stem cells separated by an ECM basement membrane, did not break the symmetry of their initial spherical shape (Fig. 5.1C). In contrast, both ETS- and ETX-embryoids (ETX: embryonic, trophoblast and extra-embryonic endoderm) made from all three blastocyst lineages did reproduce the symmetry breaking observed in real embryos. Together, these studies established the necessity of the trophectoderm for the remodelling of the epiblast [67, 155].

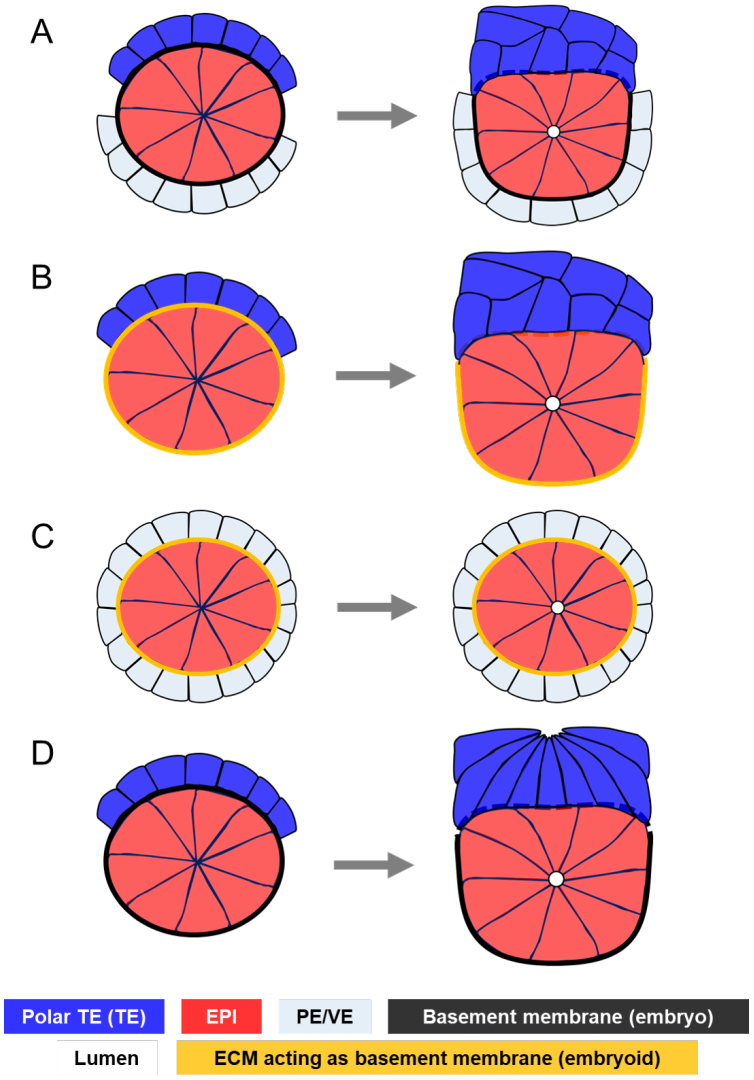

FIGURE 5.1: **Review of epiblast symmetry breaking theories. A.** The basement membrane separating the epiblast and the primitive endoderm moulds the epiblast into a cup while it disintegrates between the epiblast and the trophectoderm in mouse embryos [8]. **B.** Embryoid structures featuring epiblast and trophectoderm stem cells surrounded by an ECM acting as a basement membrane (ETS-embryoids) replicate mouse embryogenesis by forming body structures similar to those observed in normal embryonic development [67]. Here the presence of the trophecdoderm shows that this tissue might be required for symmetry breaking in the epiblast and cup shape acquisition. **C.** Embryoid structures featuring epiblast and primitive endoderm stem cells surrounded by an ECM acting as a basement membrane (EXE-embryoids) do not break symmetry in the epiblast, but initiate lumenogenesis [155]. This evidences the requirement of the trophectoderm for the remodelling of the epiblast. **D.** Trophectoderm morphogenesis during mouse implantation. Trophectodermal cells elongate, then undergo apical constriction, resulting in the tissue folding and invaginating the epiblast [26]. This suggests that epiblast remodelling into a cup might be a mechanical response to trophectoderm dynamics

On the other hand, *how* exactly trophectoderm morphogenesis influences shape change in the epiblast has not been elucidated yet because very little is known on trophectoderm morphogenesis during implantation. In the light of recent detailed descriptions of extra-embryonic tissue morphogenesis during implantation [26], it appears increasingly plausible that trophectoderm morphogenesis regulated epiblast remodelling via mechanical interactions at their common boundary. This study showed that polar trophectodermal cells exhibited drastic morphological changes throughout the implantation period. Whereas early implanting blastocysts featured squamous cells in the polar trophectoderm, these cells, driven by a high mitotic and space restrictions due to the formation of a boundary with the mural trophectoderm, later transited to cuboidal, then elongated to acquire columnar shapes. These changes were followed by apical constriction resulting in the folding of the whole tissue, and invagination of the epiblast (Fig. 5.1D). Moreover, this study provided experimental evidence that other structural changes, most notably the stretching of PE (Primitive Endoderm) cells, resulted from TE (Trophectoderm) morphogenesis [26]. Hence, we want to investigate the hypothesis that trophectoderm morphogenesis drives the remodelling of the epiblast into a cup via mechanical interactions at their common boundary.

Building on the increasing power of computational modelling in developmental biology [17, 35, 135, 147], we examine the influence of trophectoderm morphogenesis on the epiblast. The requirement of dramatic cell shape changes in trophectodermal cells, notably apical constriction [26], orients modelling options toward the family of deformable cell models (DCM) [146]. In this category, two classes of models have been predominant in recent research: vertex models (VM) and sub-cellular element models (SEM).

Although vertex models were used extensively to study epithelial dynamics [2, 52], accounting for various mechanical behaviours of individual cells remains challenging in a global energy-based approach. Hence, we set our choice on SEM, where cells are represented by an agglomeration of computational particles interacting with one another via short-range potentials emulating the viscoelastic properties of their cytoskeleton [98, 102, 130]. However, in order to exhibit realistic cell shapes, SEM generally involve an important number of particles, many of which reside within the cell, thus do not have a direct influence on cell shape. This leads to increased computational complexity, limiting the size of cell populations that can be simulated.

Here, using MG#, we first reproduce the experimental observation that repulsion at the apical surface is sufficient for lumenogenesis in the epiblast. Then, we reproduce trophectoderm morphogenesis during implantation and we provide theoretical support that epiblast remodelling into a cup shape and its movement towards the maternal uterine tissue can be explained by trophectoderm morphogenesis. We also conduct a sensitivity analysis, where we show how different sets of model parameters influence simulation outcomes.

5.2 Results

In this section, we applied our model to the study of mouse embryo morphogenesis during implantation. Here we focused on epiblast and trophectoderm tissues. First, we tested the hypothesis of whether repulsion at the apical surface of the epiblast was sufficient to account for lumenogenesis. Then, we simulated both tissues' morphogenesis and showed that the epiblast remodelling into a cup shape and its movement towards the maternal uterine tissue could be explained by trophectoderm morphogenesis. Next, we conducted

a sensitivity analysis, to show how different sets of parameters influenced simulation outcomes.

5.2.1 Repulsion at the apical surface of the epiblast is sufficient for lumenogenesis

The study of how lumens arise in epithelial tissues has revealed two predominant mechanisms: cavitation mediated by apoptosis, and hollowing, in which the lumen is formed by exocytosis and membrane separation [31, 152]. In the case of highly polarised epithelia, it was shown that cavitation was not necessary for lumenogenesis [94]. Hence, the hollowing mechanism was privileged in epiblast lumenogenesis, which features highly polarised cells spatially organised in the shape of a rosette. Moreover, it was hypothesised that repulsion mediated by anti-adhesive molecules such as podocalyxin (PCX) drove lumen formation in the epiblast [8, 9, 133, 155]. Furthermore, evidence for hollowing in the epiblast was observed in a recent study [155], where apoptosis was found not to regulate lumenogenesis, but PCX was discovered to be predominant at the apical surface of cells facing the lumen.

Using our model, we sought to determine theoretically whether hollowing via repulsion at the apical surface of the epiblast rosette was a viable mechanism for lumenogenesis in this tissue. First, we built a 3D rosette-shaped epiblast by submitting polarised epithelial cells to apical constriction [9] (Fig. 5.2A,B, Supplementary Fig. 5.6A). Then, inspired by the anti-adhesive role of PCX, we broke adhesive links between cell membranes in contact at the apical surface of the rosette, meaning that certain neighbouring pairs of particles were not more submitted to the exact same forces, but rather could be repelled in different directions.

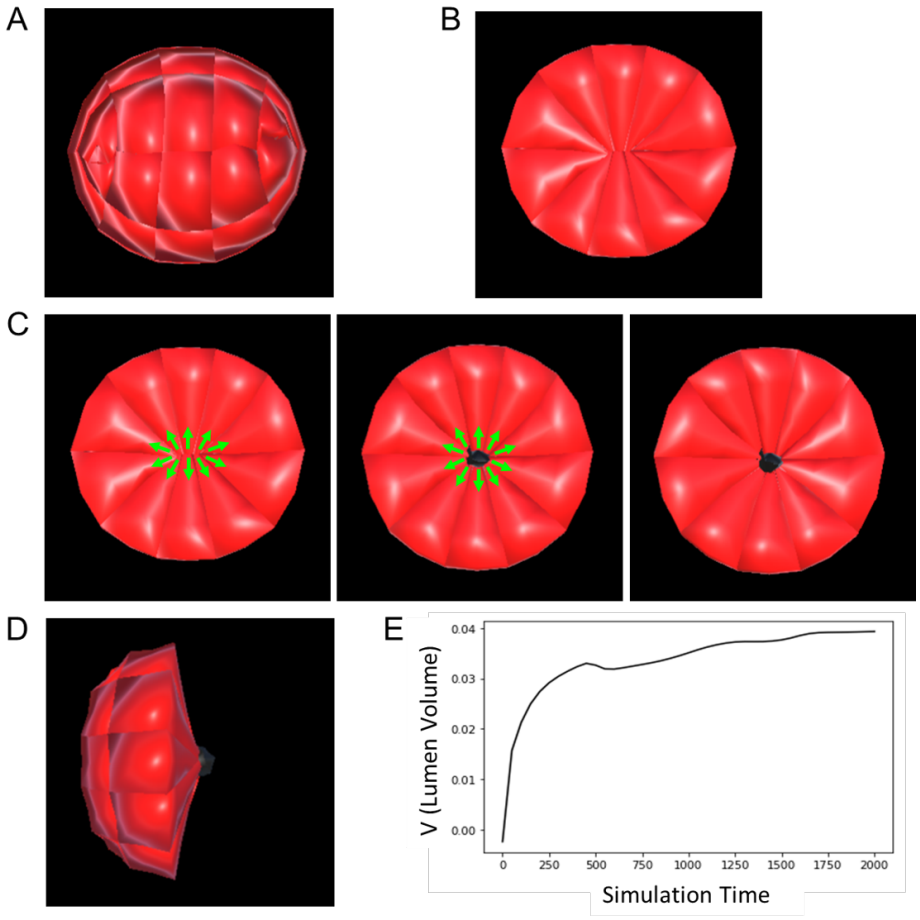

FIGURE 5.2: **Lumenogenesis in the epiblast. A.** A 3D model of a rosette-shaped epiblast. **B.** A 2D slice of the epiblast in **A** showing apically constricted cells of the building block of the epiblast rosette. **C.** Creation of the lumen cavity by repulsion at the apical surface of the epiblast. Green arrows represent the direction of repulsive forces. The snapshots (from left to right) were taken respectively at $t = 0, 500$ and 2000. **D.** Lateral view of the sliced epiblast showing the lumen volume. **E.** Dynamics in time of the volume of the lumen. Values of the equation parameters: $J_{\mathrm{EPI}} = 2.5, \lambda_{\mathrm{med}} = \lambda_{\chi} = 2, \rho = 1, R_{\mathrm{lum}} = 0.25$.

We then created a virtual source (O) at the centre of the lumen to exert repulsive forces on apical particles. Bedzhov et al. argue that these repulsion forces are driven by electrical charges [9], a possibility also explored in [43]. To model these effects, we used conservative forces from a Morse potential

(Eq. 5.1).

$$\overrightarrow{F}_i^{\text{rep}} = 2J_{\text{EPI}}\rho\left(e^{2\rho(r^{Oi}-R_{\text{lum}})} - e^{\rho(r^{Oi}-R_{\text{lum}})}\right)\overrightarrow{u}_{Oi} \tag{5.1}$$

Here, R_{lum} is the radius of the lumen. These forces prompted neighbouring apical particles and surfaces to drift apart from each other, initiate the creation of a lumen at the centre of the rosette (Fig. 5.2C-E). This result, upholding experimental data, suggests that hollowing via apical repulsion is sufficient to drive the onset of lumenogenesis in the mouse epiblast.

5.2.2 Mechanical constraints imposed by TE morphogenesis on the epiblast drive cup shape acquisition

A key feature of the blastocyst-to-egg-cylinder transition is the symmetry breaking within the epiblast and its shaping into a cup [8, 9]. During this transformation, the epiblast remodels from an oval ball to a tissue with a flat surface at its boundary with the trophectoderm. Previous studies have established the requirement of the trophectoderm in this shape change [67, 155]. Using the presented model, we investigated how trophectoderm morphogenesis influenced the cup shape acquisition by the epiblast. Our simulation protocol consisted of reproducing the sequence of morphological events observed in the trophectoderm as described in [26] (elongation followed folding via apical constriction), and keeping track of the consequent changes in the epiblast. For simplicity and to keep the model computationally efficient, we assumed that there were no cell divisions in the tissue.

We built a virtual embryo consisting of a TE sheet with initial cuboidal cells laying on top of an oval rosette-shaped epiblast (Supplementary Fig. 5.6B). At the initial stage (Fig. 5.3A,E), new equilibrium lengths were computed for all TE cells, with the goal of triggering a transition from

cuboidal cells to more elongated columnar shapes with smaller apical surface. These cells lost their resting state and regained it by gradually aligning their actual springs lengths with the calculated equilibrium lengths (Fig. 5.3B,F). After that, we initiated invagination in the TE. Single cell mechanisms at work are often activated in discriminatory ways both in space and time [25, 109, 141]. In our simulations, the distribution over the entire sheet of the length d by which the apical radius of cells R was shrunk depended on the position of the cell in relation to the centre of the sheet via a step function: cells in the middle of the sheet were set to constrict completely ($d = R$), while cells on the boundary did not constrict ($d = 0$, Supplementary Fig. 5.7). The coordinated movement of cells induced by these positional laws caused the tissue to fold and invaginate the epiblast. Short after TE invagination begins, we initiated lumenogenesis in the epiblast (Fig. 5.3G). In order to highlight the requirement of the TE, following TE folding (Fig. 5.3C,G), we broke the contacts between the TE and the epiblast for the remaining time of the simulation, inhibiting any mechanical interactions between the two tissues, but maintaining both tissues' own mechanics (Fig. 5.3D,H). We noted that throughout the experiment, with the exception of lumenogenesis, epiblast cells did not initiate any behaviours, the epiblast as a whole simply reacted to the mechanics induced by either the presence or the absence of the TE.

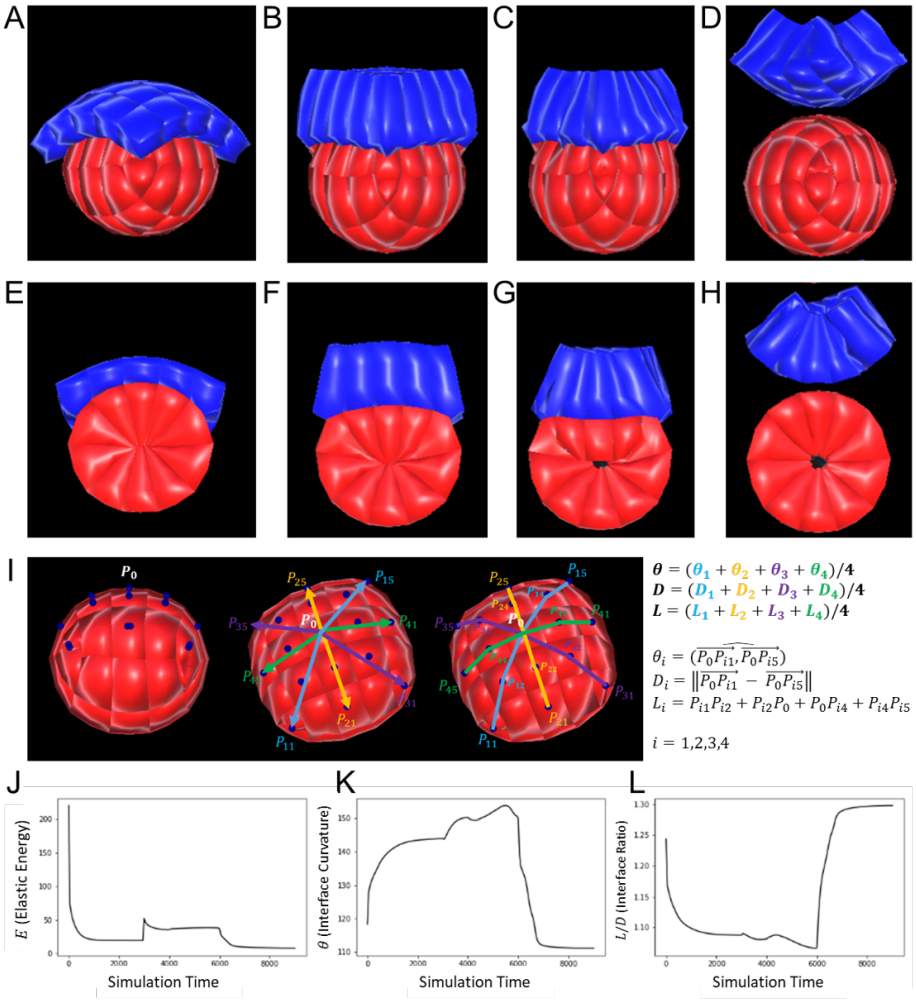

FIGURE 5.3: **Trophectoderm morphogenesis regulates epiblast shape. A-D.** 3D snapshots of the simulation of TE and EPI morphogenesis during mouse implantation, and the regulation of EPI shape, taken respectively at $t = 0, 3000, 6000$ and 9000. **E-H.** Corresponding 2D slices of the cell population at the same stages. **(A,E).** The initial stage features a single layered TE with cuboidal cells resting upon the rosette-shaped epiblast. **(B,F).** TE cells have transited to a columnar shape. **(C,G).** The TE has folded by apical constriction of single cells. Concomitantly, lumenogenesis was initiated in the epiblast (the process starts at $t = 4000$). **(D,H).** After adhesive links were broken between TE and EPI, the EPI bounces back to its near spherical shape. **I.** Definitions of the metrics used to evaluate the model, involving the curvature θ, TE/EPI interface diameter D, TE/EPI interface length L, and interface ratio L/D. **J.** Plot of the population's elastic energy E. Discontinuities mark the start of new morphological events at $t = 0, 3000, 4000$, and 6000). After removal of the TE, E falls closer to zero than ever before, meaning that cells are closer to their resting stage, hence less externally constrained. **K.** Plot of the interface curvature θ. During TE morphogenesis, θ rises towards a flat angle, then sharply drops when the TE is removed. **L.** Plot of the interface ratio L/D. During TE morphogenesis, the interface curvature decreases towards 1, then sharply increases when the TE is removed. Values of the equation parameters: $J_{\mathrm{EPI}} = J_{\mathrm{TE}} = 2.5, \lambda_{\mathrm{med}} = \lambda = 2, \rho = 1, R_{\mathrm{lum}} = 0.25$.

To appreciate the impact of the TE on the epiblast, we used the elastic energy E_i of a cell i as the sum over all cell springs of the squared difference between equilibrium and actual lengths. We extended this notion by defining the total elastic energy of a tissue or an entire population of cells as the sum of E_i's in the population (eq. 5.2).

$$E = \sum_{k \leq N} \left(\sum_{s \leq N_k} (r_{\text{eq}}^{ks} - r^{ks})^2 \right) \tag{5.2}$$

Here, N is the number of cells in the population and N_k the number of springs in cell k.

Cells always tended to minimise this energy, which can also be viewed as the degree of relaxation of cell: the closer it is to zero, the closer the cell is in its resting state, the more relaxed it is, hence the less constrained. In addition, we monitored the curvature of the epiblast, i.e. the inclination angle θ of the epiblast surface covered by the trophectoderm (Fig. 5.3I). An increasing curvature, trending towards a flat surface, was characteristic of the epiblast's transition from an oval rosette to a cup. Moreover, we measured the length (L) and diameter (D) of the interface between EPI and TE, and considered their interface ratio ($Ir = L/D$) as our third evaluation metric (Fig. 5.3I). It was expected that this ratio would decrease towards 1 as the epiblast flattened. We plotted the profiles of the curvature, the interface ratio and the elastic energy throughout our simulation.

Our model matched biological expectations by replicating, on the one hand, an increasing curvature and a decreasing interface ratio, with ultimately a flat TE/EPI interface just before we removed the TE (Fig. 5.3C,G,K,L). On the other hand, as soon as the TE was removed, the epiblast bounced back to its original shape (Fig. 5.3D,H,K,L). This result

agrees with the experimental observation that without the TE, the epiblast does not break symmetry [155]. The elastic energy profiles tie these behaviours to the mechanical influence of the TE over the epiblast. Actually, breaking mechanical interactions between the TE and the EPI not only resulted in a sharp drop in elastic energy, but this energy also plateaued at a value significantly lower than in other stages (Fig. 5.3J), demonstrating that cells were more mechanically constrained when both tissues were in contact.

These observations suggest that the presence of the TE imposes mechanical stress on epiblast cells, hinting to the necessity of this tissue's morphogenesis in the remodelling of the epiblast.

5.2.3 Trophectoderm morphogenesis fosters epiblast movement towards the uterine tissue

An important requirement of implantation is close contact between the embryo and the uterine tissue. As soon as the three pre-implantation lineages are specified, the blastocyst hatches out of the zona pellucida and initiates the process of implantation [8]. However, there exists a gap between the hatched blastocyst and attachment sites in the uterus. In order to close this gap, the embryo needs to move towards the uterus. It was recently established that this movement of the embryo towards maternal sites occur concomitantly to the drastic morphological changes observed in the TE [26]. Furthermore, it was observed in that same study that primitive endoderm expansion over the whole embryo is driven by TE morphogenesis. Given that the trophectoderm keeps close contact with the epiblast during these events,

we hypothesised that epiblast positioning could also be affected by TE morphogenesis. We employed computational modelling to examine whether TE morphological changes could influence the trajectory of the epiblast.

Here, as previously, we reproduced the sequence of TE morphogenesis (elongation followed by folding via apical constriction), and observed how it affected the position of the epiblast (which also undergoes lumenogenesis). To highlight how the TE influences the trajectory of the epiblast, we defined what we designated as the "pushing distance". We computed this distance at any given time point of the simulation by calculating the difference in height between the lowest point of the epiblast at that time point and the lowest point at the initial stage (Fig. 5.4A). We plotted the profiles of this metric and observed an increasing pushing distance as the TE transited from cuboidal to columnar, then as the TE folded (Fig. 5.4B). The sudden soar observed at $t = 4000$ reflects the slight elongation of the tissue due to hollowing-driven lumenogenesis in the epiblast.

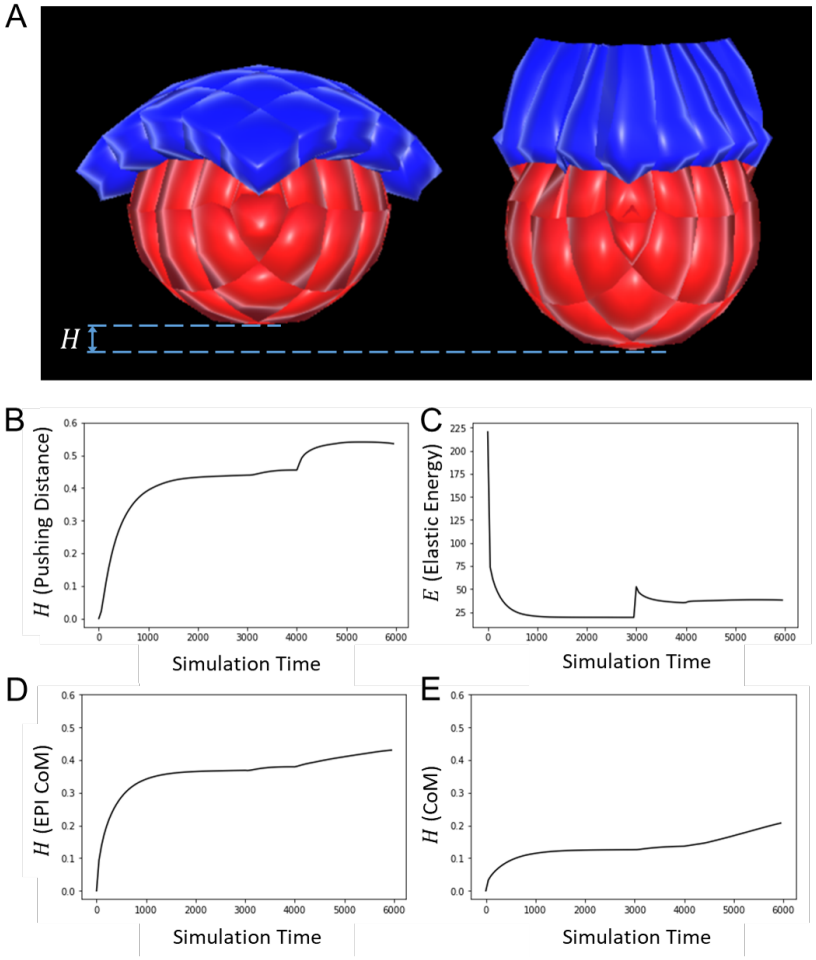

FIGURE 5.4: **Trophectoderm fosters epiblast movement towards maternal sites. A.** Snapshots of the simulation of TE and EPI morphogenesis during mouse implantation, and their influence on EPI positioning, taken respectively at $t = 0$ and 6000. **B.** Plot of the pushing distance, which increases with time. **C.** Plot of the elastic energy E. Discontinuities mark the start of new morphological events ($t = 0$ and 3000). The sudden soar observed at $t = 4000$ reflects the slight elongation of the tissue due to hollowing-driven lumenogenesis in the epiblast. **D.** Plot of the pushing distance on the epiblast Centre of Mass (CoM), which also increases with time. **E.** Plot of the pushing distance on the cell population Centre of Mass (CoM), which also increases with time. Values of the equation parameters: $J_{\mathrm{EPI}} = J_{\mathrm{TE}} = 2.5, \lambda_{\mathrm{med}} = \lambda_{\chi} = 2, \rho = 1,$,d=0.5, $R_{\mathrm{lum}} = 0.25$.

We chose to monitor the lower end of the epiblast because it is via this pole that the epiblast attaches to maternal sties. However, To ensure that

the observed changes did not merely represent an elongation of the epiblast, we also tracked the trajectory of the Centre of Mass (CoM) of both the epiblast (Fig. 5.4D) and the entire cell population (Fig. 5.4E). Similarly, these metrics reaffirmed that the epiblast indeed engages in a downwards movement. Furthermore, we checked that lumenogenesis in the epiblast was not necessary to foster this motion (Fig. 5.8). These results suggest that TE morphogenesis, while reshaping the epiblast, also fosters the embryo's movement towards maternal sites.

5.2.4 Sensitivity analysis

Physical properties are generally a segregating factor between differentiated cells in development [14, 120]. Although the mouse trophectoderm and epiblast form distinct cell lineages, we have so far assumed similar characteristics for both types of cells. The nature of our cell model allows for global physical properties such as mechanical stiffness to emerge from lower scale interactions between subcellular elements. In order to characterise cells by their stiffness and thus differentiate trophectoderm and epiblast cells, we first needed to establish how this property depended on intrinsic model parameters. In the following case study, we set out to determine how cell stiffness relates to parameter J, the scaling factor of the elastic force between neighbouring particles.

We used an "in Silico" adaptation of the experimental protocol described in [97] to estimate cell stiffness based on the computation of a measure of their elasticity modulus (also known as *Young* modulus). For a given value of J, we perform a series of simulations consisting of applying forces of increasing magnitudes (F) on the apical and basal faces of an epithelial cell (Fig. 5.5A). For each force, we calculate the associated stress ($\sigma = \frac{F}{S}$,

where S is the surface area of each face) and note the resulting deformation (strain, $\epsilon = \frac{\Delta L}{L_0}$). We then plotted the stress-strain curve and estimated the Young modulus (Y) as the slope of the curve using a linear regression model (fig. 5.5B). Using this protocol, we ran simulations with 50 different values of J uniformly distributed between 0 and 5, recording estimated values of Y after every simulation. The plot in (fig. 5.5C) suggests that Y relates to J in a measurable way. More broadly, Y increases with J. In other words, the interaction strength between subcellular particles regulates cells global stiffness: the stronger this interaction is, the stiffer the cell.

We conducted the same analysis on how friction forces coefficients λ_χ and λ_{med} affect cell mechanical properties. We fixed λ_{med} ($\lambda_{\text{med}} = 2$), varied λ_χ, and observed the evolution of cells elasticity modulus as a function of $\frac{\lambda_\chi}{\lambda_{\text{med}}}$. Simulated show that above a certain threshold ($\frac{\lambda_\chi}{\lambda_{\text{med}}} \geq 0.161$), cells elasticity modulus was constant (fig. 5.9A,B). Below this threshold, the structure of the cell was compromised (fig. 5.9C). Overall, these observations suggested that cell mechanical properties did not depend on differences between friction parameters within and without the cell. Furthermore, we refined the cell mesh, taking the number of vertices to 42 (fig. 5.9D), and repeated the experiments, varying values of parameter J (fig. 5.9E,F). Results show that mechanical properties changed with mesh refinement (For $J_{42} = 2.5 \rightarrow Y_{42} = 2.75$). However, while refining the mesh, parameters can be tuned in order maintain cell stiffness ($J_{42} = 2.6 \rightarrow Y_{42} = 2.90$) to allow similar responses to external stress.

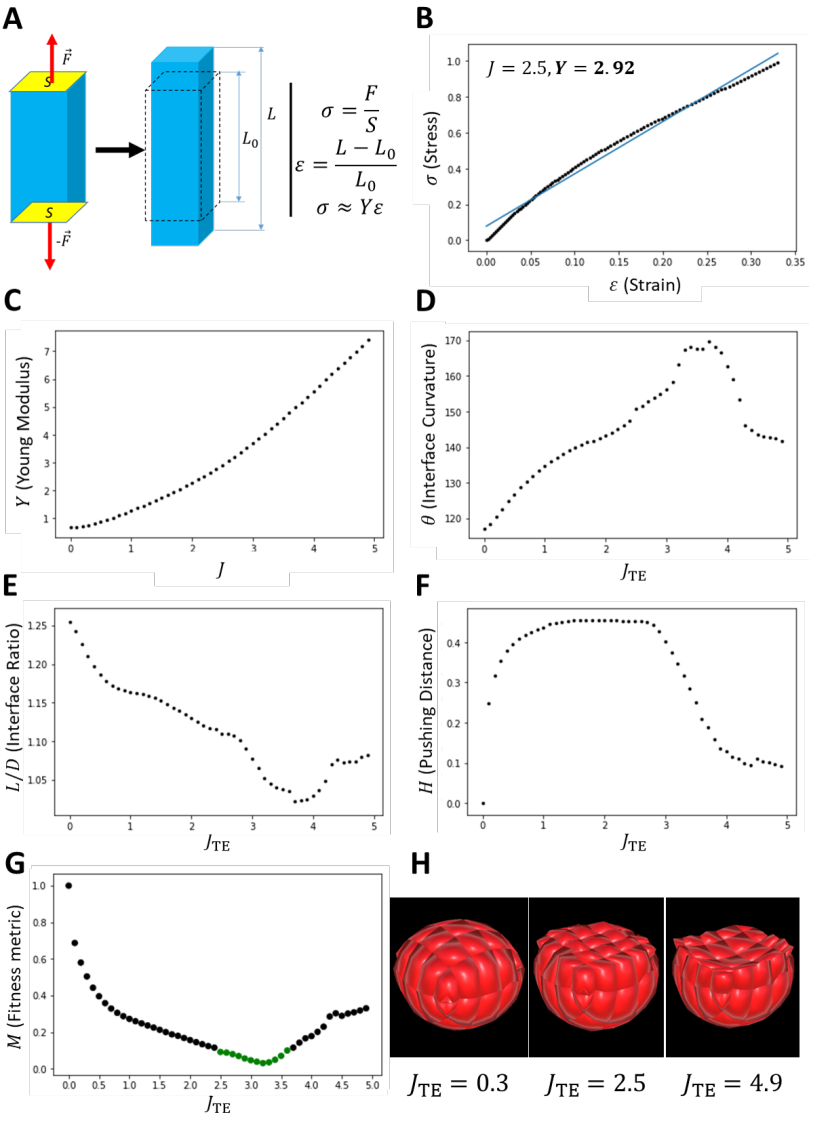

FIGURE 5.5: **Mechanical properties of EPI and TE determine mouse implantation. A.** In"Silico" experimental protocol used to determine cells elastic modulus. **B.** Stress-Strain curve (*black*) for a single epithelial cell (34 vertices) with $J = 2.5$. (*blue*) Linear approximation of the Stress-Strain curve. The elastic modulus of the cell is determined by the slope of this line ($Y = 2.92$). **C.** Plot of the Elastic (Young) modulus of cells as a function of parameter J, the interaction strength between subcellular particles. **D,E,F.** Respective Plots of the Interface curvature, the Interface ratio and the Pushing Distance as functions of the mechanical stiffness of TE cells (determined by J_{TE} as in **C**). **G.** Plot of the fitness metric as functions of the mechanical stiffness of TE cells (determined by J_{TE} as in **C**). **H.** Snapshots of the epiblast shape at the end of simulations for different values of J_{TE}. With equal stiffness (middle, $J_{TE} = 2.5$, $J_{EPI} = 2.5$), trophectoderm morphogenesis flatten the epiblast, which acquires a cup shape. However, with significantly lower stiffness (left, $J_{TE} = 0.3$, $J_{EPI} = 2.5$), trophectoderm morphogenesis barely reshape the epiblast; meanwhile, with considerably higher stiffness (right, $J_{TE} = 4.9$, $J_{EPI} = 2.5$), the trophectoderm invaginates the epiblast, forcing a concave interface with the epiblast. Other parameter values, $\lambda_{med} = \lambda_\chi = 2, \rho = 1$, $d = 0.5$.

Having established how model parameters regulate cell stiffness, we were able to discriminate between cell types based on parameter values we set for each. We then sought to investigate how differences between physical properties of trophectoderm and epiblast cells would influence mouse implantation. For this, we conducted a parameter space exploration in the one dimensional space of values of parameter J_{TE}, maintaining the value of J_{EPI} constant to a value of 2.5. This series of experiments consisted of running 50 different simulations of mouse implantation, with values of J_{TE} ranging from 0 to 5 with a step of 0.1. To better appreciate the impact of the trophectoderm on the epiblast, we do not trigger lumenogenesis in the epiblast. For every simulation, we recorded the curvature, interface ratio and pushing distance as defined in previous section, and plotted their values against values of J_{TE} (fig. 5.5D, E, F). In order to determine which values of J_{TE} perform best overall for these metrics, we defined a normalised fitness measure consisting of a combination of these metrics as previously done in [35]. If we denote by $\theta(J_{\mathrm{TE}})$, $Ir(J_{\mathrm{TE}})$ and $H(J_{\mathrm{TE}})$ the respective values of the curvature, interface ratio and pushing distance for a given value of J_{TE}, and $\theta_{\mathrm{min,max}}$, $Ir_{\mathrm{min,max}}$ $H_{\mathrm{min,max}}$ their optimal values in the simulated data, the fitness metric (M) is defined by equation (5.3).

$$M(J_{\mathrm{TE}}) = \frac{1}{3}\left(\left(\frac{\theta(J_{\mathrm{TE}}) - \theta_{\mathrm{max}}}{\theta_{\mathrm{max}} - \theta_{\mathrm{min}}}\right)^2 + \left(\frac{Ir(J_{\mathrm{TE}}) - Ir_{\mathrm{min}}}{Ir_{\mathrm{max}} - Ir_{\mathrm{min}}}\right)^2 + \left(\frac{H(J_{\mathrm{TE}}) - H_{\mathrm{max}}}{H_{\mathrm{max}} - H_{\mathrm{min}}}\right)^2\right) \tag{5.3}$$

It can be observed that function M admits a minimum and its values are constrained in $[0, 1]$. We plotted this metric against values of J_{TE} and considered that areas where the fitness fell below 0.1 represented simulations featuring a good compromise between curvature, interface ratio and pushing

distance (fig. 5.5G, *green points*). The plotted data hint the existence of a preferential range of values that yield optimal fitness with respect to the three metrics involved (fig. 5.5G *green points*, fig. 5.5H *middle*). Within this range, the strength of subcellular interactions is always always higher for trophectoderm cells ($J_{\mathrm{TE}} \in [2.5, 3.5]$) than for epiblast cells ($J_{\mathrm{TE}} = 2.5$). Assuming that cell stiffness remain constant through implantation, this result suggest that mouse implantation requires trophectoderm cells to be generally stiffer than epiblast cells. However, outside of this range, simulations appear to perform poorly. For instance, below this range i.e. with TE cells more ductile than EPI cells, the epiblast is not sufficiently remodelled into a cup (fig. 5.5H, *left*), as attested by moderate performances of the interface curvature and ratio (fig. 5.5D,E)). Above this range i.e. simulations featuring TE cells significantly more rigid than EPI cells, the trophectoderm considerably invaginates the epiblast, creating a concave interface ((fig. 5.5H, *right*)). This reflects poorly on the pushing distance as highlighted by the negative slope of its curve (fig. 5.5F)).

5.3 Discussion and Conclusion

Understanding the processes by which the mammalian embryo implants in the maternal uterus is crucial to many breakthroughs in embryology [149]. New insights into these morphogenesis events could be of great importance in helping for example to reduce human infertility [56]. Although advances have been made by studying biochemical cues involved in these events, we focused here on the mechanical basis at the cellular level of epiblast morphogenesis. In order to study the physical dynamics of mouse implantation, we have designed a novel, computationally efficient model of biological cells and tissue

mechanics able to simulate key episodes of vertebrate morphogenesis. With this model, we were able to schematically reproduce lumenogenesis in the epiblast, trophectoderm morphogenesis driven by single cells elongation and apical constriction, as well as provide theoretical support to the fact that this morphogenesis regulates the remodelling and positioning of the epiblast during implantation.

A well-known shortcoming of agent-based modelling is the risk to introduce disputable artefacts in the simulations. Within the scope of this work, we have shown that our model adhered well to biology by successfully simulating tissue-level morphological changes based solely on changes triggered at the cellular level, in a bottom-up, emergent fashion. We did this in particular for epithelial bending through apical constriction [131], rosette formation via polarised apical constriction [65], and repulsion-driven lumenogenesis [8, 9]. Nonetheless, some nuance should be added to certain quantitative features of the simulations. For instance, although it is a biological fact that the epiblast lumen's volume increases as a result of cells drifting apart, the rate of this growth as exhibited in the graph of Fig. 5.2E may not reflect the actual rate curve in mouse embryos. The same could be said of the rate at which the epiblast reshapes (Fig. 5.3K,L), or the trophectoderm-induced epiblast velocity in its motion towards maternal sites (Fig. 5.4B). While not invalidating our main conclusions, these quantitative outputs are essentially contingent upon the choice of the potential function (here the Morse potential) and parameter values. This limitation could be overcome by experimenting with other potential functions, searching parameter space, and comparing results against real biological data.

Another weakness of computational modelling is its inability to integrate all possible details of a real-world problem, as this would inevitably

increase complexity and demand unavailable computing power. Clearly, efficiency in our simulations was achieved by stripping the model of noticeable features of biological development. One important approximation is that we ignored the hypothetical impact of proliferation, although it is a pervasive phenomenon in both tissues. However, while it may be argued that proliferation plays a non-trivial role in the elongation of trophectodermal cells [26], it is difficult to make a case that proliferation would be central in reshaping the epiblast, or the folding of the trophectoderm. In fact, this particular lack in our approach could even be considered an advantage, since neglecting proliferation also allowed isolating, hence highlighting the effects of pure mechanical interactions within and between the trophectoderm and the epiblast. Another simplification is that we neglected stochastic effects related for example to cell movements during these embryogenesis episodes. Although it was shown that cell membrane blebbing influenced cell differentiation [153], in many epithelial settings, stochastic effects are often compensated by strong interactions between cells [54]. Furthermore, in general, deterministic models, still exhibit good predictive power while remaining computationally practical [78].

In summary, although relatively abstract and schematic, our computational model and simulations offer new insights into mouse embryo implantation. Looking forward, refinements could combine the effects of mechanical interactions with proliferation and the stochasticity of biological processes to further investigate tissue shape changes. Then, the variables and parameters in these simulations could be tuned to fit quantitative metrics based on real measurements gathered from implanting embryos.

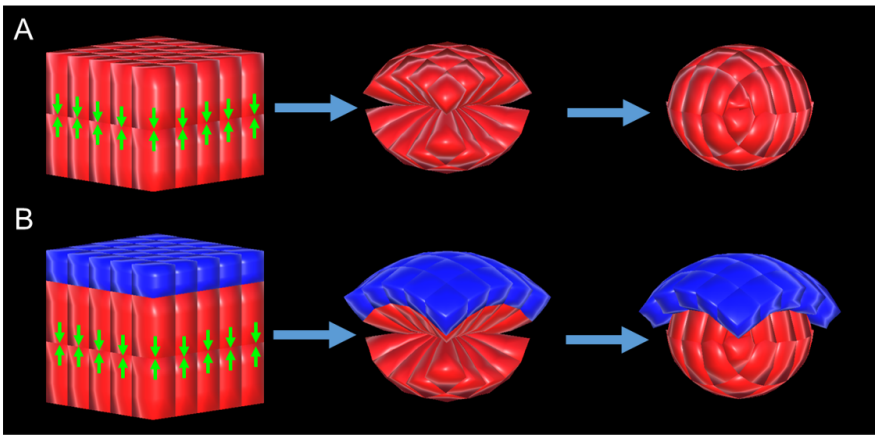

FIGURE 5.6: **Epiblast and trophectoderm population reconstruction. A.** The rosette-shaped EPI tissue is built by submitting polarised cells in a double epithelial layer to apical constriction. Green arrows indicate the apical surface of the cells, where constriction occurs. **B.** The initial cell population (TE and EPI) is built by adding an epithelial layer to the forming the EPI.

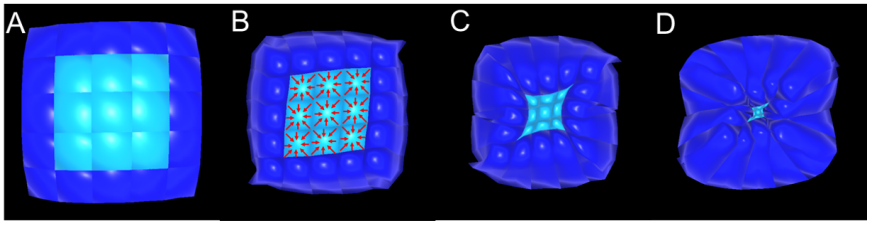

FIGURE 5.7: **Top view of trophectoderm morphogenesis. A.** Initial stage with cuboidal cells. **B.** Columnar TE initiating apical constriction. Red arrows highlight cells undergoing apical constriction. In this case, only cells in the middle constrict (light blue) to enable folding. **C.** Folded TE. **D.** Folded TE after separation from the EPI.

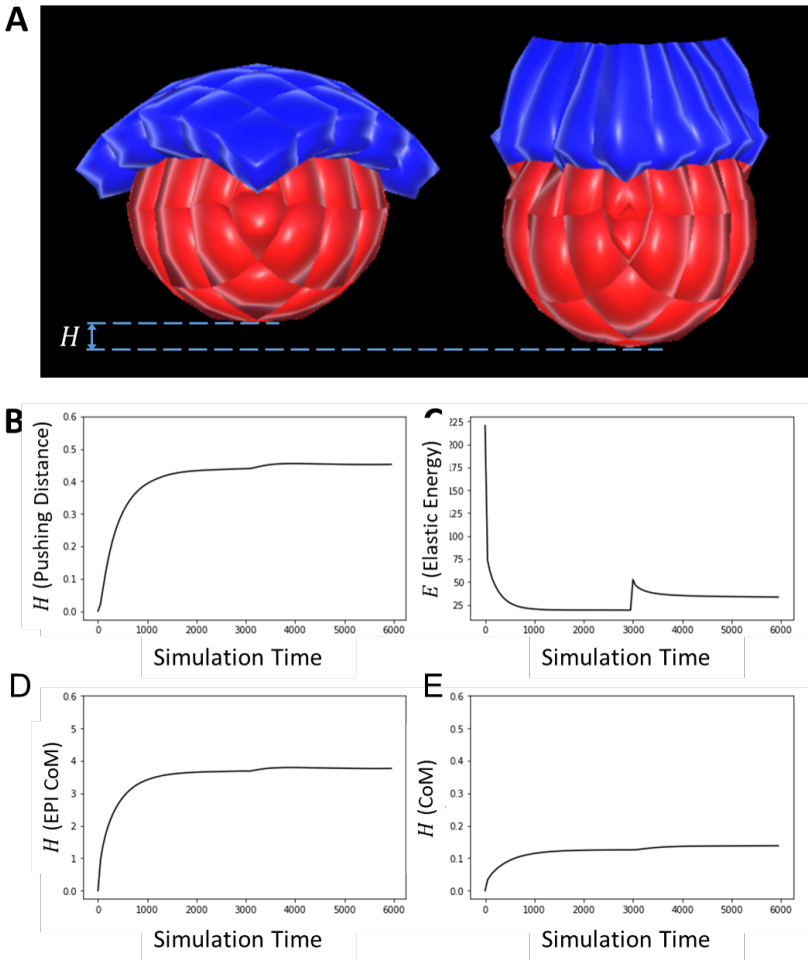

FIGURE 5.8: **Trophectoderm fosters epiblast movement towards maternal sites (Without lumenogenesis in epiblast). A.** Snapshots of the simulation of TE and EPI morphogenesis during mouse implantation, and their influence on EPI positioning, taken respectively at $t = 0$ and 6000. **B.** Plot of the pushing distance, which increases with time. **C.** Plot of the elastic energy E. Discontinuities mark the start of new morphological events ($t = 0$ and 3000). **D.** Plot of the pushing distance on the epiblast Centre of Mass (CoM), which also increases with time. **E.** Plot of the pushing distance on the cell population Centre of Mass (CoM), which also increases with time. Values of the equation parameters: $J_{\mathrm{EPI}} = J_{\mathrm{TE}} = 2.5, \lambda_0 = \lambda_\chi = 2, \rho = 1$.

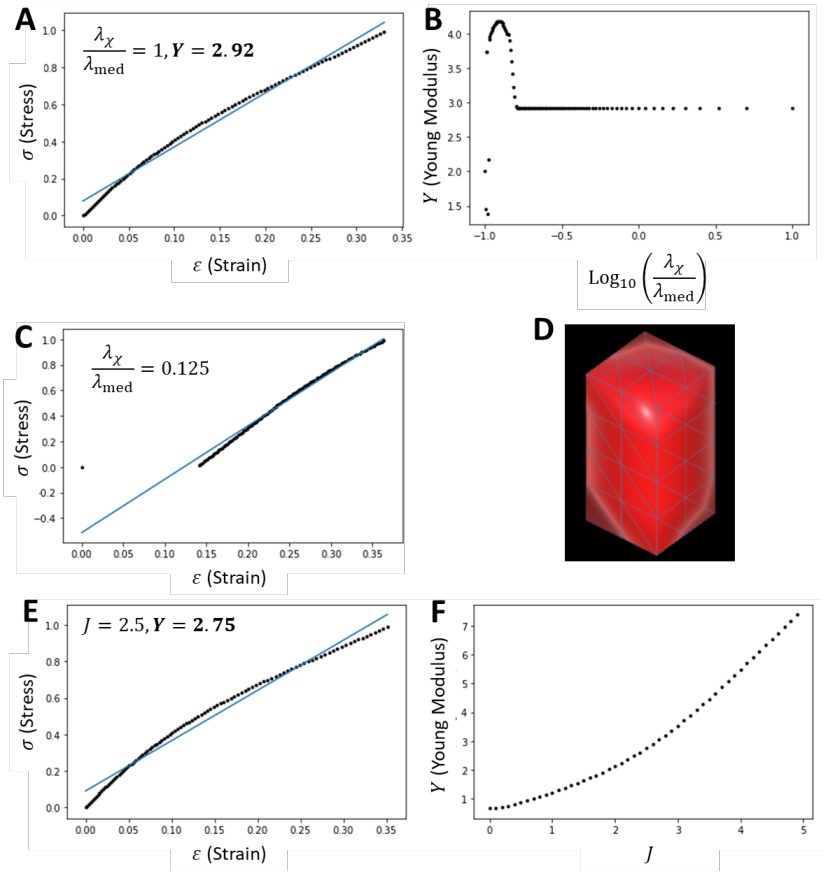

FIGURE 5.9: **Sensitivity analysis (Supplementary). A.** Stress-Strain curve (*black*) for a single epithelial cell (34 vertices) with $J = 2.5$ and $\lambda_{\text{med}} = \lambda_\chi = 2$. (*blue*) Linear approximation of the Stress-Strain curve. The elastic modulus of the cell is determined by the slope of this line ($Y = 2.92$). **B.** Plot of the Elastic (Young) modulus of cells as a function of the parameter ratio ($\frac{\lambda_\chi}{\lambda_{\text{med}}}$). Young's modulus is defined and constant for values of $\frac{\lambda_\chi}{\lambda_{\text{med}}}$ greater or equal to approximately 0.161. Below this value, simulated cells do not behave as physical materials, and the elasticity modulus cannot be defined as illustrated in the next plot. **C.** Stress-Strain curve (*black*) for a single epithelial cell (34 vertices) with $J = 2.5$, $\lambda_{\text{med}} = 2$ and $\lambda_\chi = 0.25$. The discontinuity in the curve shows that the set of parameters is not suitable for a cell. **D.** 3D rendering of an epithelial cell with square basis and 42 vertices. **E.** Stress-Strain curve (*black*) for a single epithelial cell (42 vertices) with $J = 2.5$ and $\lambda_{\text{med}} = \lambda_\chi = 2$. (*blue*) Linear approximation of the Stress-Strain curve. The elastic modulus of the cell is determined by the slope of this line ($Y = 2.75$). **F.** Plot of the Elastic (Young) modulus of a cell (42 vertices) as a function of the parameter J, the interaction strength between subcellular particles. In order for such a cell (42 vertices) to have equivalent stiffness with the previous type of cell (34 vertices, $J_{34} = 2.5$, $Y_{34} = 2.92$), the parameter J_{42} needs to be set to approximately 2.6 ($Y_{42} = 2.90$).

Chapter 6

Quantification of cell behaviors and computational modelling show that cell directional behaviors drive zebrafish pectoral fin morphogenesis

Understanding the mechanisms by which the zebrafish pectoral fin develops is expected to produce insights on how vertebrate limbs grow from a 2D cell layer to a 3D structure. Two mechanisms have been proposed to drive limb morphogenesis in tetrapods: a growth-based morphogenesis with a higher proliferation rate at the distal tip of the limb bud than at the proximal side, and directed cell behaviors that include elongation, division and migration in a nonrandom manner. Based on quantitative experimental biological data at the level of individual cells in the whole developing organ, we test the

conditions for the dynamics of pectoral fin early morphogenesis. We found that during the development of the zebrafish pectoral fin, cells have a preferential elongation axis that gradually aligns along the proximodistal axis (PD) of the organ. Based on these quantitative observations, we build a center-based cell model enhanced with a polarity term and cell proliferation to simulate fin growth. Our simulations resulted in 3D fins similar in shape to the observed ones, suggesting that the existence of a preferential axis of cell polarization is essential to drive fin morphogenesis in zebrafish, as observed in the development of limbs in the mouse, but distal tip-based expansion is not.

6.1 Introduction

Vertebrate limb development is a classical model system for understanding pattern formation: the process in which spatial organization of differentiated cells and tissues is generated in the embryo. Various tissue types contributing to the mature limb are derived from several embryonic tissues including the lateral plate mesoderm, the somites and the ectoderm [16, 21, 23, 62, 73]. How the pectoral fin lateral plate mesoderm (LPM), which gives rise to skeletal elements and tendons, grows outward from the body trunk and acquires its particular shape remains unclear. The *in vivo* observation of the whole process and the quantification of cell behaviors underlying morphogenesis are still open challenges. The formation of the zebrafish pectoral fin is a model for limb development, as it is especially suited for long-term imaging owing to its external embryonic development and translucent body. The formation of the pectoral fin initiates at 18 hours post fertilization (hpf), when LPM cells condense at the prospective fin location as a flat 2D cell layer under a

single layer of ectodermal cells. Over the course of the next 30 hours, the fin bud grows and forms a 3D structure. LPM cells proliferate and myoblasts coming from neighbouring somites enter the fin, where they will give rise to muscle bundles. At the distal tip of the fin, ectodermal cells align to form the so-called apical ectodermal ridge (AER) known to act as a source of molecular signaling required for the fin growth.

Over the past 40 years, the *"proliferation gradient"* model has been the dominant hypothesis to explain the limb bud elongation. This model suggests that a diffusible signal from the AER sets up a spatial concentration gradient. This molecule "signals the mesenchyme immediately underlying it, termed the 'progress' or 'proliferative' zone, to proliferate, resulting in directed proximodistal outgrowth" [105]. The AER indeed was shown to have mitogenic properties [126]. On the other hand, a few studies hypothesized that directionally oriented cell behaviors drive limb elongation. Li et al. [86] demonstrated that some mesenchymal cells in the chick wing bud are capable of migrating toward an ectopic source of Fgf4 (one of the molecules produced by the AER) implanted in the center of the bud. This work directly supported the idea that mesenchymal cells could consider the Fgf gradient as a chemoattractant rather than as a mitogen.

A number of computer simulations of limb bud elongation have been produced over the last decade, most of which are in two dimensions and based on the proliferation gradient hypothesis but do not incorporate real quantitative data into their model [38, 100, 121]. Recently, Boehm et al. [13] proposed a new three-dimensional computer model based on the actual shape of the mouse limb bud captured by optical projection tomography imaging. They found that the proliferation gradient would have to be extreme from the distal end to the proximal end and subsequently too unrealistic to account

for the bud shape. Similarly, Gros et al. [63] concluded that uniform cell division distribution and focal regions of cell death in the chick limb bud are unlikely to be sufficient to drive the anisotropic nature of its growth. Both studies observed that cell shapes were oriented toward the nearest ectoderm, rather than distally toward the apical ectodermal ridge. They have also demonstrated the presence of filopodia suggesting active cell movement.

With improvements in *in vivo* imaging setups and data processing, a recently available complete 3D tracking of the different cell types in the early fin bud reveals their heterogeneous and complex cellular rearrangement during the transition from 2D to 3D. The quantitative analysis of cell behaviors during the first 20 hours of the zebrafish pectoral fin formation are used to build a model of fin growth. The comparison between simulated and biological data highlights the pattern of cellular rearrangement underlying the pectoral fin morphogenesis.

6.2 Methods

6.2.1 Data acquisition workflow

For this study, 4D imaging data of developing zebrafish pectoral fins were acquired and pre-processed by our partners at the CNRS/Bioemergences lab [1]. Here we give a brief overview of the data acquisition workflow.

[1] http://bioemergences.iscpif.fr/bioemergences/index.php

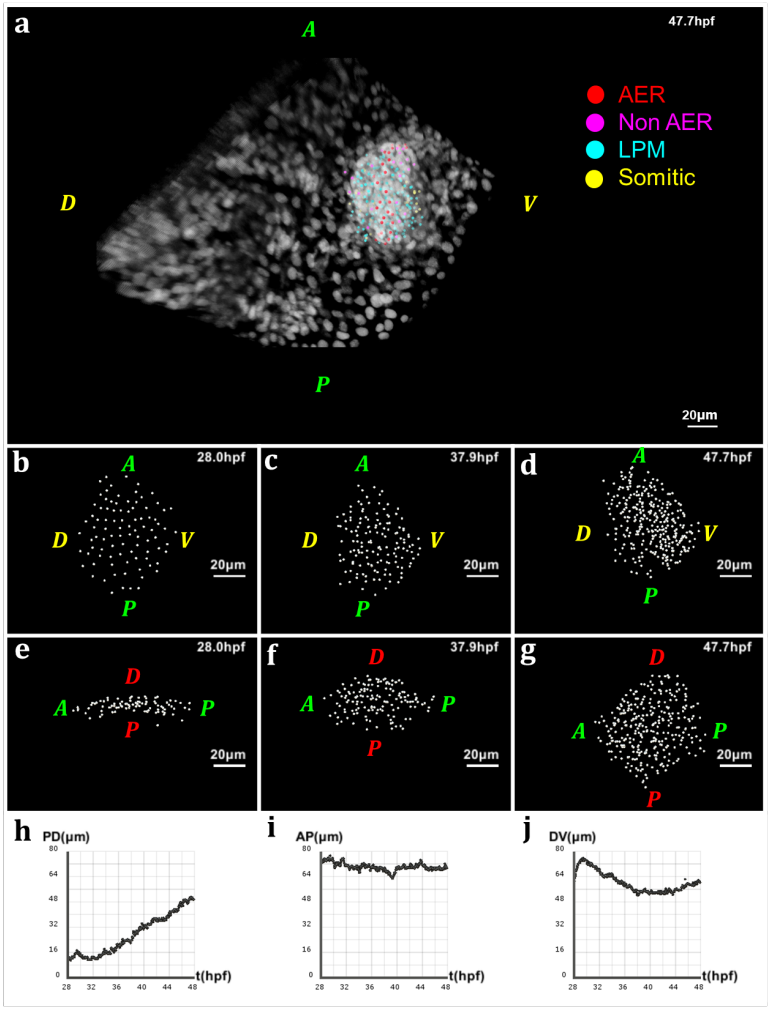

FIGURE 6.1: **Geometry of the pectoral fin based on live imaging and image processing data**. (a) 3D rendering of raw data nuclear staining at $t = 47.7$ hpf: dorsal view of the zebrafish body with detection of approximate nuclear centers of the pectoral fin cells highlighted by colored dots, where the color code depends on the cell type; scale bar: 20 μm. Imaging data and individual cell tracking have been generated by the CNRS/Bioemerges lab. (b-d) After applying cell detection methods: 3D rendering of the approximate nucleus centers of LPM cells in the pectoral fin at different stages of development, respectively $t = 28$ hpf, $t = 37.9$ hpf and $t = 47.7$ hpf (AP: anteroposterior axis; DV: dorsoventral axis). (e-g) 3D rendering of the pectoral fin at the same times along the AP axis and PD (proximodistal) axis. (h-j) Evolution over time of the fin size in μm along the PD, AP and DV axes respectively. Fin expansion occurs mainly along PD. It undergoes a slight compaction along the other two axes, more pronounced along the DV axis.

6.2.1.1 Zebrafish husbandry

Adult zebrafish (*Danio rerio*) were maintained at 28°C according to standard procedures as described in [80]. Embryos were kept at 0.3% Danieau's medium at 28.5°C. The transgenic line *Tg(X1a.Eef11:H2B-mCherry)* was used to visualize nuclei [124].

6.2.1.2 Imaging pectoral fin growth

Fin growth was monitored using the protocol described in [103]. Briefly, this was achieved on the upright Zeiss LSM780 confocal microscope equipped with 20x water dipping lens objective (Zeiss Objective W "Plan-Apochromat" 20x/1.0 DIC). The embryos were kept at 28.5°C and the chorion was removed using forceps prior imaging. Embryos were anaesthetized with 0.04% of tricaine methanesulfonate (Sigma) in embryo medium and mounted using agarose molds. The mounting strategy immobilized the embryo while allowing pectoral fin to develop unperturbed. The imaging plane was parallel to the plane formed by the anteroposterior (AP) and dorsoventral (DV) axes (Fig. 6.1a). Images of the developmental process were taken at a time invertal of 2 minutes and 18 seconds.

6.2.1.3 Image processing and reconstruction

The first analysis steps were performed using Fiji, an open source Java-based image processing (*ImageJ*) package. Raw datasets needed to undergo registration to keep the region of interest at about the same XYZ location, despite the embryos undergoing significant morphological changes during overnight imaging. To compensate for possible photo-bleaching, bleach correction by

histogram matching was also performed. Finally, images were uploaded into the Bioemergences workflow [48], an online software platform integrating original mathematical methods and algorithms to perform image filtering, nucleus center detection, and cell tracking (Fig. 6.1b-g). The outcome of cell detection was then manually validated using *Mov-IT*, an interactive visualization and editing tool complementing Bioemergences.

6.2.2 Tracking zebrafish pectoral fin growth along PD, AP and DV axes

The quantitative analysis required for this work necessitated that we track the fin's dynamics along its main axes: proximal-distal (PD), anterior-posterior (AP), dorsal-ventral (DV). Precise tracking of the fin's size along these axes is a challenge due to the fact that the embryo body moves during imaging, most likely due to growth. Embryo movements mean that its main axes do not always maintain a static orientation. This in turn poses the problem of precise identification of the fin's main axis for every time point. To tackle this issue, at each time point, we computed new orientations for the PD, AP, DV axes as functions of both the cloud of points (cell centers) at the current time and their orientations at the previous time step. First, we applied the Principal Component Analysis (PCA) algorithm to the cell centers in order to determine the three main directions of the point cloud. Then, we compared each of PCA output axes with the PD axis at the previous time step and kept the most parallel one as our new PD axis. Given that PCA does not keep track of the orientation at previous time steps, the basis formed by the two remaining PCA axes could be significantly rotated compared to the previous AP-DV basis. To correct this issue, we projected onto the plane formed by these two vectors the AP and DV axes computed

at the previous time steps, and considered these projections to be our new AP and DV axes. When the movement of the fin as a whole between two time steps is not significant enough to change the orientation of the axes, we keep the orientations computed in the previous time step. Here, noticing that the fin as whole, although still growing, is relatively stable as from about 43.3hpf, we stopped computing new axes orientations as from about that time point.

6.2.3 Computational model

In order to test our data-derived hypothesis, we turned to computational modelling. Although MG# was a good candidate model to perform this study, other factors made it more appealing to look for different models. As reviewed in chapter 2, when it comes to spatially explicit simulations of biological development, several computational approaches stand out. Depending on the biological realism they include, the spatiotemporal scale they capture, or the nature of variables they manipulate, models exhibit different properties and suit different purposes. In this case, the interest of our study did not lie in lower scale cell changes, but rather in the tissue morphogenesis emerging from their collective dynamics. Moreover, our datasets featured cells represented solely be their centre. Hence, we found it suitable to set our choice on the family of centre-based models (CBM). In this way, not only did we gain in computational efficient in comparison to deformable cell models (MG#), but this choice also meant that we could simulate cells using the initial states provided from the dataset, and use same metrics to compare our results against the biological data.

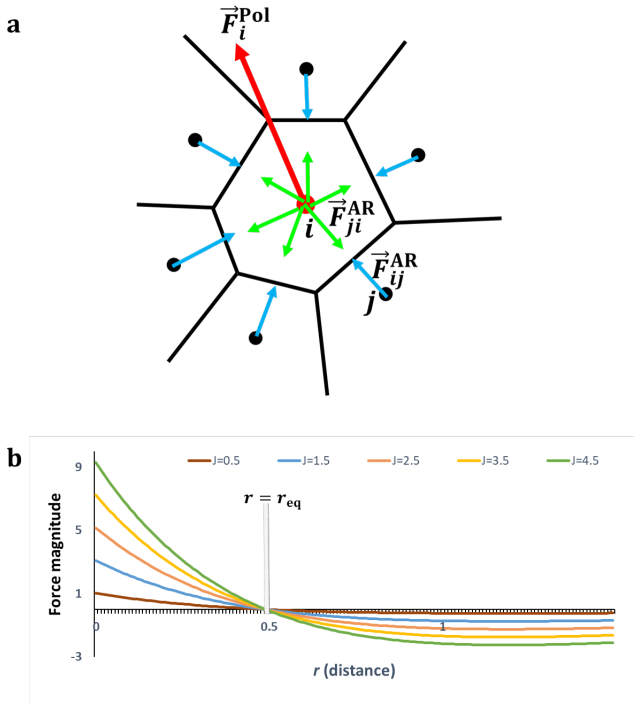

FIGURE 6.2: **Center-based computational model of multicellular dynamics**. (a) Schema of a local cell neighborhood and the abstract forces on cell centers. $\overrightarrow{F}_{ji}^{\mathrm{AR}}$ is the passive attraction-repulsion force exerted on a cell i by a cell j. $\overrightarrow{F}_i^{\mathrm{Pol}}$ is the active migration force driven by the cell's polarity (specified in Section 6.3.4). (b) Plot of the Morse force profile (derivative of the Morse potential) defining $\overrightarrow{F}^{\mathrm{AR}}$, for different parameter values. This curve presents two regimes: a positive regime (attraction) below an equilibrium distance r_{eq} and a negative regime (repulsion) above.

6.2.3.1 Model description

In CBM, cells are described by simple geometrical shapes whose representation can be reduced to their centers [146]. These models assume that cell trajectories in space can be assimilated to the motion of particles, which are governed by an equation of motion. CBMs have been used extensively to study the development of multiple organisms [35, 57, 146, 147]. We used a simplified mechanistic formulation of a CBM approach to simulate pectoral fin growth (Fig. 6.2a).

Cells are subjected in their center to forces governing their behavior. Similar to Julien Delile's *MecaGen* model [35], here we distinguished two main types of forces acting on a cell. On the one hand, passive attraction-repulsion (AR) forces $\overrightarrow{F}^{\mathrm{AR}}$ regulate interactions between cells and their local neighborhoods. AR forces translate the biophysical property that individual cells occupy a certain volume in space, hence their centres cannot be indefinitely close or indefinitely apart from each other. In the literature, these forces often derive from elastic potential mimicking linear or non-linear springs [7, 42]. Here, we followed this rule and derived AR forces from a *Morse potential*, a curve exhibiting a quadratic minimum framed by vertical and horizontal asymptotes (see its derivative in Fig. 6.2b). Moreover, we also defined a neighborhood for each cell by computing the 3D Delaunay tetrahedralization of the system. Two cells are deemed neighbors if their centers belong to the same tetrahedron.

On the other hand, cells also exhibit an active migration force which shapes their motion. Informed by empirical evidence, we constructed a polarity-driven migration force $\overrightarrow{F}^{\mathrm{Pol}}$ governing cells' intrinsic mechanics (explained in Results, Section 6.3.4). Finally, we neglected the effects of inertia due to a low Reynolds number [35, 106], and only considered viscosity-driven friction via a constant coefficient λ. Altogether, the equation of motion for a cell i with neighborhood $\mathcal{N}_i$ reads:

$$\lambda \overrightarrow{v}_i = \left(\sum_{j \in \mathcal{N}_i} \overrightarrow{F}^{\mathrm{AR}}_{ji} \right) + \overrightarrow{F}^{\mathrm{Pol}}_i \tag{6.1}$$

Here, $\overrightarrow{v}_i$ is the velocity of cell i.

In CBM, cell divisions are often simulated by adding daughter cells to the system at appropriate positions, notably in the neighborhood of the

mother cell. Here, we assumed that cells divide along their long axis and added new cells such that mother and daughter cells were aligned along this axis. Furthermore, we dealt with cell cycles by setting a global cycle period for all cells, and assigning random initial phases to individual cells. Using this model, we simulated zebrafish pectoral fin morphogenesis starting from the initial cell arrangement provided by the imaging data.

6.2.3.2 Computational implementation

The computational implementation of the described model requires a time discretisation of the equation of motion. Given $\overrightarrow{X}_i^t$, λ and $\overrightarrow{F}_i^t = \left(\overrightarrow{F}_i^{\mathrm{AR}}\right)^t + \left(\overrightarrow{F}_i^{\mathrm{Pol}}\right)^t$, respectively the position, friction coefficient and total force applied on the centre of cell i at time point t, an explicit Euler scheme is used to calculate the position $\overrightarrow{X}_i^{t+1}$ of the cell at the next time point. If dt is the time laps between instants t and $(t+1)$, cells update their configuration based on the following rule (Eq. 6.2).

$$\overrightarrow{X}_i^{t+1} = \overrightarrow{X}_i^t + \overrightarrow{V}_i^t \times dt \tag{6.2}$$

In Equation (6.2), $\overrightarrow{V}_i^t$ is nor given, neither determined. An expression of $\overrightarrow{V}_i^t$ can however be drawn from the equation of motion (Eq. 6.3).

$$\lambda \overrightarrow{V}_i^t = \overrightarrow{F}_i^t \tag{6.3}$$

Hence we update cell positions in simulations according to the following rule (Eq. 6.4).

$$\overrightarrow{X}_i^{t+1} = \overrightarrow{X}_i^t + \frac{\overrightarrow{F}_i^t}{\lambda} \times dt \tag{6.4}$$

This model has been implemented from scratch using the *C#* programming language, and the code source has been published on the code sharing platform Github[2].

6.3 Results

6.3.1 Zebrafish pectoral fin morphogenesis is proximal distal oriented

Using the approach described in the methods, we computed the pectoral fin's main axes for each time point. Then, we proceeded with calculating the size of the fin along each direction (Fig. 6.1h-j). Our data suggests that the fin expands principally along the PD axis with a quasi-linear slope, after an initial oscillatory behavior (Fig. 6.1h). This result aligns with previous observations which has consistently shown that a common property of limb development in vertebrates is the distal orientation of their growth [13, 72]. Furthermore, in this dataset, while fin's length along the AP axis oscillates somewhat, no significant overall change is recorded (Fig. 6.1i). Along the DV axis, however, the fin seems to contract slightly over the length of development (Fig. 6.1j), but seems to recover in the latest time steps.

6.3.2 Distal tip-based growth does not account for zebrafish pectoral fin morphogenesis

We sought to determine the role of proliferation in zebrafish pectoral fin growth. For this, we computed for every time point of development the

[2]https://github.com/guijoe/MaSoFin

bounding box encapsulating the pectoral fin. Then, we discretized this bounding box using the same volume unit everywhere. Next, we calculated the cumulative number of cell divisions in each volume unit of that space over the duration of fin growth. In order to understand the distribution of proliferation in 3D space, we proceeded with plotting the marginal distributions of cumulative divisions along the three main axes of the pectoral fin (Fig. 6.3d-e). To avoid the possibility of a frequency accumulation bias due to fact that the fin grows over time, we also analysed proliferation over a relative bounding box fitting the fin size at all time points. With this method, the last few layers of the PD axis always represented the actual distal end of the fin. We then also evaluated the cumulative number of division in each of these layers along the fin's axis (Fig. 6.3g-i).

Marginal distributions of proliferation along the AP and DV axes show that during pectoral fin morphogenesis, the bulk of proliferation is concentrated at the center of the fin, while only a few divisions are observed near the lateral surfaces (Fig. 6.3a-i, see supplementary figure S1 a,c). Differential behaviors of cells based on their location is a well-established biological mechanism, reminiscent of the so-called "French flag" model of Wolpert's positional information [**?**]. Furthermore, histogram plots of these marginal distributions may suggest that proliferation along the AP and DV axes can be assimilated to Gaussian processes (Fig. 6.3d-f, see supplementary figure S1 d-f). Although it could be expected that such behavior facilitates the development of the fin toward its known shape, it is not clear whether it is sufficient to drive this growth. However, it is also likely that the accumulation of cell division in the inner volume of the fin (Fig. 6.3g-i, see supplementary figure S1 g-i) is merely a consequence of the fin's geometry, namely its overall conic shape, favoring higher number of cells in the middle than near the lateral surfaces. This interpretation seems to be favoured by the data in

Fig. 6.3j,l (also see supplementary figure S1 j,l), which present quasi-uniform histograms of number of divisions per time step over the length of AP and DV axes.

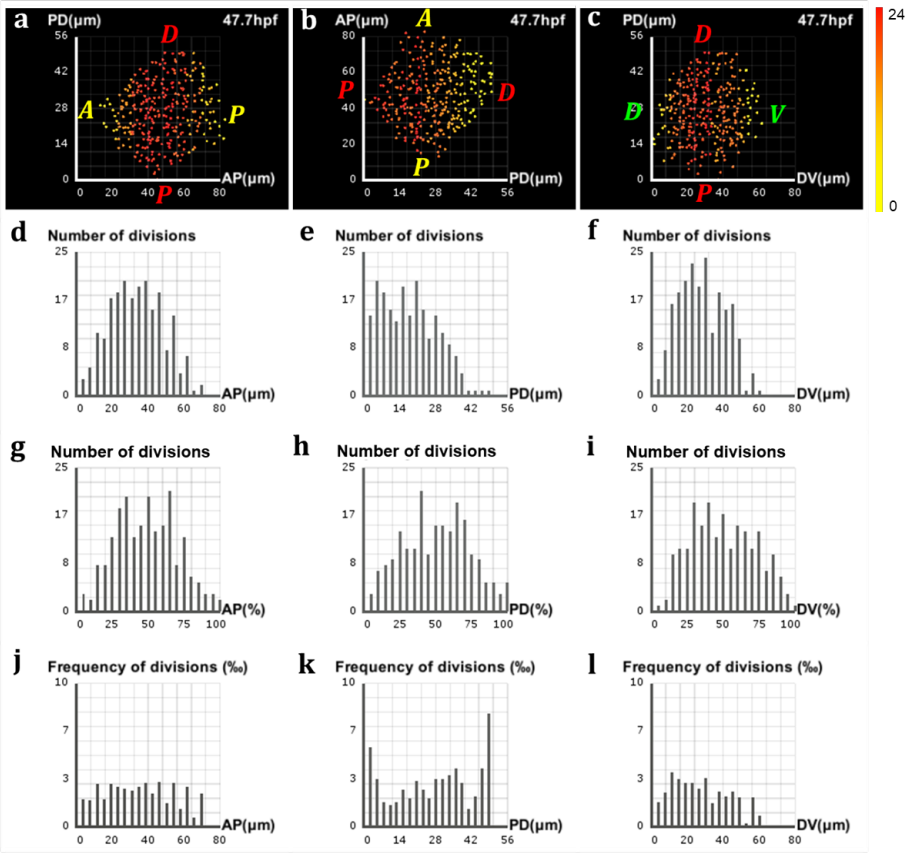

FIGURE 6.3: Analysis of proliferation in the zebrafish pectoral fin. (a-c) Frequencies of divisions along the AP, PD and DV axes respectively, highlighted by a yellow-red color gradient coding for differences in proliferation rates across the fin. (a,c) The preponderance of red at the center of the fin shows where the bulk of cell divisions takes place, with only a few of them occurring near the lateral surfaces (yellow). (b) A decreasing gradient of proliferation rates from the proximal pole to the distal tip characterizes the PD axis. (d-f) Marginal distributions of proliferation along the AP, PD and DV axes respectively, expressed in numbers of cells with respect to the absolute distance in μ m along the axis. (g-i) Same distributions with respect to the relative distance on the axis. (j-l) Same distributions expressed in proportions of cells with respect to the absolute distance.

Along the PD axis, the marginal distribution of proliferation shows a decreasing gradient of cell division from the proximal pole to the distal tip of the fin (Fig. 6.3b, see supplementary figure S1 b). This simply translates into the fact that proximal layers of the fin, which form early, host more divisions than distal regions, which develop later. This observation stands in contradiction with the growth-based morphogenesis hypothesis that stipulates higher proliferation rates at the distal tip of the fin. Hence, this result suggests that growth-based morphogenesis might not be the main drive for zebrafish fin pectoral morphogenesis.

6.3.3 Zebrafish pectoral fin cells exhibit preferential directional behaviors

Next, we looked whether cells exhibited peculiar behaviors along preferential directions that could influence the shaping of the zebrafish fin. To this goal, we decided to analyse the dynamics over time of the elongation axis of each cell. We determined the elongation axis of a cell i by computing the direction of maximum variance of the cloud of points consisting of cell i and its Delaunay neighborhood $\mathcal{N}_i$. This direction was given by the eigenvector corresponding to the maximum eigenvalue of the covariance matrix of $\mathcal{N}_i$. We denote this vector by $\overrightarrow{e}_i^{\text{Max}}$, which we also consider to be the polarity vector of the cell (Fig. 6.4a).

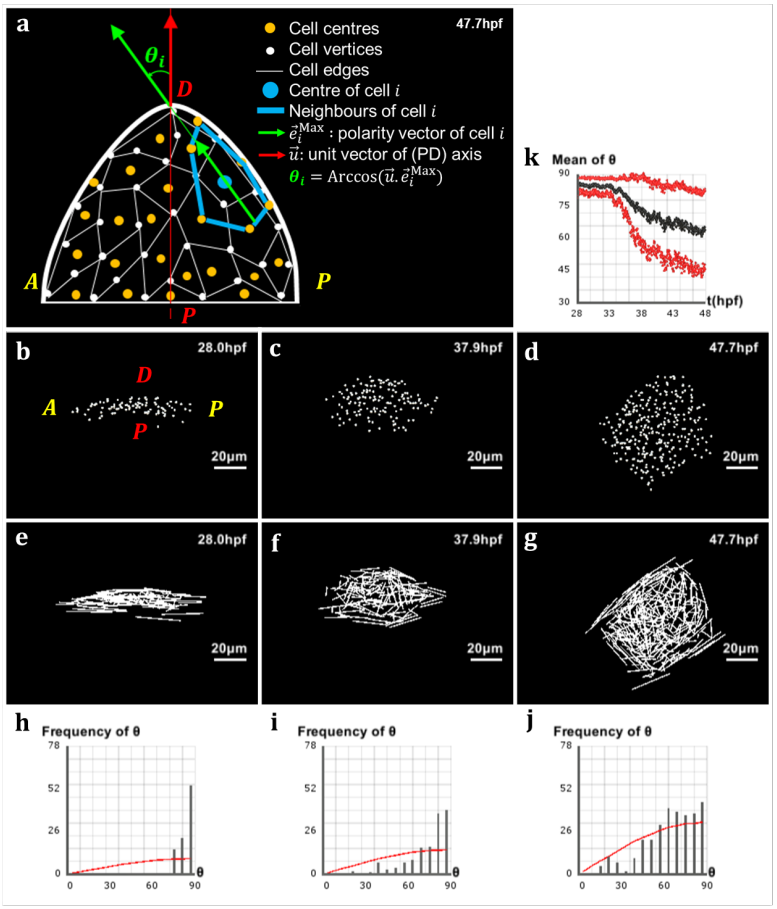

FIGURE 6.4: **Analysis of directional cell behaviors in the zebrafish pectoral fin**. (a) Schematics in 2D of the method used to analyse directional cell behaviors: for each cell i, θ_i denotes the polarity angle that this cell forms between its elongation axis $\overrightarrow{e}_i^{\text{Max}}$ (extracted from the maximum eigenvalue of the covariance matrix of its neighborhood $\mathcal{N}_i$) and the PD axis $\overrightarrow{u}$. (b-d) Lateral view of the pectoral fin at different stages of development, respectively $t = 28$ hpf, $t = 37.9$ hpf and $t = 47.7$ hpf. (e-g) Vector field of the cells' elongation axes $\overrightarrow{e}_i^{\text{Max}}$ in the pectoral fin at the same stages. (h-j) Distribution of the polarity angles θ_i of the cells in the pectoral fin at the same stages, compared with the standard distribution of random angles formed by two arbitrary vectors in 3D (red curve). (k) Evolution over time of the average polarity angle $\overline{\theta}$ of the fin cells $\pm$ its standard deviation $\Delta\theta$ shown in red.

Having computed the elongation axis of each cell through every time point of development, we observed that cells at initial stages are elongated

perpendicularly to the PD axis. We further noticed that, during development, cells gradually bring their long axis in closer alignment to the PD axis (Fig. 6.4e-g). This result is consistent with previous studies reporting high polarisation during limb development [72].In order to confirm this qualitative observation, we measured the angle that cells form via their long axis with the PD axis of the pectoral fin, and called it the "polarity angle" with notation θ_i (Fig. 6.4a). At the initial time point, the distribution of polarity angles was clustered around 90°, confirming the previous observation that cells were elongated perpendicular to the PD axis (Fig. 6.4h). During development, this distribution spread in a nonrandom way between 0 and 90°, where the average polarity angle decreased toward a value of 60°, meaning that cells exhibited preferential directionality by orienting their long axis toward the PD axis (Fig. 6.4i,j). To ensure that our observations were not mere features of a single developing fin, we applied the same analysis to a different dataset which lead to a similar dynamics (see supplementary figure S2).

6.3.4 Directional cell behaviors are essential to drive zebrafish pectoral fin morphogenesis

We wanted to find out whether directional behaviors of cells were sufficient to drive fin morphogenesis. In the previous analysis, we observed that cells tended to align their long axis in the direction of the PD axis, eventually forming an average polarity angle $\overline{\theta} = 60°$. We noticed that such behavior could explain the overall conic shape of the fin. Based on this observation, we designed the *polarity force* term $\overrightarrow{F}^{\mathrm{Pol}}$ of the 3D model as follows. First, we defined a global *polarity energy* of the cell population, denoted by H^{Pol}. Models in which forces derive from problem-specific global energy have been

used in different contexts such as cell sorting, molecular signaling, or epithelial morphogenesis in the developing *Drosophila* [52, 116]. Germann et al. [57] also use an energy term conjointly with CBM by defining a tissue polarity potential and an apicobasal polarity to distinguish between epithelial and mesenchymal tissues.

Here H^{Pol} is expressed over all N cells by:

$$H^{\mathrm{Pol}} = \left(\frac{1}{N} \sum_{1 \leq i \leq N} \arccos\left(\overrightarrow{u} \cdot \overrightarrow{e}_i^{\mathrm{Max}} \right) - \frac{\pi}{3} \right)^2 \tag{6.5}$$

Here, $\overrightarrow{u}$ denotes the unit vector of the PD axis, which constitutes the direction of fin growth. It has been suggested that this axis is defined by the body plan at the onset of fin growth (AP, DV axis). Moreover, cells can sense this axis through molecular cues originating from determined mesoderm cells, involving for instance gradients of Wnt or FGF [144].

Although H^{Pol} is defined globally, individual cells contribute to this potential only to the extent of their local neighborhood. This energy was designed such that its minimum corresponds to $\overline{\theta} = 60°$. Then, we set the polarity force to be proportional to the opposite of the gradient of H^{Pol} with respect to each cell:

$$\overrightarrow{F}_i^{\mathrm{Pol}} = -\nu \overrightarrow{\nabla}_i H^{\mathrm{Pol}} \tag{6.6}$$

Having defined these laws governing cell interactions, we proceeded to simulating limb morphogenesis. In order to highlight the influence of the polarity force, we used a uniform cell cycle period with a random initial phase for each cell. Our virtual limb featured similar properties to the imaged limb (Fig. 6.5). Driven by the polarity force $\overrightarrow{F}^{\mathrm{Pol}}$ and constrained by the elastic force $\overrightarrow{F}^{\mathrm{AR}}$ defined in Section 6.2.3, cells moved and reshaped their

neighborhoods to minimize the polarity energy H^{Pol}, resulting in $\overline{\theta}$ effectively decreasing throughout development toward 60° (Fig. 6.5n), in a way similar to the real fin. The polarity angle distribution θ_i, which clustered around 90° at the initial time point, progressively spread between 0 and 90° (Fig. 6.5h-j). Although the decrease of $\overline{\theta}$ towards 60° was predictable from the definition of the polarity force, a striking result is that this force restricted the fin growth toward the distal pole, as observed in development. Furthermore, over the same period of time as in our dataset, the virtual fin grew to a size comparable to that of the real fin, from about 12.71 μm to about 52.94 μm (Fig. 6.5k), presenting over imaged fin an increase of just below 7%. Finally, our simulated fin acquired a global conic shape similar to that of the real fin (Fig. 6.5b-d,e-g). In order to get this quantitative agreement, a right balance between the forces in presence ($\overrightarrow{F}^{\mathrm{AR}}$, $\overrightarrow{F}^{\mathrm{Pol}}$) needed to be achieved. Proper scaling of these forces was done through model parameters ($J = 0.001, \nu = 1, \lambda = 0.2$). Taken together, these results suggest that directional cell behaviors, in particular alignment toward the PD axis of the zebrafish pectoral fin, could be an essential drive for its morphogenesis.

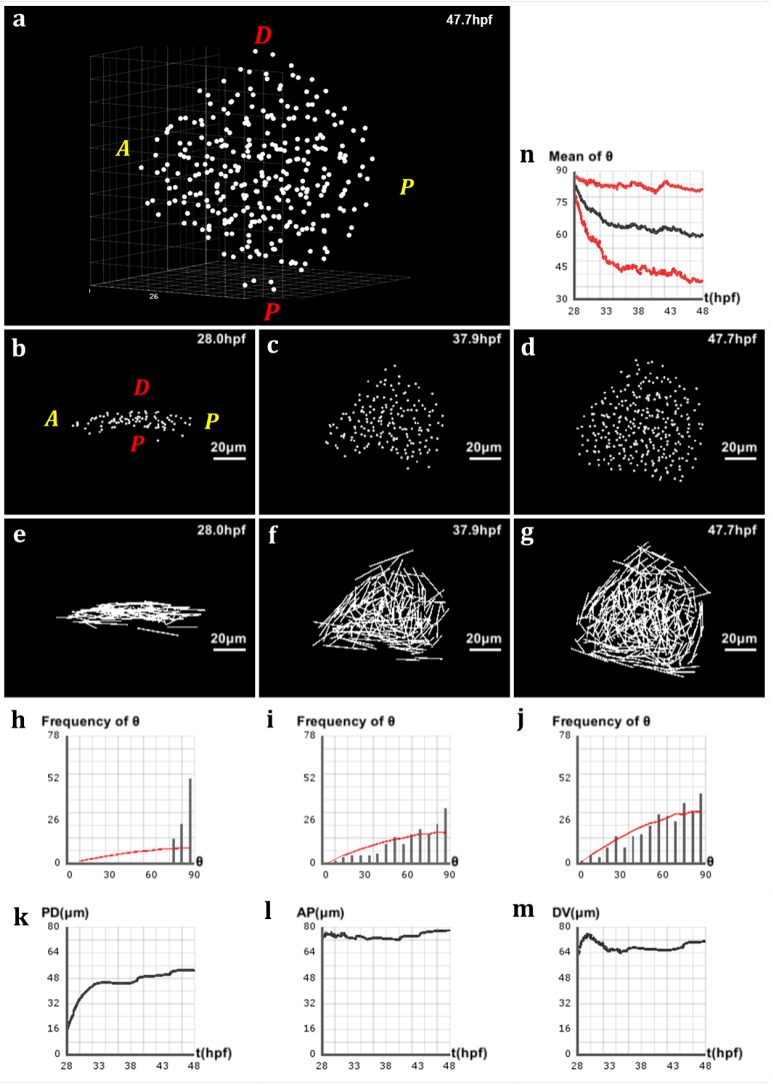

FIGURE 6.5: **Simulation of pectoral fin morphogenesis based on directional cell behaviors**. Values of the equation parameters: $J = 0.001, \lambda = 0.2, \nu = 1$. (a) 3D view of the simulated fin at the final stage $t = 47.8$ hpf. (b-d) Lateral view of the simulated fin at different stages of development, respectively $t = 28$ hpf, $t = 37.9$ hpf and $t = 47.7$ hpf. (e-g) Vector field of the cells' elongation axes $\overrightarrow{e}_i^{\text{Max}}$ in the simulated fin at the same stages. (h-j) Distribution of the polarity angles θ_i of the cells in the simulated fin at the same stages, compared with the standard distribution of random angles formed by two arbitrary vectors in 3D (red curve). (k-m) Evolution over time of the simulated fin size in μm along the PD, AP and DV axes respectively. We observe roughly the same behavior as the real fin in Fig. 6.1h-j. (n) Evolution over time of the average polarity angle $\overline{\theta}$ of the simulated fin cells $\pm$ its standard deviation $\Delta\theta$ shown in red. This curve is more scattered than Fig. 6.4k.

6.4 Discussion

The question of how vertebrates make their limbs is a fascinating problem in embryology that has been widely investigated across multiple species [144]. Although the study of molecular patterns underlying this morphogenesis has provided rich insights, the cellular basis of limb formation has not been completely elucidated. The availability of *in toto* imaging with resolution at the single cell level provides quantitative data for cells' behavior along their trajectory. New methods need to be developed to analyze such data, to use it to feed realistic models and evaluate hypotheses through a quantitative comparison between *in vivo* and *in silico* data. This work brings insights into the development of the zebrafish pectoral fin using quantitative analysis of imaging data and computational modelling.

Here, we investigated zebrafish pectoral fin development under the prism of the two dominant hypotheses of cellular behavior during limb growth. On the one hand, we analyzed proliferation behaviors in different regions of the fin, and found that proliferation gradients could not account for the observed growth. On the other hand, analysis of cellular elongation directions showed that cells tended on average to lower the angle they formed with the PD axis via their long axis, an indication of preferential polarity. To test this hypothesis, we formulated a simple mechanistic model of cells and simulated pectoral fin morphogenesis.

Our model of fin development based on quantitative biological data derived from live imaging and image processing accounts for the directional growth and the shape of the fin. However, due to some differences in comparison with imaging data, it also helps refine hypotheses concerning additional

constraints that were not integrated here. The simulated fin does not exhibit the same amplitude of slight compaction along the DV axis as the one measured in the biological data. In addition, the simulated fin shows a first phase of fast growth not quite observed in the zebrafish where the fin growth rate is closer to linear. We hypothesize that constraints imposed by the outside cell layers (i.e. ectodermal layer and enveloping layer) also contribute to the regulation of the fin growth and shaping, as observed in chick limb morphogenesis [121]. Chemical signalling from the outside cell layers, or other sources including for example electrical fields [72], could precisely play a role in the emergence of the cell polarization axes implemented in our model. Additionally, we considered the contribution of somitic cells that invade the fin bud during the time course of our observation as neutral regarding the overall growth and shaping. Both an *in vivo* and *in silico* experimentation are needed to support this view.

The biomechanical aspects privileged in our study are part of a complex interplay of genetic and mechanical cues characteristic of biological development. On the mechanical side, the requirement for cellular directional behaviours has been highlighted. However, local growth, evidenced by significant rise in cell population over the observed time span, is a key factor, serving to provide enough cells for the development of the organ, a conclusion also reached in mouse limb morphogenesis [13]. Moreover, other mechanisms such as cells coalignment or cell competition, which was shown to be preponderant in polarised tissues and organ size control, could equally be at play in pectoral fin morphogenesis [148]. To test the latter, a correlation analysis between cell polarisation and cell death would need to be performed. If the response of LPM cells during early fin development may mainly involve mechanical interactions, it is certainly required to integrate

genetic and molecular interactions as well in the transformation of the ectoderm that leads to shape the AER. Further studies may be integrate these mechanisms for more insights into zebrafish pectoral fin morphogenesis.

Supplementary figure 1

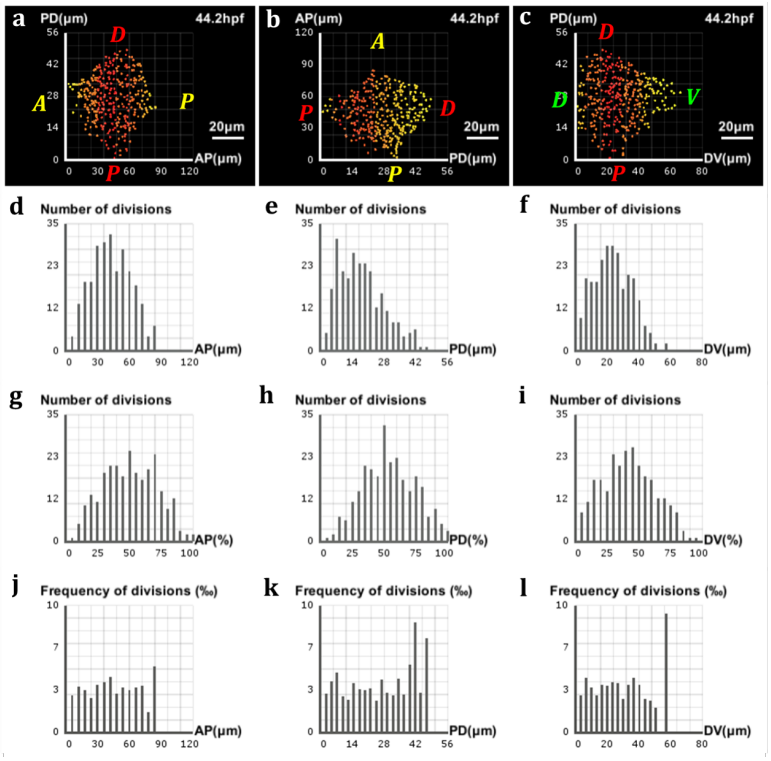

FIGURE S1: **Analysis of proliferation in the zebrafish pectoral fin (supplementary dataset)**. (a-c) Frequencies of divisions along the AP, PD and DV axes respectively, highlighted by a yellow-red color gradient coding for differences in proliferation rates across the fin. (a,c) The preponderance of red at the center of the fin shows where the bulk of cell divisions takes place, with only a few of them occurring near the lateral surfaces (yellow). (b) A decreasing gradient of proliferation rates from the proximal pole to the distal tip characterizes the PD axis. (d-f) Marginal distributions of proliferation along the AP, PD and DV axes respectively, expressed in numbers of cells with respect to the absolute distance in μm along the axis. (g-i) Same distributions with respect to the relative distance on the axis. (j-l) Same distributions expressed in proportions of cells with respect to the absolute distance.

Supplementary figure 2

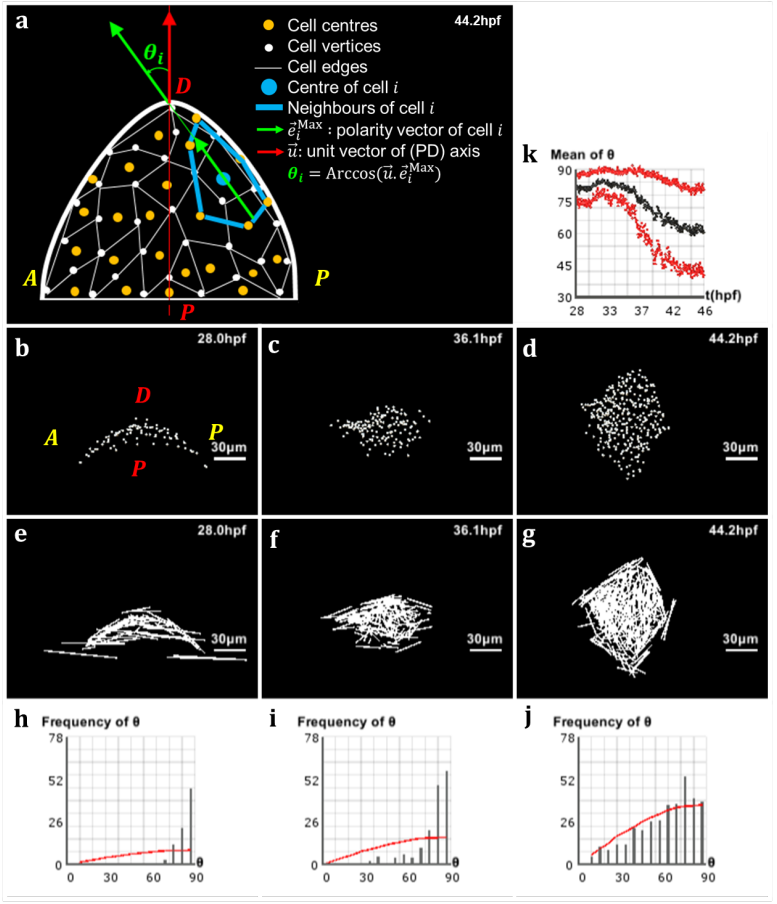

FIGURE S2: **Analysis of directional cell behaviors in the zebrafish pectoral fin (supplementary dataset)**. (a) Schematics in 2D of the method used to analyse directional cell behaviors: for each cell i, θ_i denotes the polarity angle that this cell forms between its elongation axis $\overrightarrow{e}_i^{\text{Max}}$ (extracted from the maximum eigenvalue of the covariance matrix of its neighborhood $\mathcal{N}_i$) and the PD axis $\overrightarrow{u}$. (b-d) Lateral view of the pectoral fin at different stages of development, respectively $t = 28.0$ hpf, $t = 36.1$ hpf and $t = 44.2$ hpf. (e-g) Vector field of the cells' elongation axes $\overrightarrow{e}_i^{\text{Max}}$ in the pectoral fin at the same stages. (h-j) Distribution of the polarity angles θ_i of the cells in the pectoral fin at the same stages, compared with the standard distribution of random angles formed by two arbitrary vectors in 3D (red curve). (k) Evolution over time of the average polarity angle $\overline{\theta}$ of the fin cells $\pm$ its standard deviation $\Delta\theta$ shown in red.

Chapter 7

Conclusion

Our goal in this research journey was to address the question of how computational models can contribute in unravelling the mysteries of biological development. Practically, the bulk of our work consists in formulating theoretical models that capture the dynamics of living tissues and simulating these models to investigate, in close collaboration with biologists, morphogenesis events in living systems. During our doctoral studies, this programme has been implemented through the development of agent-based models of cell and tissue mechanics, which were then used to gain valuable insights into the regulation of the epiblast shape and motion during mouse implantation, and the morphogenesis of the zebrafish pectoral fin.

In our initial project, we built upon the fundamental principles of Sub-cellular Element Models (SEM) to develop MG#, a multi-purpose novel model of cells and tissues biomechanics. In this model, a biological cell is abstracted by a cohort of particles whose triangulation form the cell membrane, and a single intracellular particle represent the biological cell. Non-linear elastic potentials between particles mimic the plasticity of

cell membranes and the activity of the cytoskeleton within the cell. These characteristics enable simulated cells to exhibit key behavioural properties of biological cells, such as division, apoptosis, bio-realistic shapes, and the feedback loop between biomechanical and biochemical effects, making MG# suitable for a broad range of morphological phenomena. In particular, we have shown that cell populations simulated with MG# can reproduce living tissue behaviours such as epithelial folding or the formation of multicellular rosettes.

In our next endeavour, we leveraged MG# to investigate the driving factor behind the symmetry-breaking in the mouse embryo epiblast during mouse implantation. At the onset of implantation, the mouse embryo consists of three cell lines: the embryonic tissue (epiblast), and two extra-embryonic tissues (trophectoderm and primitive endoderm). Building on previous studies, we hypothesised that epiblast remodelling into a cup results from mechanical constraints imposed by the polar trophectoderm, also undergoing significant morphogenesis in this time. We investigated this hypothesis by simulating both tissues with MG#.

In our latest project, we used computational modelling to study the morphogenesis of the zebrafish pectoral fin. More specifically, in collaboration with experimental biologists at the French CNRS *BioEmergences* lab, we sought to understand how this 3D organ develops from an initial layer of the cells. By analysing quantitative data resulting from the automatic tracking of single fin cells, we were able to rule out growth-based morphogenesis as the predominant factor for fin expansion along the PD axis. This result aligned with previous observations in mouse limbs, which also pointed us in the direction of examining cell elongation patterns in the fin. We found out that, during fin growth, cells aligned their long axis to the proximal-distal

axis (PD) of the zebrafish fin overtime. Building on this quantitative result, we enhanced the basic centre-based model by adding a polarity force term and specified proliferation rules based on cell cycle time. With this enhanced CBM model simulated fin growth.

In summary, the studies presented in this document highlight the effectiveness of mathematical and computational models in developmental biology and provide new insights in this field. Furthermore, the formulated models have been implemented as open source tools that were made available to the wider community by publishing their code on the open source sharing platform Github.

7.1 Future perspectives

The work carried out in this thesis can be further developed or adapted to accommodate more investigations of biological phenomena.

First, the models developed could be adapted for the purpose of studying other biological phenomena in development including differential-adhesion or differential-tension induced cell sorting, or pathological behaviours such as the growth of tumors. Although MG# simulations presented in this thesis were mostly limited to the scope of epithelial tissues, MG#, because of its deformable nature, can be enhanced to capture the dynamics of more complex cell arrangements and tissue topologies, making it suitable for both epithelia and mesenchyme. A step in this direction could be to graft onto MG# a theory of cell external contacts that accounts for cases where there may not exist an ideal mapping between external neighbouring particles. In order to achieve this, established contact mechanics methods such as Hertzian contact, Johnson-Kendall-Roberts or Maugis-Dugtale can be used

[27, 146]. To simulate differential-adhesion cell sorting for instance, single cells entourage would need to be updated periodically through their particles external neighbourhoods. In addition, contact surfaces, instead of punctual particle-particle contacts, would need to be defined around interacting particles of neighbouring cells. Moreover, different physical properties such as the modulus of elasticity of cells or the Poisson ratio would need to be defined in other to resolve adhesions on these contact surfaces.

In Chapter 6, we used a data-driven approach to examine the morphogenesis of the zebrafish pectoral fin. In this approach, we derived biological hypothesis directly from the analysis of the cell tracking data of fin cells and tested these hypothesis through simulations when necessary. However, more information, going from the subcellular activities of proteins, or genetic regulation, to cellular and tissue level like mechanical stresses, can be drawn from biological data. This data can then be integrated in the modelling workflow to infer model parameters or test model predictions [51].

Bibliography

[1] Ahrens, J., Geveci, B., and Law, C. Paraview: An end-user tool for large data visualization. *The visualization handbook 717* (2005).

[2] Alt, S., Ganguly, P., and Salbreux, G. Vertex models: From cell mechanics to tissue morphogenesis. *Philosophical transactions of the Royal Society of London. Series B, Biological sciences 372*, 1720 (5 2017), 20150520.

[3] Andrew, D. J., and Ewald, A. J. Morphogenesis of epithelial tubes: Insights into tube formation, elongation, and elaboration. *Developmental biology 341*, 1 (2010), 34–55.

[4] Arnold, S. J., and Robertson, E. J. Making a commitment: Cell lineage allocation and axis patterning in the early mouse embryo. *Nature reviews Molecular cell biology 10*, 2 (2009), 91–103.

[5] Atri, A., Amundson, J., Clapham, D., and Sneyd, J. A single-pool model for intracellular calcium oscillations and waves in the xenopus laevis oocyte. *Biophysical Journal 65*, 4 (1993), 1727–1739.

[6] Balbi, V., Destrade, M., and Goriely, A. The mechanics of human brain organoids. *Physical Review E 101* (2020).

[7] Basan, M., Prost, J., Joanny, J.-F., and Elgeti, J. Dissipative particle dynamics simulations for biological tissues: rheology and competition. *Physical biology 8*, 2 (2011), 026014.

[8] Bedzhov, I., Graham, S. J., Leung, C. Y., and Zernicka-Goetz, M. Developmental plasticity, cell fate specification and morphogenesis in the early mouse embryo. *Philosophical Transactions of the Royal Society B: Biological Sciences 369*, 1657 (2014), 20130538.

[9] Bedzhov, I., and Zernicka-Goetz, M. Self-organizing properties of mouse pluripotent cells initiate morphogenesis upon implantation. *Cell 156*, 5 (2014), 1032–1044.

[10] Belmonte, J. M., Swat, M. H., and Glazier, J. A. Filopodial-tension model of convergent-extension of tissues. *PLoS computational biology 12*, 6 (2016), e1004952.

[11] Binder, K., Ceperley, D. M., Hansen, J.-P., Kalos, M., Landau, D., Levesque, D., Mueller-Krumbhaar, H., Stauffer, D., and Weis, J.-J. *Monte Carlo methods in statistical physics*, vol. 7. Springer Science & Business Media, 2012.

[12] Blankenship, J. T., Backovic, S. T., Sanny, J. S., Weitz, O., and Zallen, J. A. Multicellular rosette formation links planar cell polarity to tissue morphogenesis. *Developmental cell 11*, 4 (2006), 459–470.

[13] Boehm, B., Westerberg, H., Lesnicar-Pucko, G., Raja, S., Rautschka, M., Cotterell, J., Swoger, J., and Sharpe, J. The role of spatially controlled cell proliferation in limb bud morphogenesis. *PLoS biology 8*, 7 (2010).

[14] Bongiorno, T., Kazlow, J., Mezencev, R., Griffiths, S., Olivares-Navarrete, R., McDonald, J. F., Schwartz, Z., Boyan, B. D., McDevitt, T. C., and Sulchek, T. Mechanical stiffness as an improved single-cell indicator of osteoblastic human mesenchymal stem cell differentiation. *Journal of biomechanics 47*, 9 (2014), 2197–2204.

[15] Boocock, D., Hino, N., Ruzickova, N., Hirashima, T., and Hannezo, E. Theory of mechanochemical patterning and optimal migration in cell monolayers. *Nature Physics 17*, 2 (2021), 267–274.

[16] Brand-Saberi, B., Seifert, R., Grim, M., Wilting, J., Köhlewein, M., and Christ, B. Blood vessel formation in the avian limb bud involves angioblastic and angiotrophic growth. *Developmental Dynamics 202*, 2 (1995), 181–194.

[17] Brodland, G. W. How computational models can help unlock biological systems, 2015.

[18] Brodland, G. W., and Chen, H. H. The mechanics of heterotypic cell aggregates: insights from computer simulations. *Journal of Biomechanical Engineering 122*, 4 (2000), 402.

[19] Brodland, G. W., Conte, V., Cranston, P. G., Veldhuis, J., Narasimhan, S., Hutson, M. S., Jacinto, A., Ulrich, F., Baum, B., and Miodownik, M. Video force microscopy reveals the mechanics of ventral furrow invagination in drosophila. *Proceedings of the National Academy of Sciences 107*, 51 (2010), 22111–22116.

[20] Brown, J. M., and García-García, M. J. Secretory pathway calcium atpase 1 (spca1) controls mouse neural tube closure by regulating cytoskeletal dynamics. *Development 145*, 19 (2018).

[21] Cameron, J., and McCredie, J. Innervation of the undifferentiated limb bud in rabbit embryo. *Journal of anatomy 134*, Pt 4 (1982), 795.

[22] Chan, C. J., Costanzo, M., Ruiz-Herrero, T., Mönke, G., Petrie, R. J., Bergert, M., Diz-Munoz, A., Mahadevan, L., and Hiiragi, T. Hydraulic control of mammalian embryo size and cell fate. *Nature 571*, 7763 (2019), 112–116.

[23] Christ, B., and Brand-Saberi, B. Limb muscle development. *International Journal of Developmental Biology 46*, 7 (2002), 905–914.

[24] Christodoulou, N., Kyprianou, C., Weberling, A., Wang, R., Cui, G., Peng, G., Jing, N., and Zernicka-Goetz, M. Sequential formation and resolution of multiple rosettes drive embryo remodelling after implantation. *Nature Cell Biology 20*, 11 (2018), 1278–1289.

[25] Christodoulou, N., and Skourides, P. A. Cell-autonomous Ca2+ flashes elicit pulsed contractions of an apical actin network to drive apical constriction during neural tube closure. *Cell reports 13*, 10 (2015), 2189–2202.

[26] Christodoulou, N., Weberling, A., Strathdee, D., Anderson, K. I., Timpson, P., and Zernicka-Goetz, M. Morphogenesis of extra-embryonic tissues directs the remodelling of the mouse embryo at implantation. *Nature Communications 10*, 1 (2019), 1–12.

[27] Chu, Y.-S., Dufour, S., Thiery, J. P., Perez, E., and Pincet, F. Johnson-kendall-roberts theory applied to living cells. *Physical review letters 94*, 2 (2005), 028102.

[28] Chung, S., and Andrew, D. J. The formation of epithelial tubes. *Journal of cell science 121*, 21 (2008), 3501–3504.

[29] Chung, S., and Andrew, D. J. Cadherin 99C regulates apical expansion and cell rearrangement during epithelial tube elongation. *Development 141*, 9 (2014), 1950–1960.

[30] Coen, E. *The art of genes: how organisms make themselves*. Oxford University Press, 2000.

[31] Coucouvanis, E., and Martin, G. R. Signals for death and survival: A two-step mechanism for cavitation in the vertebrate embryo. *Cell 83*, 2 (1995), 279–287.

[32] Davidson, L. A. Epithelial machines that shape the embryo. *Trends in cell biology 22*, 2 (2012), 82–87.

[33] Debnath, J., Mills, K. R., Collins, N. L., Reginato, M. J., Muthuswamy, S. K., and Brugge, J. S. The role of apoptosis in creating and maintaining luminal space within normal and oncogene-expressing mammary acini. *Cell 111*, 1 (2002), 29–40.

[34] Delile, J., Doursat, R., and Peyriéras, N. Computational modeling and simulation of animal early embryogenesis with the MecaGen platform. In *Computational Systems Biology*. Elsevier, 2014, pp. 359–405.

[35] Delile, J., Herrmann, M., Peyriéras, N., and Doursat, R. A cell-based computational model of early embryogenesis coupling mechanical behaviour and gene regulation. *Nature Communications 8*, 1 (2017), 1–10.

[36] Dequidt, A., Devemy, J., and Padua, A. A. Thermalized drude oscillators with the lammps molecular dynamics simulator. *Journal of chemical information and modeling 56*, 1 (2016), 260–268.

[37] Dijkstra, E. W. On the role of scientific thought. In *Selected writings on computing: a personal perspective*. Springer, 1982, pp. 60–66.

[38] Dillon, R., and Othmer, H. G. A mathematical model for outgrowth and spatial patterning of the vertebrate limb bud. *Journal of theoretical biology 197*, 3 (1999), 295–330.

[39] Disset, J. *Simulation de Cellules et Réseaux de Regulation Génétique Artificiels pour le Développement et l'Auto-organisation de Créatures Multicellulaires*. PhD dissertation, Université de Toulouse, 2017.

[40] Disset, J., Cussat-Blanc, S., and Duthen, Y. MecaCell: an Open-source Efficient Cellular Physics Engine. In *ECAL* (2015).

[41] Drasdo, D., and Höhme, S. A single-cell-based model of tumor growth in vitro: monolayers and spheroids. *Physical biology 2*, 3 (2005), 133.

[42] Drasdo, D., and Loeffler, M. Individual-based models to growth and folding in one-layered tissues: intestinal crypts and early development. *Nonlinear Analysis: Theory, Methods & Applications 47*, 1 (2001), 245–256.

[43] Duclut, C., Sarkar, N., Prost, J., and Jülicher, F. Fluid pumping and active flexoelectricity can promote lumen nucleation in cell assemblies. *Proceedings of the National Academy of Sciences 116*, 39 (2019), 19264–19273.

[44] Dupont, G., Falcke, M., Kirk, V., and Sneyd, J. *Models of calcium signalling*, vol. 43. Springer, 2016.

[45] Estrada, J., Andrew, N., Gibson, D., Chang, F., Gnad, F., and Gunawardena, J. Cellular interrogation: exploiting cell-to-cell variability to discriminate regulatory mechanisms in oscillatory signalling. *PLoS computational biology 12*, 7 (2016), e1004995.

[46] Evans, E., and Fung, Y.-C. Improved measurements of the erythrocyte geometry. *Microvascular research 4*, 4 (1972), 335–347.

[47] Farhadifar, R., Röper, J.-C., Aigouy, B., Eaton, S., and Jülicher, F. The influence of cell mechanics, cell-cell interactions, and proliferation on epithelial packing. *Current Biology 17*, 24 (12 2007), 2095–2104.

[48] Faure, E., Savy, T., Rizzi, B., Melani, C., Stašová, O., Fabrèges, D., Špir, R., Hammons, M., Čúnderlík, R., Recher, G., et al. A workflow to process 3d+ time microscopy images of developing organisms and reconstruct their cell lineage. *Nature Communications 7*, 1 (2016), 1–10.

[49] Fedosov, D. A., Caswell, B., and Karniadakis, G. E. Systematic coarse-graining of spectrin-level red blood cell models. *Computer Methods in Applied Mechanics and Engineering 199*, 29-32 (2010), 1937–1948.

[50] Fedosov, D. A., Lei, H., Caswell, B., Suresh, S., and Karniadakis, G. E. Multiscale modeling of red blood cell mechanics and blood flow in malaria. *PLoS Computational Biology 7*, 12 (12 2011), e1002270.

[51] Fletcher, A., and Osborne, J. Seven challenges in the multiscale modelling of multicellular tissues. *Preprints* (2020).

[52] Fletcher, A., Osterfield, M., Baker, R., and Shvartsman, S. Vertex Models of Epithelial Morphogenesis. *Biophysical Journal 106*, 11 (6 2014), 2291–2304.

[53] Fletcher, A. G., Cooper, F., and Baker, R. E. Mechanocellular models of epithelial morphogenesis. *Philosophical Transactions of the Royal Society B: Biological Sciences 372*, 1720 (2017), 20150519.

[54] Fletcher, A. G., Osterfield, M., Baker, R. E., and Shvartsman, S. Y. Vertex models of epithelial morphogenesis. *Biophysical Journal 106*, 11 (6 2014), 2291–2304.

[55] Fristrom, D. The cellular basis of epithelial morphogenesis. a review. *Tissue and Cell 20*, 5 (1988), 645–690.

[56] Fukui, Y., Hirota, Y., Matsuo, M., Gebril, M., Akaeda, S., Hiraoka, T., and Osuga, Y. Uterine receptivity, embryo attachment, and embryo invasion: Multistep processes in embryo implantation. *Reproductive medicine and biology 18*, 3 (2019), 234–240.

[57] Germann, P., Marin-Riera, M., and Sharpe, J. ya|| a: Gpu-powered spheroid models for mesenchyme and epithelium. *Cell systems 8*, 3 (2019), 261–266.

[58] Glazier, J. A., and Graner, F. Simulation of the differential adhesion driven rearrangement of biological cells. *Physical Review E 47*, 3 (3 1993), 2128–2154.

[59] Goriely, A., Erlich, A., Jones, G., Tisseur, F., and Moulton, D. The role of topology and mechanics in uniaxially growing cell networks. *Proceedings of the Royal Society A: Mathematical, Physical and Engineering Sciences 476*, 2233 (2020).

[60] Graner, F., and Glazier, J. A. Simulation of biological cell sorting using a two-dimensional extended Potts model. *Physical Review Letters 69*, 13 (9 1992), 2013–2016.

[61] Green, J. B. A., and Sharpe, J. Positional information and reaction-diffusion: two big ideas in developmental biology combine. *Development (Cambridge, England) 142*, 7 (4 2015), 1203–11.

[62] Grim, M., and Christ, B. Neural crest cell migration into the limb bud of avian embryos. *Progress in clinical and biological research 383* (1993), 391–402.

[63] Gros, J., Hu, J. K.-H., Vinegoni, C., Feruglio, P. F., Weissleder, R., and Tabin, C. J. WNT5A/JNK and FGF/MAPK pathways regulate the cellular events shaping the vertebrate limb bud. *Current Biology 20*, 22 (2010), 1993–2002.

[64] Hannezo, E., and Heisenberg, C.-P. Mechanochemical feedback loops in development and disease. *Cell 178*, 1 (2019), 12–25.

[65] Harding, M. J., McGraw, H. F., and Nechiporuk, A. The roles and regulation of multicellular rosette structures during morphogenesis. *Development 141*, 13 (2014), 2549–2558.

[66] Hardy, A., and Steeb, W.-H. *Mathematical Tools in Computer Graphics with C# Implementations*. WORLD SCIENTIFIC, 1 2008.

[67] Harrison, S. E., Sozen, B., Christodoulou, N., Kyprianou, C., and Zernicka-Goetz, M. Assembly of embryonic and extraembryonic stem cells to mimic embryogenesis in vitro. *Science 356*, 6334 (2017), eaal1810.

[68] Heisenberg, C.-P. D'arcy thompson's 'on growth and form': From soap bubbles to tissue self-organization. *Mechanisms of Development 145* (6 2017), 32–37.

[69] Honda, H. The world of epithelial sheets. *Development, Growth & Differentiation 59*, 5 (2017), 306–316.

[70] Honda, H., and Nagai, T. Cell models lead to understanding of multi-cellular morphogenesis consisting of successive self-construction of cells. *Journal of Biochemistry 157*, 3 (3 2015), 129–136.

[71] Honda, H., Tanemura, M., and Nagai, T. A three-dimensional vertex dynamics cell model of space-filling polyhedra simulating cell behavior in a cell aggregate. *Journal of theoretical biology 226*, 4 (2004), 439–453.

[72] Hopyan, S. Biophysical regulation of early limb bud morphogenesis. *Developmental biology 429*, 2 (2017), 429–433.

[73] Huang, R., Zhi, Q., and Christ, B. The relationship between limb muscle and endothelial cells migrating from single somite. *Anatomy and embryology 206*, 4 (2003), 283–289.

[74] Huttenlocher, D. P., Klanderman, G. A., and Rucklidge, W. J. Comparing images using the Hausdorff distance. *IEEE Transactions on pattern analysis and machine intelligence 15*, 9 (1993), 850–863.

[75] Inoue, Y., Suzuki, M., Watanabe, T., Yasue, N., Tateo, I., Adachi, T., and Ueno, N. Mechanical roles of apical constriction, cell elongation, and cell migration during neural tube formation in xenopus. *Biomechanics and modeling in mechanobiology 15*, 6 (2016), 1733–1746.

[76] Ising, E. Beitrag zur theorie des ferromagnetismus. *Zeitschrift für Physik 31*, 1 (1925), 253–258.

[77] Jacobson, A. G., and Gordon, R. Changes in the shape of the developing vertebrate nervous system analyzed experimentally, mathematically and by computer simulation. *Journal of Experimental Zoology 197*, 2 (1976), 191–246.

[78] Kaouri, K., Maini, P. K., Skourides, P., Christodoulou, N., and Chapman, S. J. A simple mechanochemical model for calcium signalling in embryonic epithelial cells. *Journal of mathematical biology 78*, 7 (2019), 2059–2092.

[79] Keller, R. Physical biology returns to morphogenesis. *Science 338*, 6104 (10 2012), 201–203.

[80] Kimmel, C. B., Ballard, W. W., Kimmel, S. R., Ullmann, B., and Schilling, T. F. Stages of embryonic development of the zebrafish. *Developmental dynamics 203*, 3 (1995), 253–310.

[81] Kojima, Y., Tam, O. H., and Tam, P. P. Timing of developmental events in the early mouse embryo. In *Seminars in cell & developmental biology* (2014), vol. 34, Elsevier, pp. 65–75.

[82] Kolega, J. The cellular basis of epithelial morphogenesis. In *The Cellular Basis of Morphogenesis*. Springer, 1986, pp. 103–143.

[83] Kursawe, J., Baker, R. E., and Fletcher, A. G. Approximate Bayesian computation reveals the importance of repeated measurements for parameterising cell-based models of growing tissues. *Journal of Theoretical Biology 443* (4 2018), 66–81.

[84] Lecuit, T., and Lenne, P.-F. Cell surface mechanics and the control of cell shape, tissue patterns and morphogenesis. *Nature Reviews Molecular Cell Biology 8*, 8 (8 2007), 633–644.

[85] Lenne, P. F., Munro, E., Heemskerk, I., Warmflash, A., Bocanegra-Moreno, L., Kishi, K., Kicheva, A., Long, Y., Fruleux, A., Boudaoud, A., et al. Roadmap on multiscale coupling of biochemical and mechanical signals during development. *Physical Biology* (2020).

[86] Li, S., and Muneoka, K. Cell migration and chick limb development: chemotactic action of FGF-4 and the AER. *Developmental biology 211*, 2 (1999), 335–347.

[87] Lienkamp, S. S., Liu, K., Karner, C. M., Carroll, T. J., Ronneberger, O., Wallingford, J. B., and Walz, G. Vertebrate kidney tubules elongate using a planar cell polarity–dependent, rosette-based mechanism of convergent extension. *Nature genetics 44*, 12 (2012), 1382–1387.

[88] Malmi Kakkada, A., Li, X., Samanta, H. S., Sinha, S., and Thirumalai, D. Cell growth rate dictates the onset of glass to fluidlike transition and long time super-diffusion in an evolving cell colony. *Biophysical Journal 114*, 3 (2 2018), 323a.

[89] Malmi-Kakkada, A. N., Li, X., Samanta, H. S., Sinha, S., and Thirumalai, D. Cell growth rate dictates the onset of glass to fluidlike transition and long time superdiffusion in an evolving cell colony. *Physical Review X 8*, 2 (2018), 021025.

[90] Marin-Riera, M., Brun-Usan, M., Zimm, R., Välikangas, T., and Salazar-Ciudad, I. Computational modeling of development

by epithelia, mesenchyme and their interactions: a unified model. *Bioinformatics 32*, 2 (9 2015), btv527.

[91] Martin, A. C., Gelbart, M., Fernandez-Gonzalez, R., Kaschube, M., and Wieschaus, E. F. Integration of contractile forces during tissue invagination. *Journal of Cell Biology 188*, 5 (2010), 735–749.

[92] Martin, A. C., and Goldstein, B. Apical constriction: themes and variations on a cellular mechanism driving morphogenesis. *Development 141*, 10 (2014), 1987–1998.

[93] Martin, A. C., Kaschube, M., and Wieschaus, E. F. Pulsed contractions of an actin–myosin network drive apical constriction. *Nature 457*, 7228 (2009), 495–499.

[94] Martín-Belmonte, F., Yu, W., Rodríguez-Fraticelli, A. E., Ewald, A., Werb, Z., Alonso, M. A., and Mostov, K. Cell-polarity dynamics controls the mechanism of lumen formation in epithelial morphogenesis. *Current Biology 18*, 7 (2008), 507–513.

[95] McShane, S. G., Molè, M. A., Savery, D., Greene, N. D., Tam, P. P., and Copp, A. J. Cellular basis of neuroepithelial bending during mouse spinal neural tube closure. *Developmental biology 404*, 2 (2015), 113–124.

[96] Merks, R. M., Guravage, M., Inzé, D., and Beemster, G. T. Virtualleaf: an open-source framework for cell-based modeling of plant tissue growth and development. *Plant physiology 155*, 2 (2011), 656–666.

[97] Micoulet, A., Spatz, J. P., and Ott, A. Mechanical response analysis and power generation by single-cell stretching. *ChemPhysChem 6*, 4 (2005), 663–670.

[98] Milde, F., Tauriello, G., Haberkern, H., and Koumoutsakos, P. SEM++: A particle model of cellular growth, signaling and migration. *Computational Particle Mechanics 1*, 2 (6 2014), 211–227.

[99] Mirams, G. R., Arthurs, C. J., Bernabeu, M. O., Bordas, R., Cooper, J., Corrias, A., Davit, Y., Dunn, S.-J., Fletcher, A. G., Harvey, D. G., et al. Chaste: an open source c++ library for computational physiology and biology. *PLoS Comput Biol 9*, 3 (2013), e1002970.

[100] Morishita, Y., and Iwasa, Y. Growth based morphogenesis of vertebrate limb bud. *Bulletin of mathematical biology 70*, 7 (2008), 1957–1978.

[101] Nagai, T., and Honda, H. A dynamic cell model for the formation of epithelial tissues. *Philosophical Magazine B 81*, 7 (2001), 699–719.

[102] Newman, T. J. Modeling multi-cellular systems using sub-cellular elements. *arXiv preprint q-bio/0504028* (2005).

[103] Nguyen, H., Boix-Fabrés, J., Peyriéras, N., and Kardash, E. 3d+ time imaging and image reconstruction of pectoral fin during zebrafish embryogenesis. In *Computer Optimized Microscopy*. Springer, 2019, pp. 135–153.

[104] Niculescu, I., Textor, J., and de Boer, R. J. Crawling and gliding: a computational model for shape-driven cell migration. *PLOS Computational Biology 11*, 10 (10 2015), e1004280.

[105] Niswander, L., Tickle, C., Vogel, A., Booth, I., and Martin, G. R. FGF-4 replaces the apical ectodermal ridge and directs outgrowth and patterning of the limb. *Cell 75*, 3 (1993), 579–587.

[106] Odell, G. M., Oster, G., Alberch, P., and Burnside, B. The mechanical basis of morphogenesis: I. epithelial folding and invagination. *Developmental biology 85*, 2 (1981), 446–462.

[107] Odenthal, T., Smeets, B., Van Liedekerke, P., Tijskens, E., Van Oosterwyck, H., and Ramon, H. Analysis of initial cell spreading using mechanistic contact formulations for a deformable cell model. *PLoS Computational Biology 9*, 10 (10 2013), e1003267.

[108] Odenthal, T., Smeets, B., Van Liedekerke, P., Tijskens, E., Van Oosterwyck, H., and Ramon, H. Analysis of initial cell spreading using mechanistic contact formulations for a deformable cell model. *PLoS computational biology 9*, 10 (2013).

[109] Ogura, Y., Wen, F.-L., Sami, M. M., Shibata, T., and Hayashi, S. A switch-like activation relay of EGFR-ERK signaling regulates a wave of cellular contractility for epithelial invagination. *Developmental cell 46*, 2 (2018), 162–172.

[110] Okuda, S., Inoue, Y., Eiraku, M., Adachi, T., and Sasai, Y. Vertex dynamics simulations of viscosity-dependent deformation during tissue morphogenesis. *Biomechanics and Modeling in Mechanobiology 14*, 2 (4 2015), 413–425.

[111] Okuda, S., Inoue, Y., Eiraku, M., Sasai, Y., and Adachi, T. Apical contractility in growing epithelium supports robust maintenance of smooth curvatures against cell-division-induced mechanical disturbance. *Journal of Biomechanics 46*, 10 (6 2013), 1705–1713.

[112] Okuda, S., Inoue, Y., Eiraku, M., Sasai, Y., and Adachi, T. Modeling cell proliferation for simulating three-dimensional tissue morphogenesis based on a reversible network reconnection framework. *Biomechanics and Modeling in Mechanobiology 12*, 5 (10 2013), 987–996.

[113] Okuda, S., Inoue, Y., Eiraku, M., Sasai, Y., and Adachi, T. Reversible network reconnection model for simulating large deformation in dynamic tissue morphogenesis. *Biomechanics and Modeling in Mechanobiology 12*, 4 (8 2013), 627–644.

[114] Okuda, S., Inoue, Y., Watanabe, T., and Adachi, T. Coupling intercellular molecular signalling with multicellular deformation for simulating three-dimensional tissue morphogenesis. *Interface Focus* (2015).

[115] Okuda, S., Miura, T., Inoue, Y., Adachi, T., and Eiraku, M. Combining Turing and 3D vertex models reproduces autonomous multicellular morphogenesis with undulation, tubulation, and branching. *Scientific Reports 8*, 1 (12 2018), 2386.

[116] Osborne, J. M., Fletcher, A. G., Pitt-Francis, J. M., Maini, P. K., and Gavaghan, D. J. Comparing individual-based approaches to modelling the self-organization of multicellular tissues. *PLoS computational biology 13*, 2 (2017), e1005387.

[117] Parfitt, D.-E., and Shen, M. M. From blastocyst to gastrula: Gene regulatory networks of embryonic stem cells and early mouse embryogenesis. *Philosophical Transactions of the Royal Society B: Biological Sciences 369*, 1657 (2014), 20130542.

[118] Pathmanathan, P., Cooper, J., Fletcher, A., Mirams, G., Murray, P., Osborne, J., Pitt-Francis, J., Walter, A., and Chapman, S. A computational study of discrete mechanical tissue models. *Physical biology 6*, 3 (2009), 036001.

[119] Pearl, E. J., Li, J., and Green, J. B. Cellular systems for epithelial invagination. *Philosophical Transactions of the Royal Society B: Biological Sciences 372*, 1720 (2017), 20150526.

[120] Pillarisetti, A., Desai, J. P., Ladjal, H., Schiffmacher, A., Ferreira, A., and Keefer, C. L. Mechanical phenotyping of mouse embryonic stem cells: increase in stiffness with differentiation. *Cellular Reprogramming (Formerly" Cloning and Stem Cells") 13*, 4 (2011), 371–380.

[121] Popławski, N. J., Swat, M., Gens, J. S., and Glazier, J. A. Adhesion between cells, diffusion of growth factors, and elasticity of the aer produce the paddle shape of the chick limb. *Physica A: Statistical Mechanics and its Applications 373* (2007), 521–532.

[122] Rashevsky, N. An approach to the mathematical biophysics of biological self-regulation and of cell polarity. *The bulletin of mathematical biophysics 2*, 1 (1940), 15–25.

[123] Rashevsky, N. Topology and life: in search of general mathematical principles in biology and sociology. *The bulletin of mathematical biophysics 16*, 4 (1954), 317–348.

[124] Recher, G., Jouralet, J., Brombin, A., Heuzé, A., Mugniery, E., Hermel, J.-M., Desnoulez, S., Savy, T., Herbomel, P., Bourrat, F., et al. Zebrafish midbrain slow-amplifying progenitors

exhibit high levels of transcripts for nucleotide and ribosome biogenesis. *Development 140*, 24 (2013), 4860–4869.

[125] Recho, P., Hallou, A., and Hannezo, E. Theory of mechanochemical patterning in biphasic biological tissues. *Proceedings of the National Academy of Sciences 116*, 12 (2019), 5344–5349.

[126] Reiter, R. S., and Solursh, M. Mitogenic property of the apical ectodermal ridge. *Developmental biology 93*, 1 (1982), 28–35.

[127] Revell, C., Blumenfeld, R., and Chalut, K. J. Force-based three-dimensional model predicts mechanical drivers of cell sorting. *Proceedings of the Royal Society B 286*, 1895 (2019), 20182495.

[128] Rivera-Pérez, J. A., and Hadjantonakis, A.-K. The dynamics of morphogenesis in the early mouse embryo. *Cold Spring Harbor perspectives in biology 7*, 11 (6 2014), a015867.

[129] Rohrschneider, M. R., and Nance, J. Polarity and cell fate specification in the control of caenorhabditis elegans gastrulation. *Developmental Dynamics 238*, 4 (2009), 789–796.

[130] Sandersius, S. A., and Newman, T. J. Modeling cell rheology with the subcellular element model. *Physical biology 5*, 1 (2008), 015002.

[131] Sawyer, J. M., Harrell, J. R., Shemer, G., Sullivan-Brown, J., Roh-Johnson, M., and Goldstein, B. Apical constriction: a cell shape change that can drive morphogenesis. *Developmental biology 341*, 1 (2010), 5–19.

[132] Shahbazi, M. N., Jedrusik, A., Vuoristo, S., Recher, G., Hupalowska, A., Bolton, V., Fogarty, N. M., Campbell, A., Devito, L. G., Ilic, D., et al. Self-organization of the human

embryo in the absence of maternal tissues. *Nature Cell Biology 18*, 6 (2016), 700–708.

[133] Shahbazi, M. N., Scialdone, A., Skorupska, N., Weberling, A., Recher, G., Zhu, M., Jedrusik, A., Devito, L. G., Noli, L., Macaulay, I. C., et al. Pluripotent state transitions coordinate morphogenesis in mouse and human embryos. *Nature 552*, 7684 (2017), 239–243.

[134] Shahbazi, M. N., and Zernicka-Goetz, M. Deconstructing and reconstructing the mouse and human early embryo. *Nature Cell Biology 20*, 8 (2018), 878–887.

[135] Sharpe, J. Computer modeling in developmental biology: Growing today, essential tomorrow. *Development 144*, 23 (2017), 4214–4225.

[136] Sherrard, K., Robin, F., Lemaire, P., and Munro, E. Sequential activation of apical and basolateral contractility drives ascidian endoderm invagination. *Current Biology 20*, 17 (2010), 1499–1510.

[137] Shyer, A. E., Tallinen, T., Nerurkar, N. L., Wei, Z., Gil, E. S., Kaplan, D. L., Tabin, C. J., and Mahadevan, L. Villification: how the gut gets its villi. *Science 342*, 6155 (2013), 212–218.

[138] Steinberg, M. S. Adhesion-guided multicellular assembly: a commentary upon the postulates, real and imagined, of the differential adhesion hypothesis, with special attention to computer simulations of cell sorting. *Journal of theoretical biology 55*, 2 (1975), 431–443.

[139] Sui, L., Alt, S., Weigert, M., Dye, N., Eaton, S., Jug, F., Myers, E. W., Jülicher, F., Salbreux, G., and Dahmann, C. Differential lateral and basal tension drive folding of drosophila wing

discs through two distinct mechanisms. *Nature Communications 9*, 1 (2018), 1–13.

[140] Suzanne, M., and Steller, H. Shaping organisms with apoptosis. *Cell Death & Differentiation 20*, 5 (2013), 669–675.

[141] Suzuki, M., Sato, M., Koyama, H., Hara, Y., Hayashi, K., Yasue, N., Imamura, H., Fujimori, T., Nagai, T., Campbell, R. E., et al. Distinct intracellular Ca2+ dynamics regulate apical constriction and differentially contribute to neural tube closure. *Development 144*, 7 (2017), 1307–1316.

[142] Swat, M. H., Thomas, G. L., Belmonte, J. M., Shirinifard, A., Hmeljak, D., and Glazier, J. A. Multi-scale modeling of tissues using compucell3D. *Methods in cell biology 110* (2012), 325–366.

[143] Thompson, D. W., et al. On growth and form. *On growth and form.* (1942).

[144] Tickle, C. How the embryo makes a limb: determination, polarity and identity. *Journal of anatomy 227*, 4 (2015), 418–430.

[145] Turing, A. M. *The Chemical Basis of Morphogenesis*, vol. 237. Royal Society.

[146] Van Liedekerke, P., Palm, M., Jagiella, N., and Drasdo, D. Simulating tissue mechanics with agent-based models: concepts, perspectives and some novel results. *Computational particle mechanics 2*, 4 (2015), 401–444.

[147] Villoutreix, P., Delile, J., Rizzi, B., Duloquin, L., Savy, T., Bourgine, P., Doursat, R., and Peyriéras, N. An integrated

modelling framework from cells to organism based on a cohort of digital embryos. *Scientific reports 6* (2016), 37438.

[148] Vincent, J.-P., Fletcher, A. G., and Baena-Lopez, L. A. Mechanisms and mechanics of cell competition in epithelia. *Nature reviews Molecular cell biology 14*, 9 (2013), 581–591.

[149] Wang, H., and Dey, S. K. Roadmap to embryo implantation: Clues from mouse models. *Nature Reviews Genetics 7*, 3 (2006), 185–199.

[150] Wang, Q., Holmes, W. R., Sosnik, J., Schilling, T., and Nie, Q. Cell Sorting and Noise-Induced Cell Plasticity Coordinate to Sharpen Boundaries between Gene Expression Domains. *PLOS Computational Biology 13*, 1 (1 2017), e1005307.

[151] Wen, F.-L., Wang, Y.-C., and Shibata, T. Epithelial folding driven by apical or basal-lateral modulation: geometric features, mechanical inference, and boundary effects. *Biophysical Journal 112*, 12 (2017), 2683–2695.

[152] Wolpert, L., Tickle, C., and Arias, A. M. *Principles of development*. Oxford university press, 2015.

[153] Yanagida, A., Revell, C., Stirparo, G. G., Corujo-Simon, E., Aspalter, I. M., Peters, R., De Belly, H., Cassani, D. A., Achouri, S., Blumenfeld, R., et al. Cell surface fluctuations regulate early embryonic lineage sorting. *BioRxiv* (2020).

[154] Yu, J. C., and Fernandez-Gonzalez, R. Quantitative modelling of epithelial morphogenesis: integrating cell mechanics and molecular dynamics. *Seminars in Cell & Developmental Biology 67* (7 2017), 153–160.

[155] Zhang, S., Chen, T., Chen, N., Gao, D., Shi, B., Kong, S., West, R. C., Yuan, Y., Zhi, M., Wei, Q., et al. Implantation initiation of self-assembled embryo-like structures generated using three types of mouse blastocyst-derived stem cells. *Nature Communications 10*, 1 (2019), 1–17.

[156] Zhou, J., Kim, H. Y., and Davidson, L. A. Actomyosin stiffens the vertebrate embryo during crucial stages of elongation and neural tube closure. *Development 136*, 4 (2009), 677–688.

List of Figures